



## Light-matter interaction in low-dimensional materials. A theoretical study

Gjerding, Morten Niklas

*Publication date:*  
2016

*Document Version*  
Publisher's PDF, also known as Version of record

[Link back to DTU Orbit](#)

*Citation (APA):*  
Gjerding, M. N. (2016). *Light-matter interaction in low-dimensional materials. A theoretical study*. Department of Physics, Technical University of Denmark.

---

### General rights

Copyright and moral rights for the publications made accessible in the public portal are retained by the authors and/or other copyright owners and it is a condition of accessing publications that users recognise and abide by the legal requirements associated with these rights.

- Users may download and print one copy of any publication from the public portal for the purpose of private study or research.
- You may not further distribute the material or use it for any profit-making activity or commercial gain
- You may freely distribute the URL identifying the publication in the public portal

If you believe that this document breaches copyright please contact us providing details, and we will remove access to the work immediately and investigate your claim.

Ph.D. Thesis  
Doctor of Philosophy

 **DTU Physics**  
Department of Physics

# Light-matter interaction in low-dimensional materials

A theoretical study

Morten Niklas Gjerding

Kongens Lyngby 2016



**DTU Physics**  
**Department of Physics**  
**Technical University of Denmark**

Fysikvej  
Building 307  
2800 Kongens Lyngby, Denmark  
Phone +45 4525 3344  
info@fysik.dtu.dk  
www.fysik.dtu.dk



# Summary

---

In this thesis we have investigated the optical properties of layered and two-dimensional materials for application in the field of plasmonics and metamaterials using Density Functional Theory (DFT). Both of these fields, if successful in their goals, promise new technologies for small scale photonics beyond the diffraction limit. A technological breakthrough of such a caliber would have far reaching consequences such as enabling a practical interface to nano scale integrated electronic circuits or enable the construction of novel devices like a superlens with resolution well beyond diffraction limit. However, the progress of these fields is currently inhibited by large losses that can only be resolved through the discovery of new materials.

Using linear response time-dependent DFT we calculate the optical properties of several experimentally known layered transition metal dichalcogenides (TMDs) with the chemical formula of  $\text{MX}_2$  where M is a transition metal and X is a chalcogen atom (S, Se, Te). The TMDs constitute an interesting class of materials due to their diverse range of properties including both metals and semi-conductors. We find that the TMDs with group 5 transition metal atoms in the H monolayer exhibit a special bandstructure in which metallic bands are separated from other valence and conduction bands by finite energy gaps which has the potential to minimize the optical losses by reducing the density of states for scattering. The size of the energy gaps are, however, not sufficiently large to completely eliminate optical losses. We therefore propose a new class of layered materials with the chemical formula  $2\text{H-MXY}$  where M is a group 4 transition metal atom, X is a chalcogen atom, and Y is a halogen atom (Cl, Br, I) which increases the size of the energy gaps and significantly reduces optical losses. This entails improved plasmonic normalized propagation lengths and superior lifetimes compared to the best plasmonic material, namely, silver.

We show that all of the TMDs are natural hyperbolic materials, which means that they exhibit a strongly anisotropic dielectric response reflected by a sign-difference in their dielectric tensor resulting in hyperbolic isofrequency contours. Hyperbolic metamaterials obtain their anisotropic response from an artificial sub-wavelength structuring and are limited in their performance by the period of the structuring - the smaller, the better. In contrast, natural hyperbolic materials suffer no such limitation due to their lack of artificial structuring, and indeed, we find a much greater performance for all applications of hyperbolic materials.

The possibility of stacking individual two-dimensional materials into so-called van der Waals heterostructures is perhaps one of the most interesting technological devel-

opments in the field of two-dimensional materials. We show that effective medium theory for the dielectric properties of graphene and hexagonal boron nitride heterostructures, which treat the heterostructure as a continuous medium, break down for atomically thin layers due to quantum mechanical effects but also for thick components due to multiple reflection effects. We propose an extended version of effective medium theory to account for the interface layers and show that the effective medium description is improved.

The determination of the quality of materials for application within plasmonics and metamaterials requires an accurate calculation of the optical properties of materials which can be computationally demanding. To reduce the computational costs, the linear tetrahedron method and the employment of symmetries have been implemented which in some cases can reduce the computational costs by a factor of 200.

# Resume

---

Vi har i denne afhandling undersøgt de optiske egenskaber af lagdelte og to-dimensionelle materialer for deres anvendelse som plasmoniske- og meta-materialer ved brug af tætheds-funktional teori (density functional theory, DFT). Begge af disse felter lover nye teknologier indenfor nanoskala optik ved at bryde diffraktionsgrænsen. Et teknologisk gennembrud af en sådan kaliber vil have langtrækkende konsekvenser, blandt andet ved at muliggøre fabrikationen af et praktisk interface mellem elektroniske og optiske komponenter eller fabrikationen af banebrydende teknologier som en superlinse med opløsning der bryder diffraktionsgrænsen. Desværre er udviklingen i disse felter blevet hindret af store energi-tab i alle forslåede komponenter, som kun kan blive løses igennem opdagelsen af nye materialer.

Vi har beregnet, ved brug af lineær respons tidsafhængig DFT, de optiske egenskaber af adskillige eksperimentelt kendte lagdelte overgangsmetal-dichalcogenider (transition metal dichalcogenides, TMDs) med den kemiske formel  $MX_2$  hvor M er et overgangsmetal og X er et chalcogen atom (S, Se, Te). TMDerne udgør en interessant klasse af materialer da deres varierede egenskaber foresager at der både findes metaller og halv-ledere iblandt dem. Vi har fundet at TMDerne med gruppe 5 overgangsmetaller i H-monolagsstrukturen har specielle båndstrukturer hvor ledningsbåndet er separeret fra andre valens og ledningsbånd med endelige båndgab. Disse båndstrukturer reducere optiske tab ved at minimiere tilstandtætheden for spredning af elektroner, men gabene er desværre ikke store nok til fulstændig at eliminere tab. Vi foreslår derfor en ny klasse af lagdelte materialer med den kemiske formel  $2H-MXY$  hvor M er et gruppe 4 overgangsmetal, X er et chalcogen atom og Y er et halogen atom (Cl, Br eller I). Dette øger størrelsen af gabene og leder dermed til en betydelig reduktion af de optiske tab. Konsekvensen af denne reduktion er længere propagationslængder og større levetider for plasmoner sammenlignet med sølv, som hidtil har været det bedste materiale til sådanne formål.

Vi har vist at alle de undersøgte TMDer er naturligt hyperbolske materialer, hvilket betyder at deres dielektriske tensor udviser et stærkt anisotropisk respons, udmøntende i en fortegnforskkel blandt nogle komponenter, hvilket betyder at deres associerede isofrekvens-overflader bliver hyperbolske. Hyperbolske metamaterialer opnår deres anisotropiske respons fra en kunstig strukturering, som begrænser det hyperbolske respons til bølgelængder der er betydeligt længere end perioden af metamaterialet. Sådant en begrænsning lider naturligt hyperbolske materialer ikke under, og vi finder derfor de præsterer markant bedre end selv de bedste metamaterialer.

Muligheden for at stable individuelle to-dimensionelle materialer i såkaldte van der Waals heterostrukturer er måske en af de mest interessante teknologiske udviklinger indenfor 2D materiale fysik. Vi viser at effektiv medium teori bryder sammen i beskrivelsen af de dielektriske egenskaber af graphén/hexagonal bornitrid (hBN)-heterostrukturer når de individuelle komponenter når den atomare grænse. Dette sammenbrud er forårsaget af kvantemekaniske effekter, altså, hybridisering i grænselaget mellem graphén og hBN. Ved at tage højde for disse ændrede egenskaber i grænselagene foreslår vi en forbedret EMT model og viser, at denne leder til en bedre beskrivelse af de dielektriske egenskaber.

Bestemmelsen af kvaliteten af materialer indenfor optiske applikationer kræver en nøjagtig beregning af de optiske egenskaber hvilket typisk leder til beregningsmæssigt tunge programmer. For at reducere de beregningsmæssige omkostninger er symmetrier og den lineære tetraede integrationsmetode blevet implementeret hvilket i nogle tilfælde kan lede til en reduktion svarende til en faktor 200.

# Preface

---

This thesis is submitted in candidacy for the Ph. D. degree in physics from the Technical University of Denmark. The work was carried out at the Center for Atomic-scale Materials design (CAMd) at the Department of Physics in the period September 2013 to December 2016, under supervision of professor Kristian S. Thygesen. The Ph. D. project was funded by an internal scholarship from DTU and was affiliated with the Center for Nanostructured Graphene.

Kongens Lyngby, December 23, 2016

A handwritten signature in black ink, reading "Morten Niklas Gjerding". The signature is written in a cursive style with a large, sweeping 'M' at the beginning and a long, trailing 'y' at the end.

Morten Niklas Gjerding



# Acknowledgements

---

I am grateful to Kristian, my supervisor, for his guidance. I have been allowed a great influence and freedom during my project and it is safe to say that I have matured a lot from this experience. You have been understanding during the tough times.

I would like to thank René Petersen and his supervisor Thomas Garm Pedersen from Aalborg University for good collaboration and for their patience.

Marianne deserves a special thanks for her patience in me, especially in attending to official matters. As you once said in response to one of my countless apologies for my negligence, and I am paraphrasing from memory, 'You get to know your children' - I hope i haven't been too bad.

I am grateful for the understanding and support of my family and girlfriend Gertrud, both of whom have often suffered my absence, and I would like them to know that I could not have made it without them.

I am grateful to Jens Jørgen Mortensen for his insight and guidance in whatever challenges I have encountered in the implementation of the methods for calculating optical properties of matter.

Finally, I would like to thank all the people whom I have spent time with during my stay at CAMd. In no particular order, thank you Simone, Filip, Per, Kirsten, Mohnish, Nicki, Mohnish, Korina, Sten, Chengjun, Manuel, Kristian Ørnsø, Chris, Alexander, Rune, Keld, Jess, Thomas, Ivano, Martin, Ole, Marcin, Falco and Karsten.

As a consequence of writing both Bachelor, Master and now Ph. D. at CAMd, I consider CAMd my place of academic upbringing. Naturally, there will be many people to thank and I hope that I covered you all - if not, you are entitled to a beer at my expense!



# Contents

---

<b>Summary</b>	<b>i</b>
<b>Resume</b>	<b>iii</b>
<b>Preface</b>	<b>v</b>
<b>Acknowledgements</b>	<b>vii</b>
<b>Contents</b>	<b>ix</b>
<b>1 Introduction</b>	<b>1</b>
1.1 Plasmonics and metamaterials . . . . .	1
1.2 Outline . . . . .	2
<b>2 Nano-optics background</b>	<b>3</b>
2.1 Maxwell's equations . . . . .	3
2.2 Layered and two-dimensional materials . . . . .	5
2.3 Plasmonics . . . . .	9
2.4 Quantum emitters . . . . .	16
2.5 Hyperbolic metamaterials . . . . .	22
<b>3 Density Functional Theory Background</b>	<b>27</b>
3.1 The problem of the structure of matter . . . . .	27
3.2 Density Functional Theory . . . . .	29
3.3 Linear response theory for the dielectric function . . . . .	31
3.4 Optical properties from first principles . . . . .	33
<b>4 Summary of the results</b>	<b>35</b>
4.1 Paper I: Limitations of effective medium theory in multilayer graphite/hBN heterostructures . . . . .	35
4.2 Paper II: Bandstructure engineered metals for low-loss plasmonics . . . . .	36
4.3 Paper III: Layered materials with hyperbolic light dispersion . . . . .	37
<b>5 Papers</b>	<b>41</b>

---

5.1	Paper I: Limitations of effective medium theory in multilayer graphite/hBN heterostructures . . . . .	41
5.2	Paper II: Band structure engineered layered metals for low-loss plasmonics	52
5.3	Paper III: Layered van der Waals crystals with hyperbolic light dispersion	61
<b>6</b>	<b>Additional information</b>	<b>71</b>
6.1	Paper I: Limitations of effective medium theory in multilayer graphite/hBN heterostructures . . . . .	71
6.2	Paper II: Bandstructure engineered layered metals for low-loss plasmonics	74
6.3	Paper III: Layered materials with hyperbolic light dispersion . . . . .	86
<b>7</b>	<b>Implementation</b>	<b>91</b>
7.1	GPAW . . . . .	91
7.2	Python . . . . .	91
7.3	Calculating the response functions . . . . .	92
7.4	Linear tetrahedron method . . . . .	92
7.5	Symmetries of the dielectric function . . . . .	95
7.6	The irreducible Brillouin zone . . . . .	98
<b>8</b>	<b>Conclusion</b>	<b>101</b>
<b>9</b>	<b>Hull energies and HOF for MXY compounds</b>	<b>103</b>
	<b>Bibliography</b>	<b>105</b>

# CHAPTER 1

# Introduction

---

The central role played by materials science in the major technological breakthroughs throughout the history of human progress is indisputable. In the three-age system of archaeology, the human prehistoric ages were *named* according to the predominant choice of material that artefacts were made of: the Stone Age, Bronze Age and Iron Age. Other examples of materials discoveries that have led to significant advances in human history, including dynamite, cement, glass, concrete, electrical conductors, and steel, are too numerous to exhaust. It is difficult to say what the next scientific breakthrough will be, but it seems certain that it starts with the discovery of novel materials. The possible strategies for the exploration for novel materials can be divided into three categories: experimental, analytic and computational. In this work we take the strategy of computational materials science. By employing theoretical and computational methods we are able to explore the properties of synthesized and yet-to-be synthesized materials for potentially any application we deem interesting. This strategy aids and guides experimental scientists in their search for novel materials by providing detailed information that is not readily available in an experimental setup.

## 1.1 Plasmonics and metamaterials

As the feature size of integrated electronic circuits has reached the nanometer scale, the delay of the electrical interconnects that transport information across electronic chips over centimetre scales poses severe limitations to the achievable processing speeds of integrated circuits. This limitation has nourished the interest in replacing electronic interconnects with optical interconnects that are able to carry more information at greater speeds. However, an inherent problem of optical fields that stops the immediate transfer to optical interconnects is the diffraction limit which restricts the degree to which light can be confined, and sets a minimum size on the optical components employed typically in the micrometer scale which is challenging to interface with the nanometer scale integrated electronic circuits[1].

The field of Plasmonics (Chap. 2) presents a potential solution to this problem by offering a way to guide electromagnetic energy on metallic structures that are not limited by the diffraction limit[2]. Unfortunately, most applications of plasmonic subwavelength structures have so far been dominated by ohmic (resistive) losses which can only be resolved through the discovery of new materials with lower intrinsic losses[3].

The potential applications of plasmonics extend further and enable the construction of artificially structured metamaterials that exhibit an unnatural response to light. For example, a metamaterial that consists of nanometer thin alternating layers of metal and dielectric exhibits properties that could be used to implement lenses that are not limited by the diffraction limit[4].

The material of tomorrow is perhaps to be found in the new class of two-dimensional (2D) materials that have only recently been discovered; the original and most famous example of which is graphene, a single sheet of carbon atoms arranged in a honeycomb lattice[5]. However, many other materials have since been discovered and synthesized[6]. The 2D character of the materials often provide them with novel properties unparalleled in three-dimensional crystals and give researchers microscopic control to engineer extremely compact devices, which might be the key enable the construction of even smaller integrated electronic circuits.

## 1.2 Outline

The first chapters (Chap. 2 and 3) present the necessary background information needed to understand the papers of the thesis. Chapter 4 presents summaries of the papers highlighting the most significant results. Chapter 5 presents the papers and Chapter 6 supplies additional information not contained in the papers. Finally, Chapter 7 details the implementation of the computational methods employed.

# CHAPTER 2

# Nano-optics background

---

The study of optical phenomena at the nanometer scale has intensified due to the recent advances in nanofabrication methods that make it possible to fabricate structures with nano-meter scale features[7]. In nano-optics the goal is to understand and utilize the interaction of light with these nano-scale components for a vast array of applications[8]. The field of nano-optics encompasses other scientific fields such as plasmonics[9, 10] and metamaterials[11–14]. In plasmonics, metallic components are set up to interact with light in a way that enables a much greater focussing of light compared to vacuum where focussing is limited by the diffraction limit[1, 15, 16], entailing the possibility for light to interact selectively with nanoscale features[2]. Artificial metamaterials, or simply metamaterials, are materials that have been structured on a microscopic scale with the goal of engineering an effective (and often unusual) response to light, in some cases with the goal of achieving an effective negative refractive index[17].

The central message that this chapter seeks to convey is the need for new materials for plasmonic and metamaterial applications to reduce energetic losses. Besides giving an introduction to the fields of plasmonics and metamaterials, this chapter describes how progress in these fields currently is inhibited by large ohmic losses occurring in the metallic components of practical devices.

## 2.1 Maxwell's equations

In classical physics electric fields ( $\mathbf{E}(\mathbf{r}, t)$ ) and magnetic fields ( $\mathbf{B}(\mathbf{r}, t)$ ) are described by Maxwell's equations, a set of inhomogeneous differential equations containing two source terms, the charge density  $\rho(\mathbf{r}, t)$  and the current density  $\mathbf{J}(\mathbf{r}, t)$ . These densities substitute the discrete microscopic nature of the electrons within real materials by continuous quantities which is why the equations are sometimes denoted as Maxwell's macroscopic equations[8, 10, 18]. In the presence of metals and dielectrics bound charges and currents will be induced, which makes it convenient to introduce the auxiliary fields known as the displacement field  $\mathbf{D}$  and the magnetizing field  $\mathbf{H}$  defined

by  $\mathbf{D} = \varepsilon_0 \mathbf{E} + \mathbf{P}$  and  $\mathbf{H} = \mu_0^{-1} \mathbf{B} - \mathbf{M}$ , where  $\mathbf{P}$  the polarization density and  $\mathbf{M}$  is the magnetization. Here  $\mu_0$  is the vacuum permeability and  $\varepsilon_0$  is the vacuum permittivity. The auxiliary fields serve the purpose of reducing the source terms of Maxwell's equations to quantities that are controllable in experiments, i.e., the free charge concentration  $\rho_f$ . Only non-magnetic materials are considered in this thesis so we neglect the magnetization,  $\mathbf{M} = 0 \Rightarrow \mu_0 \mathbf{H} = \mathbf{B}$ . With these simplifications Maxwell's equations become

$$\nabla \cdot \mathbf{D} = \rho_f \quad (\text{Gauss' Law}), \quad (2.1)$$

$$\nabla \cdot \mathbf{B} = 0, \quad (2.2)$$

$$\nabla \times \mathbf{E} = -\partial_t \mathbf{B} \quad (\text{Faraday's law}), \quad (2.3)$$

$$\mu_0^{-1} \nabla \times \mathbf{B} = \mathbf{J} + \partial_t \mathbf{D} \quad (\text{Ampere's law}). \quad (2.4)$$

### 2.1.1 The dielectric function

To make further progress, it is necessary to assume a dependence of the polarization density, or equivalently the displacement field on the electric field. For so-called linear materials, the relation between the electric field and the displacement field is approximated as

$$\mathbf{D} = \varepsilon \varepsilon_0 \mathbf{E}. \quad (2.5)$$

This introduces the dielectric function,  $\varepsilon$ , which turns out to be the central object in the description of optical properties of linear materials. For conductive materials the dielectric function is normally generalized to include current response of the material in which case it becomes a complex number. This can be seen by introducing  $\mathbf{J} = \sigma \mathbf{E}$  into Ampere's law Eq. (2.4) and Fourier transforming ( $f(t) = \int_{-\infty}^{\infty} d\omega f(\omega) e^{-i\omega t}$ ) to give

$$\mu_0^{-1} \nabla \times \mathbf{B} = \mathbf{J}_f - i\omega \varepsilon_0 \left( \varepsilon + \frac{i\sigma}{\omega} \right) \mathbf{E} = \mathbf{J}_f - i\omega \varepsilon_0 \tilde{\varepsilon} \mathbf{E}, \quad (2.6)$$

where the complex dielectric function  $\tilde{\varepsilon} = \left( \varepsilon + \frac{i\sigma}{\omega} \right)$  has been introduced. It is usual to neglect the tilde and generally refer to the complex dielectric function as simply the dielectric function. Using that the refractive index is related to the dielectric function as  $n = \sqrt{\varepsilon}$  it is straightforward to show that a finite imaginary part of the dielectric function leads to the absorption of a propagating plane-wave with a wave-number  $k = n\omega/c$  in a homogeneous medium propagating along the  $z$ -axis

$$\mathbf{E} = \mathbf{E}_0 e^{-izk_0 n} = \mathbf{E}_0 e^{iz\omega \sqrt{\varepsilon}/c} = \mathbf{E}_0 e^{iz\omega \text{Re}\sqrt{\varepsilon}/c} e^{-z\omega \text{Im}\sqrt{\varepsilon}/c}. \quad (2.7)$$

Here the decay length is proportional to  $1/\text{Im}\sqrt{\varepsilon}$ .

In the case of anisotropic media where the induced polarization and current is dependent on the polarization of the electric field, the dielectric function must be

described as a tensor, i.e.,

$$\mathbf{D} = \overleftrightarrow{\epsilon} \epsilon_0 \mathbf{E}. \quad (2.8)$$

Maxwell's equations can be combined to yield the form of a wave equation which will be used later to understand the properties of propagating waves in anisotropic media. It is derived by taking the curl of Faradays law Eq. (2.3), inserting into Eq. (2.4), using the constitutive relation for the displacement field in anisotropic linear media Eq. (2.8) and Fourier transforming ( $f(\mathbf{r}) = \int d\mathbf{k} f(\mathbf{k}) e^{i\mathbf{k}\cdot\mathbf{r}}$ ) resulting in[19]

$$-|\mathbf{k}|^2 \mathbf{E} + k_0^2 \overleftrightarrow{\epsilon} \mathbf{E} + \mathbf{k}(\mathbf{k} \cdot \mathbf{E}) = 0. \quad (2.9)$$

where the identity  $\nabla \times \nabla \times = |\nabla|^2 - \nabla \nabla$  have been employed and  $k_0^2 = \frac{\omega^2}{c^2}$  is the free space wave number. A similar wave equation can be derived for the magnetic field but will not be presented here.

## 2.2 Layered and two-dimensional materials

In this thesis we investigate the optical properties of several layered materials and their merits in plasmonic and metamaterial applications. As shown in Figure 2.1, layered materials are anisotropic materials characterized by the fact that they can be viewed as a collection of tightly bound atomic sheets bound together by weak van der Waals forces to form a bulk material. Over the past decade, layered materials have found themselves in the spotlight of mainstream science because of the discovery that single layers, that exhibit novel physical properties due to their reduced dimensionality, can be exfoliated from bulk layered crystals[20, 21]. Starting from graphite, the first two-dimensional material to be synthesized was graphene[22, 23] (Fig. 2.1(a)), a single sheet carbon atoms arranged in a honeycomb lattice with a thickness of approximately 3 Å. Certainly, the property of graphene that most of its interesting physical attributes can be assigned to is its special electronic structure[5, 24], namely, it being a semi-metal with light-like linear dispersion, entailing properties such as large electron and hole mobilities. Since then, many other two-dimensional materials have been discovered that exhibit a diverse range of electronic properties including metals, semimetals, semiconductors and insulators[20, 25]. Monolayer hexagonal boron nitride (Fig. 2.1(b)), for example, is a large bandgap insulator[26]; a property it has in common with its bulk counterpart.

Of particular interest to this work have been the class of layered materials known as transition metal dichalcogenides (TMDs)[27, 28]. The TMDs consist of one transition metal atom M for every two chalcogen atoms X ( $\text{MX}_2$ ) as shown in Fig. 2.1(c) for the case of 2H-TaS<sub>2</sub>. The TMDs are distinguished from other layered materials such as graphite and hexagonal boron nitride in that each monolayer can be viewed as a collection of three stacked monolayers in the order: chalcogen layer, transition metal layer, chalcogen layer. Aside from some rare exceptions, TMDs are observed in three bulk structures: 1T (Fig. 2.1(d)), 2H (Fig. 2.1(e)) and 3R (Fig. 2.1(f)), where the

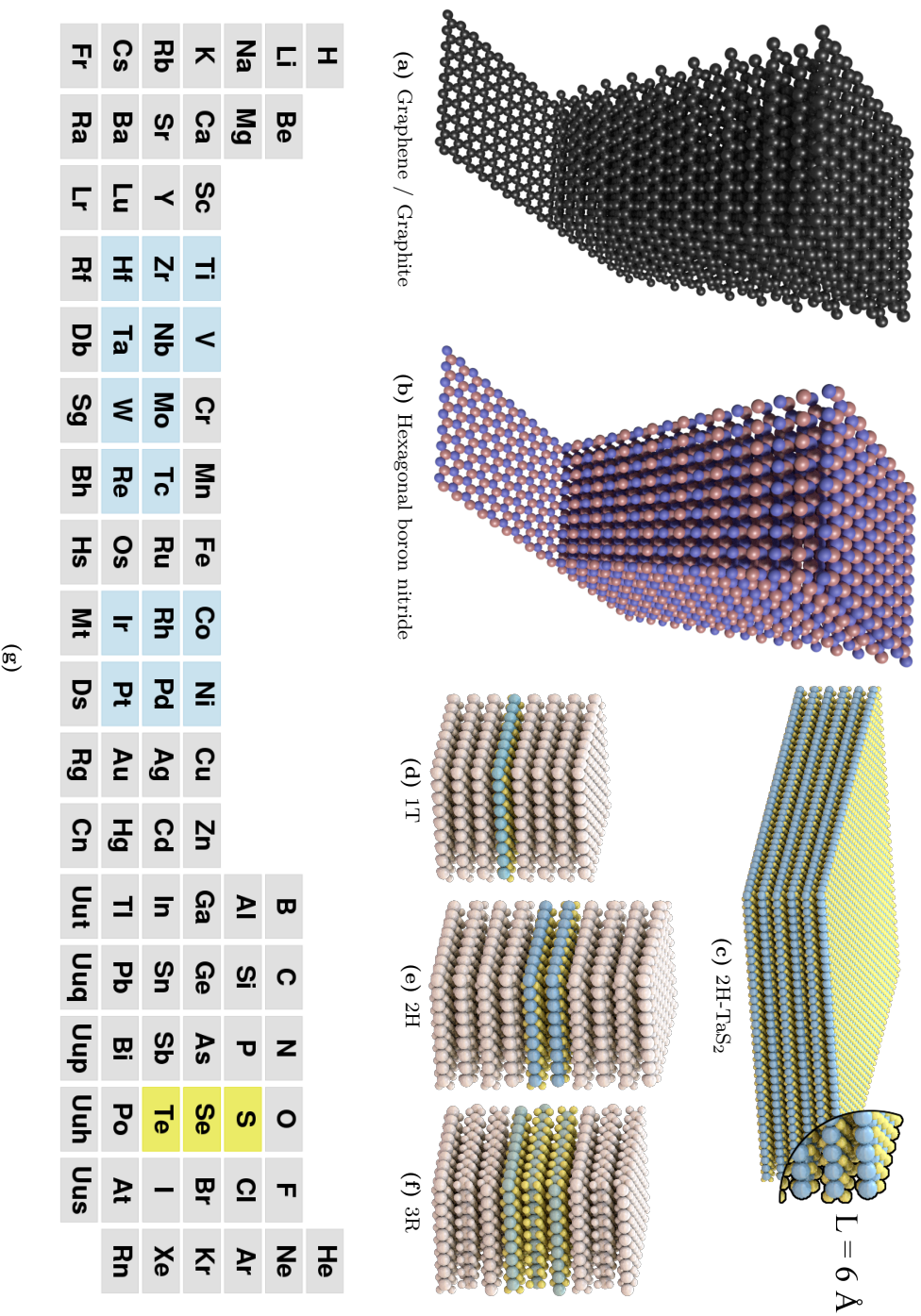


**Figure 2.1:** (a-c) Examples of layered materials. (d-f) The different polymorphs that the TMDS are commonly found in. The colored atoms indicate the number of layers in a unit cell. (g) The periodic table shows the transition metal atoms (blue) that when combined with the chalcogen atoms (yellow) compose the experimentally observed TMDS.

numbers indicate the number of monolayers in the unit cell of the bulk crystal and the letters refer to the symmetry of the crystal[28]. The experimentally known transition metal dichalcogenides are marked by blue (transition metal) and yellow (chalcogen) in the periodic table of Fig. 2.1(g)[28].

The TMDs span a wide variety of electronic properties including both metallic compounds (such as 2H-TaS<sub>2</sub>) and semi-conducting compounds (such as 2H-MoS<sub>2</sub>). These diverse properties can be understood from the filling of the transition metal d-orbitals as shown in Figure 2.2[28]. The crystal field breaks the degeneracy of the transition metal d-states into degenerate chunks (irreducible representations) depending on the phase, and the position of the Fermi level (dashed lines) is determined by filling in the number of d-electrons of the transition metal atom. The most drastic consequence of this splitting is perhaps that T-MoS<sub>2</sub> is metallic (Fig. 2.2(a)) while H-MoS<sub>2</sub> is semi-conducting (Fig. 2.2(b)) as also observed in experiments[29].

The possibility of stacking individual atomic layers into so-called van der Waals heterostructures (Fig. 2.3) is perhaps one of the most exciting opportunities that 2D materials provide[30]. The weak van der Waals's bonding relaxes the conditions of lattice matching which means that virtually all two-dimensional materials can be combined. For example, being a large bandgap insulator hexagonal boron nitride is often employed in heterostructures to protect other two-dimensional materials from the environment by, for example, providing protection from oxidation[31] or minimizing the coupling of plasmons to the environment[32]. For the purposes of this thesis, we will later show how heterostructuring enables the fine tuning of optical properties for various optical applications.

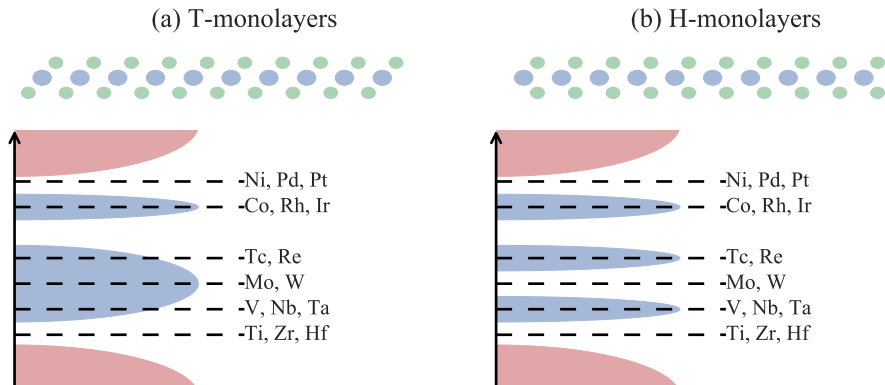


**Figure 2.2:** Electronic density of states of monolayer TMDs in (a) the T-phase and (b) the H-phase. The crystal field breaks the degeneracy of the transition metal d-states (blue) and the Fermi level (dashed lines) is determined by the number of d-electrons provided by the transition metal atom. The bonding anti-bonding states are marked by red but are not essential for the present discussion.

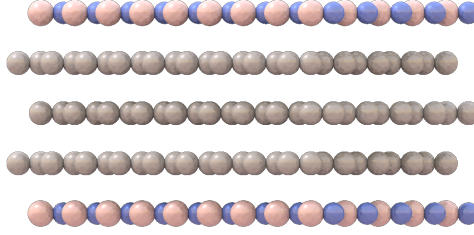


**Figure 2.3:** Graphene-hexagonal boron nitride heterostructure.

In this work, we almost exclusively consider the layered counterparts of the two-dimensional materials, however, much of the insight above can be used to understand the properties of the layered materials. Layered materials are not strictly two-dimensional, but due to the weak van der Waal's forces the interlayer bonding distances are typically larger than covalently and ionically bonded crystals. The longer bonding distance reduces the electronic hybridization between adjacent layers and increases the confinement of the electrons to each layer. The electronic properties of layered materials can thus be considered to be in-between those of a three-dimensional material and a two-dimensional material, due to the inhibited interlayer electronic motion.

From the point of view of optics, layered materials fall under a category of materials known as uniaxial media[11]. Materials of this kind are characterized by the fact that they possess a symmetry axis, known as the "optic axis", about which they are rotationally invariant, meaning that their dielectric tensor possess two independent components, known as the ordinary and extra-ordinary components. Light rays propagating along the optic axis (thus polarized perpendicular to the optic axis) experience the "ordinary" component and light-rays whose polarization is along the optic axis experience the extra-ordinary component. In the context of layered materials, it is useful and more intuitive to relabel to components of the dielectric tensor to "in-plane" ( $\parallel$ ) and "out-of-plane" ( $\perp$ ) for "ordinary" and "extra-ordinary". This means that we write the dielectric tensor of a layered material as

$$\varepsilon = \begin{bmatrix} \varepsilon_x & 0 & 0 \\ 0 & \varepsilon_y & 0 \\ 0 & 0 & \varepsilon_z \end{bmatrix} = \begin{bmatrix} \varepsilon_{\parallel} & 0 & 0 \\ 0 & \varepsilon_{\parallel} & 0 \\ 0 & 0 & \varepsilon_{\perp} \end{bmatrix}. \quad (2.10)$$

The dispersion of light in uniaxial materials is given by Eq. (2.9) and by setting its determinant to zero

$$(|\mathbf{k}|^2 - k_0^2 \varepsilon_{\parallel}) \left( \frac{k_{\perp}^2}{\varepsilon_{\parallel}} + \frac{k_{\parallel}^2}{\varepsilon_{\perp}} - k_0^2 \right) = 0 \quad (2.11)$$

two distinct solutions are found corresponding to different electric field polarizations. The transverse electric (TE/s-polarized) mode has its electric field polarization per-

pendicular to the optic axis and thus only experience the in-plane dielectric function, whereas the transverse magnetic (TM/p-polarized) mode has its magnetic field polarized perpendicular to the optic axis. The dispersion relations for these two modes are

$$|\mathbf{k}|^2 = k_0^2 \varepsilon_{\parallel} \quad (\text{TE}), \quad (2.12)$$

$$\frac{k_{\perp}^2}{\varepsilon_{\parallel}} + \frac{k_{\parallel}^2}{\varepsilon_{\perp}} = k_0^2 \quad (\text{TM}). \quad (2.13)$$

Most interesting optical properties of uniaxial materials are related to the dispersion of TM-polarized light within the material and we shall rarely discuss the TE-modes.

## 2.3 Plasmonics

The field of plasmonics study the interaction of electromagnetic radiation with metallic nanostructures and surfaces[10]. The strong interaction of electromagnetic fields with the conduction electrons of metallic structures entail a significantly different behaviour than the behaviour of electromagnetic fields in dielectrics, in particular, it offers the possibility to break the diffraction limit and confine electromagnetic fields to very small length scales[16]. This will be necessary if we are ever to achieve a practical interface to integrated electronic circuits which, due to the ever decreasing feature size now approaching the nano-meter scale, could benefit from the fast and nearly lossless transfer of information that traditional photonic components offer [1, 33]. Besides providing confinement, metallic subwavelength structures can be used to guide electromagnetic energy in equivalence to photonic wave guides[15, 34]. Other applications of plasmonic components include the possible improvement of in the resolution of microscopes (superlensing)[35, 36], quantum information processing[37] and energy conversion [38], to name a few.

### 2.3.1 Surface plasmon polaritons

On a fundamental level, the extreme localization of electromagnetic energy is enabled by the existence of a special resonant state of matter, confined to the metal-dielectric interface, known as a surface plasmon[39]. A surface plasmon is a self-sustained oscillation of the charge density at the surface of a metal which when coupled with light forms a propagating mode known as a surface plasmon polariton (SPP). 'Self-sustained' means that they are solutions of Maxwell's homogeneous equations, i.e., in the absence of sources. A trivial example of a self-sustained mode supported by the source-less Maxwell equations is light which relies on the restoring force of the displacement current in Ampere's law to enable its self-sustenance. In contrast, the restoring force that enable the self-sustenance of SPPs is the long range interaction of charges, known as the Coulomb interaction, acting on the oscillating charges. Their existence emerge from a fully quantum mechanical framework[40] and as such can be

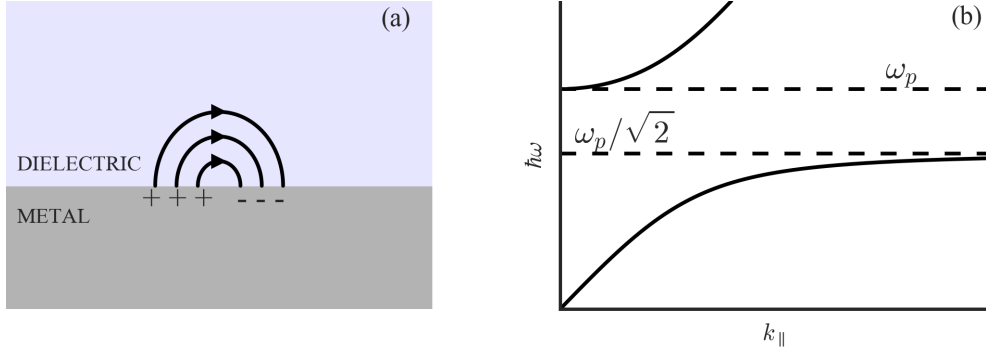


**Figure 2.4:** A sketch of (a) the electric field of a surface plasmon polariton and (b) its dispersion relation (in vacuum) where  $\omega_p$  is the plasma frequency.

viewed as quasi-particle excitations. However, because the plasmon originates from the long range interaction of the Coulomb force it is possible to derive most properties of SPPs directly from Maxwell's equations. The physical situation is sketched in 2.4(a). Starting from the ansatz of a localized SPP

$$\mathbf{E}_j = (E_{j\parallel}\hat{\mathbf{x}} + E_{j\perp}\hat{\mathbf{z}})e^{ik_{\parallel}x}e^{ik_{j\perp}z}e^{-i\omega t}, \quad (2.14)$$

where  $j \in 1, 2$  indicates the upper and lower half spaces, the resulting dispersion relation become[8]

$$k_{\parallel}^2 = \frac{\varepsilon_1\varepsilon_2}{\varepsilon_1 + \varepsilon_2}k_0^2, \quad (2.15)$$

$$k_{j\perp}^2 = \frac{\varepsilon_j^2}{\varepsilon_1 + \varepsilon_2}k_0^2. \quad (2.16)$$

By demanding that the in-plane wave vector be real and the out-of-plane component be imaginary the existence conditions for the SPPs become

$$\varepsilon_1\varepsilon_2 < 0 \quad (2.17)$$

$$\varepsilon_1 + \varepsilon_2 < 0, \quad (2.18)$$

in the case of real dielectric functions. The optical properties of a metal are mostly determined by the free conduction electrons of the metal which to a good approximation can be described as a free electron plasma. This leads to the Drude-Sommerfeld model for the dielectric function of a metal[8]

$$\varepsilon_{\text{Drude}} = 1 - \frac{\omega_p^2}{\omega(\omega + i\eta)}, \quad (2.19)$$

where  $\omega_p$  is known as the plasma-frequency and  $\eta$  as the relaxation rate of the free carriers which represent ohmic losses in the metal. The SPP dispersion relation is presented in Fig. 2.4(b).

A commonly discussed geometry for plasmonic wave guiding is the metallic thin film[39] (Fig. 2.5). Light in metallic thin films behave fundamentally different than dielectric planar wave guides in that the fundamental wave guiding mode becomes *more* confined as the thickness is decreased[41]; an advantageous feature if nano-scale optics is to become reality. The single-interface SPP model gives a good description of SPPs on interfaces of thick metal films, however, as the thickness of the film decreases the SPPs on the two interfaces hybridize into a symmetric and an anti-symmetric mode (Fig. 2.5(a,b)) with dispersion relations given by[39, 42] (Fig. 2.5(c))

$$\varepsilon_1 k_{2,\perp} + \varepsilon_2 k_{1,\perp} \tanh(k_{1,\perp} d/2) = 0, \quad \text{anti - symmetric mode}, \quad (2.20)$$

$$\varepsilon_1 k_{2,\perp} + \varepsilon_2 k_{1,\perp} \coth(k_{1,\perp} d/2) = 0, \quad \text{symmetric mode}. \quad (2.21)$$

The light-like character of the anti-symmetric mode entails fast group velocities and small skin-depths into the metal leading to long plasmon propagating lengths on the order of centimeters[43] but also weak field confinements as the effective refractive index is on the order of the free space refractive index ( $k_{\parallel}/k_0 \sim 1$ ). Due to the long propagation length, the anti-symmetric mode is often known as the long-range SPP (LRSPP). The symmetric mode offers great field confinement but slower group velocities, and therefore shorter propagation lengths [44]. Due to the shorter propagation length, this mode is typically known as the short-range SPP (SRSP)[45, 46]. The greater field confinement comes at the prize of greater metallic skin depth which typically entails greater losses. In this thesis, we study the properties of some layered materials in the thin film wave guide geometry and show that they offer some benefits over the noble metal wave guides.

### 2.3.2 Origin of losses in plasmonics

Even though the field of plasmonics now is more than a decade old, the promises of plasmonics[2] have remained unfulfilled and the status of the field is currently that energetic losses in plasmonic devices are too large for nearly all practical applications[3]. Eliminating losses in plasmonic waveguides with weak field confinement (employing the LRSPP) using gain materials have shown some promise[47], however, when the field confinement increases extremely large injection current densities are required[48] which questions the practicality of approaches based on gain materials. Through general considerations of the energy balance of an electromagnetic field confined to subwavelength length scales Khurgin and Sun [49] have shown that a self-sustained subwavelength field dissipates at the rate of the losses in the metal *regardless* of the geometry of the plasmonic component. As a consequence, the problem of losses is actually a problem of materials science, i.e., the only way low-loss plasmonic components can be obtained is by engineering materials to minimize intrinsic ohmic losses[3]. However, even with the large efforts already spent in the search for better plasmonic

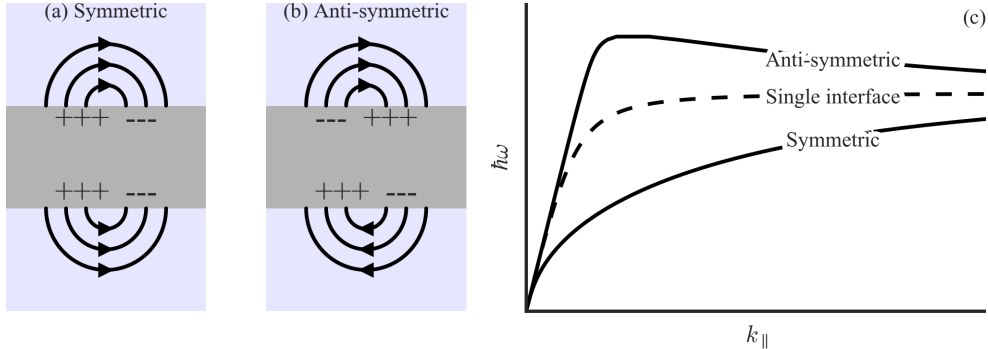


**Figure 2.5:** Sketch of the (a) symmetric and (b) anti-symmetric SPP modes in a metallic thin film and (c) their dispersion relations..

materials[50–54], the metals employed in plasmonic components remain the noble metals that was originally employed[55].

As shown previously, optical losses are related to a finite imaginary part of the dielectric function. In more general terms, absorption is described by the work done by the electric field on charge carriers in a material (Poynting's theorem),  $W = \int d\mathbf{r} \mathbf{J}(\mathbf{r}) \cdot \mathbf{E}(\mathbf{r})$ . Through  $\mathbf{J} = \text{Re}\sigma\mathbf{E} = \omega\text{Im}\varepsilon\mathbf{E}$  losses are seen to be directly proportional to the imaginary part of the dielectric function

$$W = \omega \int d\mathbf{r} \text{Im}\varepsilon |\mathbf{E}(\mathbf{r})|^2. \quad (2.22)$$

The Drude model Eq. (2.19) introduced the relaxation rate which was seen to yield a finite frequency-dependent imaginary part of the dielectric function

$$\text{Im} \varepsilon_{\text{Drude}} = \frac{\omega_p^2}{\omega^3} \eta. \quad (2.23)$$

In this model the relaxation rate is a phenomenological constant, introduced to account for the losses that are inevitably observed in experiment. It describes losses due to all scattering mechanism that exists including phonon-scattering, impurity scattering, electron-electron scattering. For simple metals such as sodium, copper, silver and gold, the relaxation rate is well-approximated as a constant[56], but for other materials it may significantly depend on the frequency of the electromagnetic field. Indeed, as we show in this thesis, the constant relaxation rate approximation is not a good approximation for layered materials.

In electronic structure theory, optical losses can be understood as the generation of electron-hole pairs within the absorbing material[3]. Whether or not electron-hole

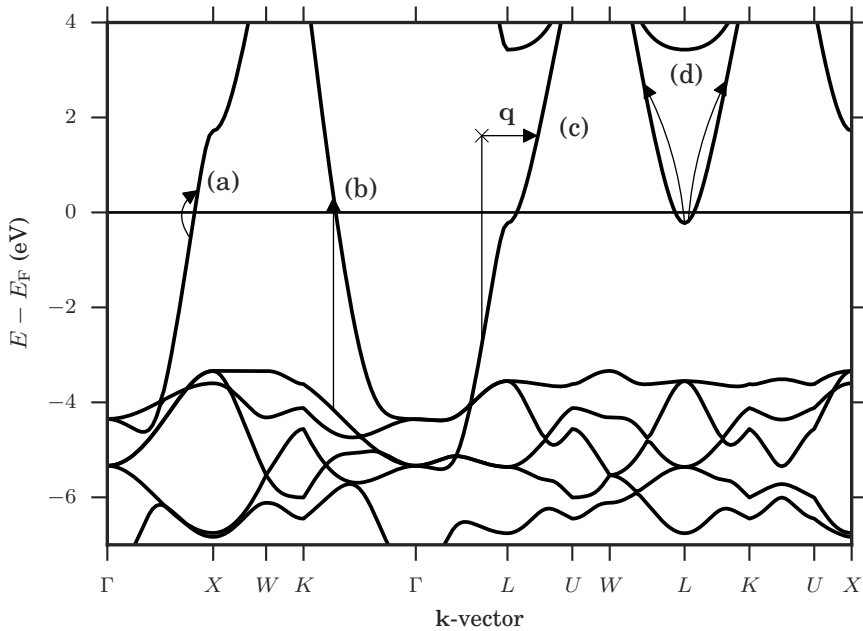


**Figure 2.6:** Bandstructure of silver calculated with DFT using the GLLBSC functional. Absorption of electromagnetic radiation can be understood as the generation of electron-hole pairs. For high frequencies, losses are dominated by (b) interband transitions. For smaller frequencies the losses are dominated by other scattering mechanisms such as (c) impurity scattering and (d) electron-electron scattering that provide the required momentum to induce losses..

pairs can be excited depend on the electronic structure of the specific material. Figure 2.6 shows the electronic bandstructure of silver as calculated by density functional theory (see Chap. 3). In this picture an absorbed photon excites an electron from an occupied state  $E < E_F$  to an unoccupied state  $E > E_F$  (Fig. 2.6(a)) leaving a hole behind. In the absence of scattering mechanisms only vertical transitions are allowed due to the translational symmetry of the crystal along with the negligible photon momentum (Fig. 2.6(b)). Such transitions are known as interband transitions and the lowest energy interband transition is denoted the 'interband onset'. Losses are typically large above the interband onset which limits the operating regime to frequencies below the interband onset. For silver the experimental interband onset is between 3.5 and 4 eV[57]. For frequencies smaller than the interband onset an additional momentum must be provided to induce losses (Fig. 2.6(c)). Electron-phonon scattering provides the additional momentum by absorbing (or emitting) a

phonon, and in the case of impurity scattering the extra momentum is provided by breaking the translational invariance. Finally, electron-electron scattering (Fig. 2.6(d)) can lead to losses even in the absence of crystal inhomogeneities, however, the total momentum must be conserved as indicated.

### 2.3.3 Searching for new materials

The Drude model predicts that losses are proportional to the square of the plasma frequency and directly proportional to the relaxation rate, Eq. (2.23). This insight has guided the previous search for plasmonic materials[54] by showing that losses can be reduced by reducing the plasma frequency and, unsurprisingly, by reducing the relaxation rate. Highly doped semiconductors such as silicon, germanium, III-V semiconductors, transparent conducting oxides, perovskite oxides and non-stoichiometric oxides and sulfides have been investigated previously as alternative plasmonic materials[54]. The limiting factor is typically the solid solubility of the donors in the semiconductor which limits how large the plasma frequency can become. The best performance is typically found in the mid-infrared. In addition to reducing the plasma frequency, the relaxation rate might also be reduced due to a reduced density of states for scattering originating from the low density of states at the fermi-level of doped semi-conductors[58]. Instead of doping semiconductors to increase the plasma frequency it has also been investigated whether metals could be diluted with the goal of reducing the plasma frequency and therefore also the losses[54]. None of these materials unfortunately outperform silver at the moment but show similar performance to gold. The properties of two-dimensional materials are different than their three-dimensional competitors and this may well provide new opportunities and applications for the field of plasmonics, especially in terms of dynamically tuning their plasmonic properties[59]. The research on two-dimensional plasmonic materials have until this point almost exclusively investigated graphene[60, 61] which shows operation frequencies in the mid infrared regime.

Few computational studies on the design of new materials for plasmonics have been performed[51, 62]. Blaber, Arnold, and Ford [62] investigated the alkali-noble intermetallics and identify one material, namely KAu, that outperform gold. The few computational studies are probably due to the difficulties in estimating the relaxation rates due to different scattering processes which makes it a formidable challenge to obtain high quality results from first principles.

The detrimental effect that losses seems to have on most plasmonic applications led Khurgin and Sun [63] to ask the question of whether losses were fundamentally unavoidable in all applications of plasmonics. They discovered that it is indeed theoretically possible for a material to have a metallic response in certain spectral regions without having any losses. However, it requires that the metal has a characteristic band-structure, where the metallic bands are narrow and separated from other bands by finite band gaps (Fig. 2.7 (a)). If a metal has such a band structure and the gaps are sufficiently big there will exist frequencies where no direct or indirect electron-

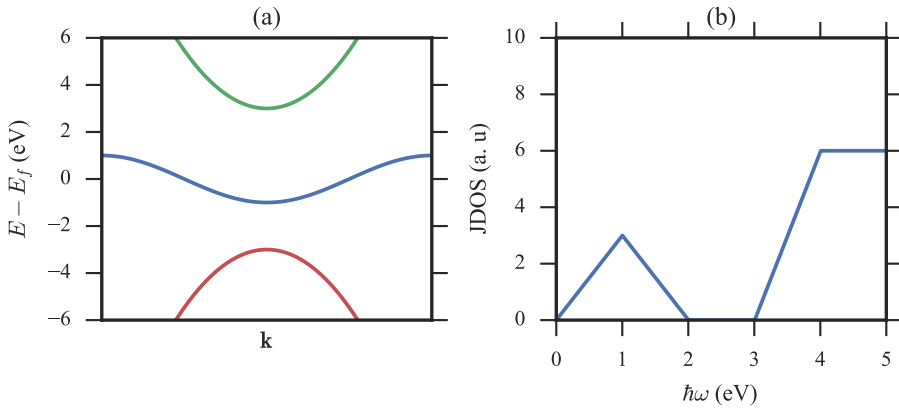


**Figure 2.7:** (a) Proposed model bandstructure of the elusive loss-less metal. This special bandstructure character greatly suppress the (b) JDOS at finite frequencies and thus potentially also also the density of states for scattering.

hole pair excitations are possible. This is represented in the density of states for electron-hole pairs, i.e., joint density of states (JDOS),

$$\text{JDOS}(\omega) = \int d\omega' n_{\text{occ}}(\omega') n_{\text{unocc}}(\omega' + \omega), \quad (2.24)$$

where  $n_{\text{occ}}$  and  $n_{\text{unocc}}$  are the occupied and unoccupied density of states, as a region with  $\text{JDOS} = 0$  (Fig. 2.7 (b)) meaning that all elastic first order scattering processes (i.e., scattering processes where only one electron-hole pair is created) are forbidden. Khurgin and Sun termed their model the 'elusive loss-less metal'. The question of whether metals with such bandstructures can exist in nature was unclear but they showed that by increasing the lattice constant in a sodium crystal, thus decreasing the hybridization between neighboring atoms, the necessary bandstructure was obtained for a loss-less plasmonic metal.

The quality of a particular plasmonic material depends on the specific application that is considered. For plasmonic waveguides a typical figure of merit (FOM) is the decay length normalized by the wavelength, i.e.,  $\text{Re}k_{\parallel}/\text{Im}k_{\parallel}$  [50], describing the number of wavelengths the SPP travels before it decays, which is used in our work to assess the performance of the layered materials for plasmonic wave guiding.

In applications where the fundamental excitation is not a plasmon other figures of merit have to be employed. In transformation optical applications [14], the goal is to engineer an optical field through the bulk of a material the fundamental excitation is therefore light and the typical FOM employed is simply the inverse of the optical

losses  $(\text{Im}\epsilon)^{-1}$  along with the criterium that the absolute value of the permittivity is on the order of one[50].

## 2.4 Quantum emitters

An integral part of achieving integrated electronic-photonic circuits is the ability to create reliable photon sources that can emit single photons at any time the user requires[64]. To obtain such a photon source requires the optimization many factors but here the focus will be on the subsequent emission of a photon given an initially excited quantum emitter. To fulfil the requirement of an on-demand supply of single photons it is necessary to be able to engineer single emitters to have large emission rates[65]. This section introduces the key concept of the local photonic density of states (PDOS) describing the number of photonic modes at any point in space. The relevance of the PDOS becomes clear when it is shown that the spontaneous emission rate of a quantum emitter is proportional to the value of the local PDOS at its position which can be influenced by placing the emitter in the vicinity of a photonic structure like a planar interface. In other words the spontaneous emission rate of a quantum emitter can be increased by increasing PDOS at the position of the emitter[8]. Its relation to this thesis becomes clear when we show that most layered materials exhibit very large PDOSs in finite spectral regions which provides a way of increasing the spontaneous emission rate.

As with plasmonics, many of the relevant properties of single photon emitters can be calculated from classical electromagnetism which is surprising because spontaneous emission is a true quantum mechanical phenomenon that cannot be derived from classical physics. The explanation is that while the quantum emitter itself cannot be described classically, the PDOS can, which means that the enhancement of the spontaneous emission rate (known as the Purcell effect) can be described classically.

### 2.4.1 Dyadic Green's Functions

The first step to introducing the PDOS is to introduce the Green's function of Maxwell's equations, known as the Dyadic Green's Function (DGF) to reflect the vector nature of the sources and fields. The DGF provides a simple tool for calculating the electromagnetic field distribution in the presence of arbitrary current and charge sources. The electric and magnetic fields are written in terms of the vector potential  $\mathbf{A}$  and electric potential  $\phi$

$$\mathbf{E}(\mathbf{r}) = i\omega\mathbf{A}(\mathbf{r}) - \nabla\phi(\mathbf{r}) \quad (2.25)$$

$$\mathbf{H}(\mathbf{r}) = \frac{1}{\mu\mu_0}\nabla\times\mathbf{A}(\mathbf{r}). \quad (2.26)$$

Choosing the Lorentz gauge for the vector potential  $\nabla\cdot\mathbf{A}(\mathbf{r}) = i\omega\mu_0\mu\epsilon_0\epsilon\phi(\mathbf{r})$  and introducing equations (2.25) and (2.26) into Ampere's law four scalar Helmholtz equa-

tions can be written, one for each of the components of the vector potential and one for the scalar potential, taking the generic form

$$\left[ \nabla^2 + \frac{\omega^2}{c^2} \varepsilon \right] f(\mathbf{r}) = -g(\mathbf{r}). \quad (2.27)$$

The scalar Green's function  $G_0(\mathbf{r}, \mathbf{r}')$  is the solution of the equation above under a delta function perturbation, i.e.  $g(\mathbf{r}) = \delta(\mathbf{r} - \mathbf{r}')$ ,

$$G_0(\mathbf{r}, \mathbf{r}') = \frac{e^{\pm ik|\mathbf{r}-\mathbf{r}'|}}{4\pi|\mathbf{r}-\mathbf{r}'|} \quad (2.28)$$

where  $k^2 = \omega^2 \varepsilon / c^2$ . The Greens function then returns the vector potential as,

$$\mathbf{A}(\mathbf{r}) = \mu_0 \mu \int_V d\mathbf{r}' G_0(\mathbf{r}, \mathbf{r}') \mathbf{j}_0(\mathbf{r}'). \quad (2.29)$$

The electric field is easily expressed in terms of the vector potential by inserting the Lorentz gauge condition into Eq. (2.25) resulting in

$$\mathbf{E}(\mathbf{r}) = i\omega \left[ 1 + \frac{c^2}{\omega^2 \varepsilon} \nabla \nabla \cdot \right] \mathbf{A}(\mathbf{r}), \quad (2.30)$$

which can be expressed in terms of the external current sources using the scalar Green's function

$$\mathbf{E}(\mathbf{r}) = i\omega \mu_0 \mu \int_V d\mathbf{r}' \left[ 1 + \frac{c^2}{\omega^2 \varepsilon} \nabla \nabla \cdot \right] G_0(\mathbf{r}, \mathbf{r}') \mathbf{j}_0(\mathbf{r}'). \quad (2.31)$$

This allows the definition of the Dyadic Green's function that relates the electric field to the external current sources,

$$\overleftrightarrow{\mathbf{G}}(\mathbf{r}, \mathbf{r}', \omega) = \left[ 1 + \frac{c^2}{\omega^2 \varepsilon} \nabla \nabla \cdot \right] G_0(\mathbf{r}, \mathbf{r}') \quad (2.32)$$

such that

$$\mathbf{E}(\mathbf{r}) = i\omega \mu_0 \mu \int_V d\mathbf{r}' \overleftrightarrow{\mathbf{G}}(\mathbf{r}, \mathbf{r}', \omega) \mathbf{j}_0(\mathbf{r}'). \quad (2.33)$$

This expression will be used in the discussion of spontaneous emission of quantum emitters, and in the specific case of spontaneous emission near planar interfaces.

## 2.4.2 Two-level quantum emitters

In this section we derive the Purcell factor, i.e., the ratio of the actual spontaneous emission rate of a quantum emitter in the presence of other materials ( $\Gamma$ ) compared

to vacuum ( $\Gamma_0$ ), using a fully classical description. The subsequent section then gives a fully quantum mechanical description which shows exact agreement with the classical treatment as long as the quantum emitter is only weakly coupled with its environment.

Classically, the quantum emitter can be modelled as a radiating point dipole corresponding to the current distribution

$$\mathbf{J}(\mathbf{r}) = \delta(\mathbf{r} - \mathbf{r}_0) \partial_t \mathbf{p}. \quad (2.34)$$

By Poynting's theorem, the radiated power is given by the dissipated energy

$$P = \frac{dW}{dt} = -\frac{1}{2} \int d\mathbf{r} \operatorname{Re}(\mathbf{J}(\mathbf{r}) \cdot \mathbf{E}(\mathbf{r})), \quad (2.35)$$

which for the case of a radiating point dipole in vacuum yields[8]

$$P_0 = \frac{dW}{dt} = \frac{|\mathbf{p}|^2 \omega^4}{12\pi\epsilon_0\epsilon c^3}. \quad (2.36)$$

The Purcell effect can be demonstrated if the total electric field is written as the sum of the emitted dipole field  $\mathbf{E}_0$  and the scattered field  $\mathbf{E}_s$  of the medium

$$\mathbf{E}(\mathbf{r}) = \mathbf{E}_{\text{dipole}}(\mathbf{r}) + \mathbf{E}_s(\mathbf{r}). \quad (2.37)$$

Inserting this into Eq. (2.35) and calculating the ratio of the emission rate in the presence of an inhomogeneous medium to the free space emission rate returns the so-called Purcell factor

$$\frac{P}{P_0} = 1 + \frac{6\pi c^3 \epsilon_0 \epsilon}{|\mathbf{p}|^2 \omega^3} \operatorname{Im}[\mathbf{p} \cdot \mathbf{E}_s(\mathbf{r}_0)] \quad (2.38)$$

from which the importance of the scattering field strength on the emitted power is clear. In general we can write the energy emission rate of a point dipole in terms of the total Green's function Eq. (2.33)

$$P = \frac{dW}{dt} = \frac{\omega^3}{2c^2 \epsilon_0 \epsilon} \mathbf{p} \cdot \operatorname{Im} \left( \overleftrightarrow{\mathbf{G}}(\mathbf{r}_0, \mathbf{r}_0, \omega) \right) \cdot \mathbf{p} \quad (2.39)$$

which will be used when drawing the connection to the quantum mechanical treatment.

### 2.4.3 Spontaneous emission and the photonic density of states

A simple description of a quantum emitter can be made by considering it as a two-level system  $H_0$  with a ground state  $|g\rangle$  with eigen-energy  $E_g$  and excited state  $|e\rangle$

with eigen-energy  $E_e$ . The dynamics of this system is described by the Hamiltonian of a charged particle in the presence of an electromagnetic field

$$\hat{H} = \frac{1}{2m} (\hat{p} - q\mathbf{A})^2 + q\phi \quad (2.40)$$

$$= \hat{H}_0 - \frac{q}{2m} \mathbf{A} \cdot \hat{p} + \hat{p} \cdot \mathbf{A} + \frac{q^2}{2m} |\mathbf{A}|^2 \quad (2.41)$$

where  $q$  is the electron charge,  $\hat{H}_0 = \frac{\hat{p}^2}{2m} + q\phi$  and  $\hat{p} = -i\hbar\nabla$  is the momentum operator. If the vector field is assumed to vary slowly over the quantum emitter then  $\hat{p} \cdot \mathbf{A} = \mathbf{A} \cdot \hat{p}$  and to be weak such that the  $|A|^2$  term can be neglected then we can consider the perturbing Hamiltonian to be

$$\hat{H}' = -i \frac{q}{2m\omega} \mathbf{E} \cdot \hat{p} \quad (2.42)$$

where  $\mathbf{E} = i\omega\mathbf{A}$ . The electric field is quantized by introducing the electric field operator

$$\hat{\mathbf{E}} = \sum_{\mathbf{k}} \left[ \mathbf{E}_{\mathbf{k}}^*(\mathbf{r}) \hat{a}_{\mathbf{k}}(t) + \mathbf{E}_{\mathbf{k}}(\mathbf{r}) \hat{a}_{\mathbf{k}}^\dagger(t) \right] \quad (2.43)$$

where  $\hat{a}_{\mathbf{k}}(t) = \hat{a}_{\mathbf{k}} e^{i\omega_{\mathbf{k}}t}$  and  $\hat{a}_{\mathbf{k}}^\dagger(t) = \hat{a}_{\mathbf{k}}^\dagger e^{-i\omega_{\mathbf{k}}t}$  with  $\hat{a}_{\mathbf{k}}, \hat{a}_{\mathbf{k}}^\dagger$  being creation and annihilation operators for photons in mode  $\mathbf{k}$  and the frequency of each mode is given by  $\omega_{\mathbf{k}}$ .  $\mathbf{E}_{\mathbf{k}}^*(\mathbf{r})$  and  $\mathbf{E}_{\mathbf{k}}(\mathbf{r})$  are complex field amplitudes for positive and negative frequencies.

Assuming that the system is in the initial state of an excited quantum emitter and zero photons in the electromagnetic field, i.e.,  $|e, 0\rangle$ , Fermi's golden rule[66] then gives the decay rate of the two level system as a sum over all final states fulfilling energy conservation

$$\Gamma = \frac{2\pi}{\hbar^2} \sum_{|f\rangle} |\langle e|\hat{H}'|f\rangle|^2 \delta(\omega_0 - \omega_f) \quad (2.44)$$

$$= \sum_{\mathbf{k}} (\mathbf{p}_{eg}^* \cdot (\mathbf{E}_{\mathbf{k}}^*(\mathbf{r}) \mathbf{E}_{\mathbf{k}}(\mathbf{r})) \cdot \mathbf{p}_{eg}) \delta(\omega_{\mathbf{k}} - \omega_0). \quad (2.45)$$

where  $\omega_0 = E_e - E_g$  and  $\mathbf{p}_{eg} = \langle e|\mathbf{r}|g\rangle$  is known as the transition dipole matrix element. In the derivation we have used the fact that  $\hat{p} = \frac{i}{m} [\mathbf{r}, \hat{H}_0]$ . To introduce the concept of the PDOS it is common to introduce the normalized modes

$$E_{\mathbf{k}} = \sqrt{\frac{\hbar\omega_{\mathbf{k}}}{2\varepsilon_0}} \mathbf{u}_{\mathbf{k}}, \quad E_{\mathbf{k}}^* = \sqrt{\frac{\hbar\omega_{\mathbf{k}}}{2\varepsilon_0}} \mathbf{u}_{\mathbf{k}}^*. \quad (2.46)$$

The decay rate can then be written as,

$$\Gamma = \frac{\pi\omega}{3\hbar\varepsilon_0} |\mathbf{p}_{eg}|^2 \rho_p(\mathbf{r}_0, \omega_0) \quad (2.47)$$

$$\rho_p(\mathbf{r}_0, \omega_0) = 3 \sum_{\mathbf{k}} (\mathbf{n}_{eg}^* \cdot (\mathbf{u}_{\mathbf{k}}^*(\mathbf{r}_0) \mathbf{u}_{\mathbf{k}}(\mathbf{r}_0)) \cdot \mathbf{n}_{eg}) \delta(\omega_0 - \omega_{\mathbf{k}}). \quad (2.48)$$

where  $\rho_p(\mathbf{r}_0, \omega_0)$  is the photonic density of states at the location of the quantum emitter  $\mathbf{r}_0$  projected onto the axis of the dipole of the quantum emitter,  $\mathbf{n}_{eg}$ . This expression clearly shows the effect of increasing the photonic density of states on the decay rate.

The connection to the classical expression for the Purcell factor is then achieved by showing that Eq. (2.48) is actually the spectral representation of the Dyadic Greens function

$$\text{Im } \overleftrightarrow{\mathbf{G}}(\mathbf{r}, \mathbf{r}', \omega) = \frac{\pi c^2}{2\omega} \sum_{\mathbf{k}} \mathbf{u}_{\mathbf{k}}^*(\mathbf{r}, \omega_{\mathbf{k}}) \mathbf{u}_{\mathbf{k}}(\mathbf{r}', \omega_{\mathbf{k}}) \delta(\omega_{\mathbf{k}} - \omega), \quad (2.49)$$

which won't be proven here[8]. Comparison with Eq. (2.48) then shows that

$$\rho_p(\mathbf{r}_0, \omega_0) = \frac{6\omega_0}{\pi c^2} (\mathbf{n}_{eg}^* \cdot \text{Im } \overleftrightarrow{\mathbf{G}}(\mathbf{r}_0, \mathbf{r}_0, \omega_0) \cdot \mathbf{n}_{eg}) \quad (2.50)$$

which gives the decay rate

$$\Gamma = \frac{2\omega^2}{\hbar \varepsilon_0 c^2} (\mathbf{p}_{eg}^* \cdot \text{Im } \overleftrightarrow{\mathbf{G}}(\mathbf{r}_0, \mathbf{r}_0, \omega_0) \cdot \mathbf{p}_{eg}). \quad (2.51)$$

In the case of free space it is possible to show that  $\rho_p$  is independent of the orientation of the dipole moment which becomes  $\rho_0 = \omega_0^2 / \pi^2 c^3$  resulting a free space decay rate of

$$\Gamma_0 = \frac{\omega_0^3 |\mathbf{p}_{eg}|^2}{3\pi \varepsilon_0 \hbar c^3}. \quad (2.52)$$

This makes it straightforward to confirm that the predicted Purcell factor is identical to the classical treatment, i.e.,

$$\frac{\Gamma}{\Gamma_0} = \frac{P}{P_0}. \quad (2.53)$$

## 2.4.4 Emission near planar media

To determine the effect of a planar substrate on the decay rate of a quantum emitter Eq. (2.38) shows that we need calculate the scattered field of the substrate at the location of the quantum emitter. Making use of the Dyadic Green's function formalism it is possible to express the scattered field in terms of the Dyadic Green's function. We consider the free space Dyadic Green's function for the specific case of a radiating dipole at a position  $\mathbf{r}_0 = (x_0, y_0, z_0)$ ,  $\mathbf{j} = -i\omega \mathbf{p} \delta(\mathbf{r} - \mathbf{r}_0)$ , in a medium characterized by the dielectric function  $\varepsilon_1$ . The resulting electric field is then given by Eq. (2.33)

$$\mathbf{E}_0(\mathbf{r}) = \omega^2 \mu_0 \mu \overleftrightarrow{\mathbf{G}}_0(\mathbf{r}, \mathbf{r}_0) \mathbf{p}. \quad (2.54)$$

The dipole is placed above a planar substrate with interface in the  $xy$ -plane at  $z = 0$ . The so-called angular spectrum representation is a convenient representation that makes it easy to implement the boundary conditions of Maxwell's equations by expressing the Dyadic Green's function in terms of propagating and evanescent plane waves. It is equivalent to a two-dimensional Fourier transform in the in-plane coordinates  $x, y$ , the out-of-plane dependence is then given as  $e^{ik_z z}$  where  $k_z = \pm(k_1^2 - k_x^2 - k_y^2)^{1/2}$  (with the sign determined by the condition that  $\text{Im}(k_z) > 0$ ) where  $k_1^2 = \varepsilon_1 \omega^2 / c^2$ . The free space Dyadic Green's function then takes the angular spectrum form[8]

$$\overleftrightarrow{\mathbf{G}}_0 = \frac{i}{8\pi^2} \int_{-\infty}^{\infty} \int_{-\infty}^{\infty} dk_x dk_y \overleftrightarrow{\mathbf{M}} e^{i[k_x(x-x_0) + k_y(y-y_0) + k_z|z-z_0|]} \quad (2.55)$$

$$\overleftrightarrow{\mathbf{M}} = \frac{1}{k_1^2 k_{z_1}} \begin{bmatrix} k_1^2 - k_x^2 & -k_x k_y & \mp k_x k_{z_1} \\ -k_x k_y & k_1^2 - k_y^2 & \mp k_y k_{z_1} \\ \mp k_x k_{z_1} & \mp k_y k_{z_1} & k_1^2 - k_z^2 \end{bmatrix}. \quad (2.56)$$

The upper sign applies when  $z > z_0$  and the lower sign when  $z < z_0$ . The expansion in terms of evanescent waves is clear: when  $k_x^2 + k_y^2 > \omega^2 \varepsilon_1 / c^2$ ,  $k_z$  becomes imaginary and the electric field decays exponentially as the distance to the dipole is increased. The total electric field is the sum of the emitted dipole field and the reflected field  $\mathbf{E} = \mathbf{E}_0 + \mathbf{E}_{\text{ref}}$  and likewise it is possible to split the total Dyadic Green's function into a dipole and reflected contributions,

$$\overleftrightarrow{\mathbf{G}} = \overleftrightarrow{\mathbf{G}}_0 + \overleftrightarrow{\mathbf{G}}_{\text{ref}}. \quad (2.57)$$

If the incident field  $\mathbf{E}_0$  was a plane-wave then the reflected field would be trivially given in terms of Fresnel's reflection and transmission coefficients as  $\mathbf{E} = \mathbf{E}_0 + r_{s,p} \mathbf{E}_0$  where  $r_s$  ( $r_p$ ) is the Fresnel reflection coefficient for s-polarized (p-polarized) light[8]. The reflected Dyadic Green's function is simply the free space Green's function where each Fourier component has been multiplied by Fresnel's reflection coefficients. Taking into account different polarizations the reflected Dyadic Green's function is split into  $p$  and  $s$ -polarized contributions and which results in[8]

$$\overleftrightarrow{\mathbf{G}}_{\text{ref}} = \frac{i}{8\pi^2} \int_{-\infty}^{\infty} \int_{-\infty}^{\infty} dk_x dk_y \left[ \overleftrightarrow{\mathbf{M}}_{\text{ref}}^s + \overleftrightarrow{\mathbf{M}}_{\text{ref}}^p \right] e^{i[k_x(x-x_0) + k_y(y-y_0) + k_z(z+z_0)]} \quad (2.58)$$

where

$$\overleftrightarrow{\mathbf{M}}_{\text{ref}}^s = \frac{r^s(k_x, k_y)}{(k_x^2 + k_y^2)k_{z_1}} \begin{bmatrix} k_y^2 & -k_x k_y & 0 \\ -k_x k_y & k_x^2 & 0 \\ 0 & 0 & 0 \end{bmatrix} \quad (2.59)$$

$$\overleftrightarrow{\mathbf{M}}_{\text{ref}}^p = \frac{-r^p(k_x, k_y)}{k_1^2(k_x^2 + k_y^2)} \begin{bmatrix} k_x^2 k_{z_1} & k_x k_y k_{z_1} & k_x(k_x^2 + k_y^2) \\ k_x k_y k_{z_1} & k_y^2 k_{z_1} & k_y(k_x^2 + k_y^2) \\ -k_x(k_x^2 + k_y^2) & -k_y(k_x^2 + k_y^2) & -(k_x^2 + k_y^2)^2 / k_{z_1} \end{bmatrix}. \quad (2.60)$$

If the substrate is a layered material, such as the materials investigated in this thesis, then the rotational symmetry reduces the complexity of the problem to a simple calculation of the integral[8]

$$\frac{P}{P_0} = 1 + \frac{p_{\parallel}^2}{|\mathbf{p}|^2} \frac{3}{4} \int_0^{\infty} ds \operatorname{Re} \left\{ \frac{s}{s_z} [r^s - s_z^2 r^p] e^{ik_1 z_0 s z} \right\} + \frac{p_{\perp}^2}{|\mathbf{p}|^2} \frac{3}{2} \int_0^{\infty} ds \operatorname{Re} \left\{ \frac{s^3}{s_z} r^p e^{ik_1 z_0 s z} \right\}, \quad (2.61)$$

where  $s = \frac{k_{\rho}}{k_1}$ ,  $s_z = \sqrt{1 - s^2}$  and  $p_{\parallel}$ ,  $p_{\perp}$  are the in-plane and out-of-plane projections of the dipole moment.

## 2.5 Hyperbolic metamaterials

A metamaterial is an artificial material that has been structured on a subwavelength scale such as to obtain an unusual response to external radiation[67]. By creating an artificial material with engineered "meta-atoms" it is possible to engineer a response to optical fields unlike any naturally occurring material[13]. If the meta-atoms are small compared to the optical field within the material, then the response of the metamaterial can be understood in terms of effective/average permittivities and permeabilities[14]. In conventional optical metamaterials, the goal is to obtain both

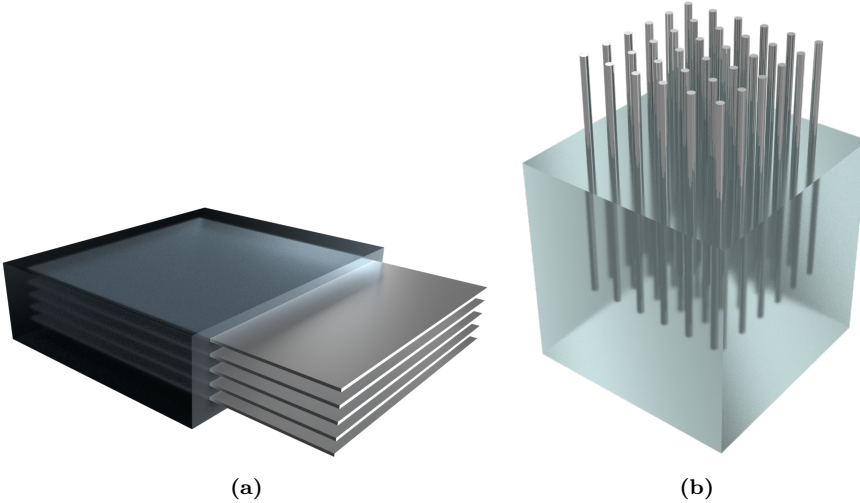


**Figure 2.8:** Examples of (a) a planar layered hyperbolic metamaterial and (b) a metal nanowire hyperbolic metamaterial.

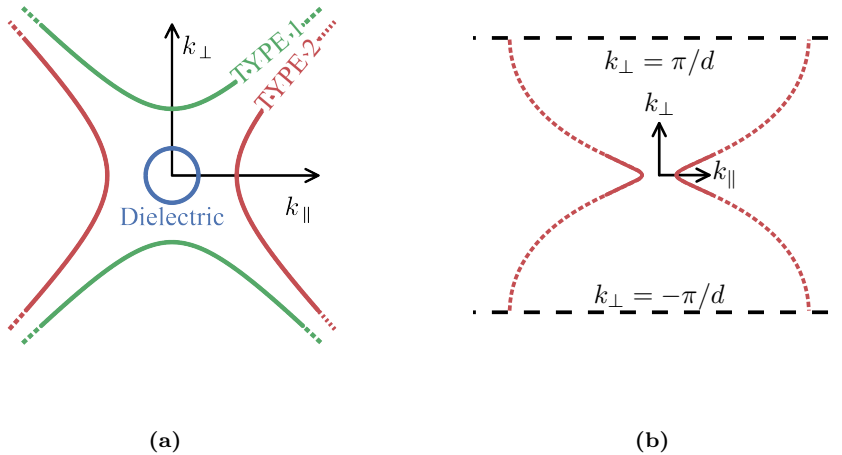


**Figure 2.9:** (a) Hyperbolic isofrequency surfaces showing the difference between type 1 and 2 hyperbolicity, compared to an isotropic dielectric isofrequency surface (blue). (b) When the wavelength of the fields within the material approaches the period of the structure the EMT picture breaks down and the isofrequency surfaces deviate from the hyperbolic approximation (dashed lines).

negative effective permeability and permittivity which results in a negative refractive index[17],  $n < 0$ , entailing a number of interesting applications such as perfect lensing. Unfortunately, achieving optical negative index materials have been challenged by limitations of engineering a strong magnetic response[55].

In this thesis we have investigated a different class of metamaterials, known as hyperbolic metamaterials[4] (HMM), that do not require a negative permeability. They are characterized by an extreme anisotropy in their dielectric response, resulting in a sign difference of the diagonal components of the dielectric tensor. In HMMs such an anisotropy is typically obtained by restricting the charge carrier movement in some directions. In a planar layered heterostructure HMM consisting of alternating metal and dielectric layers (Fig. 2.8(a)) movement is restricted to the in-plane direction resulting in an in-plane metallic response ( $\epsilon_{\parallel}^{\text{eff}} < 0$ ) and an out-of-plane dielectric response ( $\epsilon_{\perp}^{\text{eff}} > 0$ ). Another example of a HMM is the metal nanowire medium in which the electron motion is restricted in two directions (Fig. 2.8(b)). Effective permittivities for the planar layered HMM are derived from the boundary conditions of Maxwell's equations, i.e., continuity of the parallel component of the electric field and

the normal component of the displacement field, resulting in

$$\varepsilon_{\parallel}^{\text{eff}} = f\varepsilon_a + (1 - f)\varepsilon_b, \quad (2.62)$$

$$\frac{1}{\varepsilon_{\perp}^{\text{eff}}} = \frac{f}{\varepsilon_a} + \frac{1 - f}{\varepsilon_b} \quad (2.63)$$

where  $f$  is the fill fraction of component  $a$  with dielectric function  $\varepsilon_a$  and component  $b$  has dielectric function  $\varepsilon_b$ . The sign difference of their dielectric tensor results in hyperbolic iso-frequency surfaces given by Eq. (2.13) shown in Figure 2.9(a), in contrast to the elliptical or spherical iso-frequency surfaces found in most dielectrics. Depending on the number of negative components in the dielectric tensor, two types of hyperbolic behaviour can be observed. Type 1 (one negative component, green curve) support hyperbolic modes for all in-plane wave vectors in contrast to type 2 (two negative components, red curve) which only support wave vectors above an in-plane cut-off wave vector. For low-frequencies, the planar layered metamaterial exhibit type 2 behaviour, while the metallic nanowire medium shows type 1 behaviour[19].

Hyperbolic metamaterials have become the subject of intensive research because of the potential benefits they provide, most of which can be understood in terms of their hyperbolic isofrequency surfaces. For this thesis the most relevant of these benefits is the enhancement of the spontaneous emission rate in the vicinity of hyperbolic metamaterials[68, 69] caused by the large area of the isofrequency surfaces of a HMM entailing large photonic density of states (Eq. (2.48)), determined by Eq. (2.61). Enhanced Purcell factors have been measured in planar layered metamaterials consisting of silver and titanium-oxide ( $\text{TiO}_2$ ) in the order of 10[70]. Of other properties and applications of HMMs we mention the possibility of achieving hyperlensing[71, 72] in slabs of hyperbolic metamaterials.

### 2.5.1 Limitations of hyperbolic metamaterials

Effective medium theory (EMT), Eqs. (2.62, 2.63), predict a practically unlimited purcell factor limited only by the distance of the dipole to hyperbolic substrate, i.e., limited by the exponential factor in Eq. (2.48). This is an illness of the EMT description and in reality infinitely large wave-vectors are not supported by a hyperbolic metamaterial substrate. When the wavelength within the hyperbolic metamaterial approaches the period of the metamaterial, the artificial structuring is no longer sub-wavelength and effective medium theory breaks down. The implications of the finite subwavelength structuring can be recognized by solving Maxwell's equations in the case of a true, infinite multilayer structure. Using the transfer matrix method Kidwai, Zhukovsky, and Sipe [46] showed that the introduction of a finite period introduced a cutoff for the hyperbolic modes thus limiting the photonic density of states. Using Bloch's theorem, the dispersion of hyperbolic modes in a planar hyperbolic metama-

terial is determined by the solutions of

$$\cos(k_B(d_d + d_m)) = \cos(k_{m,\perp}d_m) \cos(k_{d,\perp}d_d) + \quad (2.64)$$

$$\left( \frac{\varepsilon_m k_{d,\perp}}{\varepsilon_d k_{m,\perp}} + \frac{\varepsilon_d k_{m,\perp}}{\varepsilon_m k_{d,\perp}} \right) \sin(k_{m,\perp}d_m) \sin(k_{d,\perp}d_d) \quad (2.65)$$

where  $d_d$  and  $d_m$  are the dielectric and metal layer thicknesses, respectively,  $k_{(d,m),\perp} = \sqrt{k_0^2 \varepsilon_{(d,m)} - k_{\parallel}^2}$  are the out-of-plane wave numbers and  $k_b$  is the out-of-plane Bloch wavenumber representing propagation through the heterostructure. The associated iso-frequency surface is shown in Figure 2.8(b) where the deviation from the hyperbolic dispersion is clear for large wave-vectors (dashed).

The hyperbolic response is on a fundamental level a result of the hybridizing SPPs that each interface in the HMM support[73, 74]. A HMM is therefore actually a plasmonic device and thus subject to the same limitations[3], namely, large losses. It can be argued that these limitations are even more severe for HMMs since very thin films are needed to achieve large photonic density of states which make surface roughness a considerable source of losses[75, 76].

Even if the heterostructure period is subwavelength quantum mechanical effects can lead to the breakdown of the effective hyperbolic response[77]. A consequence of quantum mechanics is that the dielectric function becomes non-local, i.e., the polarization at one point in space  $\mathbf{P}(\mathbf{r})$  is dependent on the electric field in another point  $\mathbf{E}(\mathbf{r}')$ . Mathematically, this translates to a spatial dependence of the dielectric function

$$\varepsilon = \varepsilon(\mathbf{r}, \mathbf{r}'). \quad (2.66)$$

In the Drude description of the metallic response the discrete atomic nature of the metal is neglected and in this picture the non-local response only depends on the relative distance of  $\mathbf{r}$  and  $\mathbf{r}'$ ,  $|\mathbf{r} - \mathbf{r}'|$ , that is  $\varepsilon(|\mathbf{r} - \mathbf{r}'|)$  which in reciprocal space is expressed as  $\varepsilon(\mathbf{k})$  where  $\mathbf{k}$  is the wave-vector of the electric field within the material. A more rigorous treatment of the dynamics of the electronic system within the Thomas-Fermi approximation leads to [78]

$$\varepsilon(\omega, \mathbf{k}) = 1 - \frac{1}{\omega(\omega + i\eta) - \beta^2 |\mathbf{k}|^2} \quad (2.67)$$

where  $\beta^2 = \frac{3}{5} v_F^2$  with  $v_F$  being the Fermi velocity[79]. Since  $\varepsilon \rightarrow 1$  when  $|\mathbf{k}| \rightarrow \infty$  the metallic (and thus the hyperbolic) response is limited to small wave vectors and the achievable PDOS no longer diverges[77].

In addition to the spontaneous emission enhancement achieved by emission into propagating hyperbolic modes or SPPs, other competing decay mechanisms exists. The decay of a quantum emitter under the excitement of electron-hole pairs is known as quenching and can be a significant contribution to the Purcell Factor as the results of this thesis will show. Quenching has been rigorously treated previously[80–82] from

which it is known that the effect decays as  $d^{-3}$ , where  $d$  is the distance to the substrate, just like the spontaneous emission enhancement due to hyperbolic modes[68]. Since both the electron-hole pair and the quantum emitter can be thought of as dipoles with near-fields decaying as  $d^{-3}$ , the distance dependence extracted from Fermi's golden might be expected to be  $\propto d^{-6}$ , making the  $d^{-3}$ -dependence surprising. The  $d^{-3}$ -dependence comes about when summing up all excited electron-hole pairs within the substrate which cancels the distance dependence of the substrate[83].

# CHAPTER 3

## Density Functional Theory Background

---

This chapter describes the theoretical framework used in this thesis for calculating properties of matter. Since the development of quantum mechanics for describing physical events on the atomic length scale we have known the mathematical equations that describe most properties of matter. However, even with the necessary theoretical framework, the problem of calculating properties of matter remain a challenging task. The challenges of calculating properties of matter are technical rather than principal, i.e., it is the complexity of the equations and the difficulties in solving them that has inhibited the progress of the field for many decades. Therefore, the most important discoveries within the field are those that have been able reduce the computational complexity of the problems without introducing significant errors.

### 3.1 The problem of the structure of matter

On the microscopic level all matter consists of atoms. The enormous diversity in kind and properties of materials we find in nature emerge from the specific atomic composition that constitute every single material. Gasses consist of freely floating atoms or molecules, liquids are more dense and solids consists of fixed configurations of atoms. Even for a single element of the periodic table it is possible to create materials of many different properties, which the many allotropes of carbon testifies to (Diamond, graphite, carbon-nanotubes, fullerenes etc.[84]). A theory that can predict the properties which emerge from the structuring of matter in different forms must therefore depend not only on the type of atoms investigated but also on their specific spatial configuration.

Since the development of quantum mechanics it has in principle been possible to calculate material properties from theory[85]. In quantum mechanics, a material is described by its wavefunction  $\Psi(\mathbf{r}_1, \mathbf{r}_2, \dots, \mathbf{R}_1, \mathbf{R}_2, \dots, t)$  where  $\mathbf{r}_*$  and  $\mathbf{R}_*$  are electronic and nuclear coordinates, respectively. The wavefunction represents the statistical probability of an electron (or nuclei) to occupy a certain position in space, in contrast to classical mechanics where electrons and nuclei are treated as point particles. The

time-dependent Schrödinger equation describes the evolution of the wave-function

$$-i\partial_t\Psi(\{\mathbf{r}\},\{\mathbf{R}\},t) = \hat{H}\Psi(\{\mathbf{r}\},\{\mathbf{R}\},t) \quad (3.1)$$

where  $\{\mathbf{r}\}$  and  $\{\mathbf{R}\}$  denote the set of all electronic and nucleic coordinates, respectively, and  $\hat{H}$  is the Hamiltonian operator of the system. The Hamiltonian is given by

$$\begin{aligned} \hat{H} = & -\sum_{\{\mathbf{r}\}} \frac{\hbar^2}{2m} \nabla_{\mathbf{r}}^2 - \sum_{\{\mathbf{R}\}} \frac{\hbar^2}{2M} \nabla_{\mathbf{R}}^2 + \frac{1}{2} \sum_{\mathbf{r}_i \in \{\mathbf{r}\}, \mathbf{r}_j \in \{\mathbf{r}\}, \mathbf{r}_i \neq \mathbf{r}_j} \frac{e^2}{|\mathbf{r}_i - \mathbf{r}_j|} + \\ & \frac{1}{2} \sum_{\mathbf{R}_i \in \{\mathbf{R}\}, \mathbf{R}_j \in \{\mathbf{R}\}, \mathbf{R}_i \neq \mathbf{R}_j} \frac{Z_i Z_j}{|\mathbf{R}_i - \mathbf{R}_j|} + \sum_{\mathbf{r}_i \in \{\mathbf{r}\}, \mathbf{R}_j \in \{\mathbf{R}\}} \frac{e Z_j}{|\mathbf{r}_i - \mathbf{R}_j|}, \end{aligned} \quad (3.2)$$

where  $Z$  is the charge of the nuclei,  $m$  is the electron mass and  $M$  is the proton mass. The first and second term describes the kinetic energy of the electrons and the nuclei, respectively, and the latter terms describe their Coulomb (electrostatic) repulsion. Because the wave-function contain all information about the material and all properties can be derived from its knowledge, it might be surprising that this is still an active field of science. The reason is the monstrosity that is the wave-function. For example, to store a wave-function for a system consisting of 4 electrons requires, if every coordinate is represented on a three dimensional grid of  $10 \times 10 \times 10 = 1000$  grid-points, storing  $1000^4$  numbers or an equivalent of more than 14 terabytes of data. Simply adding one electron to this fictitious material results in a memory demand of more than 14 petabytes. The exponential increase in the computational demands is the essential problem that inhibits progress in the field of computational materials design and a significant part of research is dedicated to finding new methods and simplifications that can reduce the strain on computing facilities.

The first simplification to make is to separate the dynamics of the electrons and the nuclei's. The large mass of nuclei's compared to electrons ( $m_e/m_p = 10^{-4}$ ) make this separation of variables a good approximation in most cases and is known as the Born-Oppenheimer approximation[86]. Mathematically, the approximation is equivalent of the product ansatz for the full wave-function[87]

$$\Psi(\{\mathbf{r}\},\{\mathbf{R}\},t) = \Theta(\{\mathbf{R}\},t)\Phi(\{\mathbf{r}\};\{\mathbf{R}\}), \quad (3.3)$$

where  $\Phi$  is the solution of  $\hat{H}_e\Phi(\{\mathbf{r}\};\{\mathbf{R}\}) = E(\{\mathbf{R}\})\Phi(\{\mathbf{r}\};\{\mathbf{R}\})$ .  $\hat{H}_{ee}$  is the electronic Hamiltonian defined by

$$\hat{H}_e = \hat{T} + \hat{U}_{ee} + \hat{V}_{ne} \quad (3.4)$$

where  $\hat{T}$  is the kinetic energy,  $\hat{U}_{ee}$  is the electron-electron interaction and  $\hat{V}_{ne}$  is the

electrostatic potential from the nuclei given by

$$\hat{T} = - \sum_{\{\mathbf{r}\}} \frac{\hbar^2}{2m} \nabla_{\mathbf{r}}^2 \quad (3.5)$$

$$\hat{U}_{ee} = \frac{1}{2} \sum_{\mathbf{r}_i \in \{\mathbf{r}\}, \mathbf{r}_j \in \{\mathbf{r}\}, \mathbf{r}_i \neq \mathbf{r}_j} \frac{e^2}{|\mathbf{r}_i - \mathbf{r}_j|} \quad (3.6)$$

$$\hat{V}_{ne} = \sum_{\mathbf{r}_i \in \{\mathbf{r}\}, \mathbf{R}_j \in \{\mathbf{R}\}} \frac{eZ_j}{|\mathbf{r}_i - \mathbf{R}_j|}. \quad (3.7)$$

For a dynamic system of moving atoms, the Born-Oppenheimer approximation can be understood by imagining the electrons as instantaneously adjusting to the potential landscape created by the nuclei. From this point we restrict ourselves to the electronic subsystem and disregard the nucleic subsystem. The subscript for the electronic subsystem is neglected as no confusion should be possible.

## 3.2 Density Functional Theory

The exponential increase in computational costs with system size was seen to be the main limiting factor in treating systems of little more than 4 particles. Partly because it has broken this scaling, density functional theory[87, 88] (DFT) has been one of the most successful advances of theoretical materials science throughout history. The scaling is broken by taking advantage of the fact that the complex electronic structure problem can be reduced significantly by employing the electronic density as relevant parameter, as opposed to the many-body wave-function. At the basis of DFT lies the fundamental theorems of Hohenberg and Kohn[89] which will be summarized in the following.

In DFT jargon the potential originating from the static nuclei's is known as the 'external' potential, and the Hamiltonian is written as the sum of the kinetic energy, the electron-electron interaction and the external potential.

$$\hat{H} = \hat{T} + \hat{U}_{ee} + \hat{V}_{\text{ext}}. \quad (3.8)$$

**First Hohenberg-Kohn Theorem.** *The external potential is uniquely determined by the electronic density.*

The total energy is trivially a functional of the external potential. The first Hohenberg-Kohn theorem then proves that the total energy of a system is also a functional of the electronic density by establishing a one-to-one relationship between the electronic density and the external potential. Because the many-body wave-function is determined by the external potential the first Hohenberg-Kohn theorem also establishes its relationship to the electronic density as a functional of it, that is,  $\Phi = \Phi[\hat{V}_{\text{ext}}[\rho]]$ .

**Second Hohenberg-Kohn Theorem.** *The ground state energy can be obtained variationally; the density that minimizes the total energy is the ground state density. The variational energy is given by,*

$$E_v[\rho] = F[\rho] + \int \rho(\mathbf{r})v_{\text{ext}}(\mathbf{r})d^3r \quad (3.9)$$

with  $F[\rho] = \langle \Phi[\rho] | \hat{T} + \hat{U}_{\text{ee}} | \Phi[\rho] \rangle$ .

The second Hohenberg-Kohn theorem introduces an energy functional  $F[\rho]$  which describes the contributions to the total energy from the electron-electron interaction and the kinetic energy. The theorem gives a recipe for finding the ground state energy of a system; i.e., the one that minimizes the energy functional  $F$ . However, the calculation requires the knowledge of the unknown many-body electronic wavefunction. The Hohenberg-Kohn theorems give no practical scheme to overcome this problem but establishes the property of DFT as an, in principle, exact theory.

### 3.2.1 Kohn-Sham Theory

The calculation the kinetic energy  $\langle \Phi[\rho] | \hat{T} | \Phi[\rho] \rangle$  in principle requires the knowledge of how the kinetic energy operator acts on the many-particle wavefunction. Since the wave-function is unknown this is not a straight-forward operation. In Kohn-Sham theory[90] the system of interacting electrons is replaced by a system of non-interacting electrons embedded in an effective potential  $v_{\text{R}}$  constructed to reproduce the density of the interacting system. This is a significant simplification since it makes it possible to represent the contribution from the kinetic energy by simple single particle matrix elements. The model system is typically known as the *non-interacting reference system* and is described by the Hamiltonian

$$\hat{H}_{\text{R}} = \sum_{i=1}^N \left[ -\frac{\hbar^2}{2m} \nabla_i^2 + v_{\text{R}}(\mathbf{r}_i) \right]. \quad (3.10)$$

Here  $N$  is the number of electrons and  $v_{\text{R}}$ , the potential of the reference system, is chosen such that the ground state density of  $\hat{H}_{\text{R}}$  reproduces the density of interacting system.

Because the reference system is non-interacting its ground state will be a Slater determinant and the corresponding density of the reference system is simply given by,  $\rho(\mathbf{r}) = 2 \sum_{i=1}^{N/2} |\phi_i(\mathbf{r})|^2$ , the kinetic energy becomes  $T_{\text{R}}[\rho] = \frac{\hbar^2}{m} \sum_{i=1}^{N/2} \langle \phi_i | \nabla^2 | \phi_i \rangle$ , and the total energy of the Kohn-Sham system reduces to

$$E_{\text{KS}}[\rho] = T_{\text{R}}[\rho] + \int \rho(\mathbf{r})v_{\text{ext}}(\mathbf{r})d^3r + E_{\text{Hartree}} + E_{\text{xc}}[\rho]. \quad (3.11)$$

Here, according to custom, the electrostatic energy contribution to the total energy  $E_{\text{Hartree}}$  (the Hartree energy) has been separated out from the electron-electron interaction and the so-called exchange-correlation (xc) energy  $E_{\text{xc}}$  has been introduced

to account for all left-over energy contributions. The xc-energy contain contributions to the total energy originating from the anti-symmetric nature of the many-particle wave-function (exchange) as well as contributions resulting from many-body correlation effects.

### 3.2.2 Exchange-correlation functionals

The most rudimentary approximation to the xc-energy is known as the Local Density Approximation (LDA). Here the energetic contributions to exchange and correlation is derived from the homogeneous electron gas and applied locally to each point in space. For optical properties the LDA approximation suffers from the fact that it underestimates electronic band-gaps by 40%[87, 91] leading to an overestimation of the dielectric constant in semiconductors on the order of 5-20%[92].

Generalized gradient approximations (GGAs) are semi-local xc-functionals that go beyond the LDA by employing information about the gradient of the density in every point of space. The band gap energies typically only improves marginally and thus the description of the dielectric constant is not significantly better described compared to LDA[87, 93].

The layered materials that have been investigated in this thesis are bonded through the long range van der Waals force. These forces originate from instantaneous dipole interactions at a long range and is a purely quantum mechanical effect. Due to the inherent non-local nature of van der Waals interactions, both the LDA and GGAs fail to describe bonding distances in the layered van der Waals systems treated in this work[94]. To accurately describe the bonding of our layered systems it is necessary to employ xc-functionals that explicitly take into account the non-local interactions and in this thesis we consider two of such functionals: the BEEF-vdW[94] and the optB88-vdW[95] functionals. These functionals are fitted to experimental data and their success or failure will be discussed in our application of the functionals.

As a general remark, we note that although the commonly used approximations to the exchange-correlation energy does not always give quantitative agreement with experiment, trends are often preserved and this important fact is often used to compare the performance of different compounds as predicted by DFT, as has also been done in this thesis[87].

## 3.3 Linear response theory for the dielectric function

As explained in Chapter 2, the calculation of the dielectric function is the primary goal of any theory that describes the linear optical response of matter. The microscopic dielectric function, describing microscopic variation of the polarization throughout the material, generally exhibits large fluctuations due to the discrete atomic nature of any material. However, in Maxwell's macroscopic equations (2.1-2.4) the deviations on the order of the atomic scale were substituted by the use of average macroscopic

fields and in this section we will briefly describe how to connect the microscopic and the macroscopic pictures.

The (longitudinal) microscopic dielectric function is defined as

$$\langle \varepsilon \rangle(\mathbf{r}, \mathbf{r}', \omega) = \frac{1}{\varepsilon_0} \frac{\delta \mathbf{D}(\mathbf{r})}{\delta \mathbf{E}(\mathbf{r}')} = \delta(\mathbf{r} - \mathbf{r}') + \frac{1}{\varepsilon_0} \frac{\delta \mathbf{P}(\mathbf{r})}{\delta \mathbf{E}(\mathbf{r}')}. \quad (3.12)$$

Here, non-locality is implied by the dependence of the dielectric function on both  $\mathbf{r}$  and  $\mathbf{r}'$ , i.e., an electric field at  $\mathbf{r}'$  can induce a polarization at another position  $\mathbf{r}$  (see Sec. 2.5.1). For longitudinal fields it is convenient to introduce the total potential  $-\nabla v_{\text{tot}} = \mathbf{E}$  and external potential  $-\varepsilon_0 \nabla v_{\text{ext}} = \mathbf{D}$  such that the inverse dielectric function becomes

$$\varepsilon^{-1}(\mathbf{r}, \mathbf{r}', t - t') = \frac{\delta v_{\text{tot}}(\mathbf{r}, t)}{\delta v_{\text{ext}}(\mathbf{r}', t')} = \delta(\mathbf{r} - \mathbf{r}') + \frac{\delta v_{\text{ind}}(\mathbf{r}, t)}{\delta v_{\text{ext}}(\mathbf{r}', t')}. \quad (3.13)$$

The inverse dielectric function represents a more intuitive quantity as it describes the response in the total potential to an external perturbation in contrast to the dielectric function. The induced potential has been introduced through  $v_{\text{tot}} = v_{\text{ext}} + v_{\text{ind}}$ .

In the Kubo formalism of linear response theory the induced potential is expanded to first order in the external potential, using the Kubo Formula[96]. Given a time-independent Hamiltonian  $\hat{H}_0$  subject to a perturbation  $\hat{H}'$  at times  $t > t_0$  the linear response of the mean value of an observable  $\hat{O}$  is given by the Kubo formula

$$\delta \langle \hat{O}(t) \rangle = \int_{t_0}^{\infty} \left( -i \theta(t - t') \langle [\hat{O}(t), \hat{H}'(t')] \rangle_0 \right). \quad (3.14)$$

Here  $\langle \hat{A} \rangle_0 = (Z_0)^{-1} \text{Tr}[\rho_0 \hat{A}]$  denotes equilibrium average of  $\hat{A}$  with respect to  $H_0$ ,  $\rho_0$  is the density operator,  $Z_0 = \text{Tr}[\rho_0 \hat{A}]$  is the density operator and  $[\cdot, \cdot]$  denotes the commutator. In this case the observable  $\hat{O}$  is the induced potential associated with the operator

$$\hat{v}_{\text{ind}}(\mathbf{r}, t) = \int d\mathbf{r}'' v_c(\mathbf{r} - \mathbf{r}'') \hat{n}(\mathbf{r}'', t) \quad (3.15)$$

where  $v_c(\mathbf{r}) = |\mathbf{r}|^{-1}$  is the Coulomb kernel and the perturbation is

$$\hat{H}' = \int d\mathbf{r}' \delta v_{\text{ext}}(\mathbf{r}', t') \hat{n}(\mathbf{r}'). \quad (3.16)$$

Using the Kubo formula to get the induced potential and Fourier transforming in time the dielectric function becomes

$$\varepsilon^{-1}(\mathbf{r}, \mathbf{r}', \omega) = \delta(|\mathbf{r} - \mathbf{r}'|) + \int v_c(|\mathbf{r} - \mathbf{r}''|) \chi(\mathbf{r}'', \mathbf{r}', \omega) d\mathbf{r}'''. \quad (3.17)$$

$\chi$  is known as the interacting density response function and is given by

$$\chi(\mathbf{r}, \mathbf{r}', \omega) = -i \lim_{\eta \rightarrow \infty} \int d(t - t') e^{i(\omega + i\eta)(t - t')} \theta(t - t') \langle [\hat{n}(\mathbf{r}, t), \hat{n}(\mathbf{r}', t')] \rangle, \quad (3.18)$$

where  $\hat{n}$  is the density operator and  $\eta$  is a small parameter introduced to ensure convergence of the Fourier transform. Within the random-phase approximation (RPA), the interacting density response function is approximated through the Dyson equation[97, 98]

$$\hat{\chi} = \hat{\chi}_0 + \hat{\chi}_0 \hat{v}_c \hat{\chi}, \quad (3.19)$$

where  $\hat{\chi}$  is to be understood as an operator in  $\mathbf{r}$  and  $\mathbf{r}'$  and  $\chi_0$  is known as the non-interacting density response function. In this approximation the dielectric function reduces to

$$\varepsilon(\mathbf{r}, \mathbf{r}', \omega) = \delta(|\mathbf{r} - \mathbf{r}'|) - \int v_c(|\mathbf{r} - \mathbf{r}''|) \chi_0(\mathbf{r}'', \mathbf{r}', \omega) d\mathbf{r}''. \quad (3.20)$$

For periodic systems like crystals it is more convenient to represent the dielectric function in terms of its Fourier transform

$$\varepsilon_{\mathbf{G}\mathbf{G}'}(\mathbf{q}, \omega) = \int_{V_{\text{cell}}} d\mathbf{r} \int_{V_{\text{cell}}} d\mathbf{r}' e^{-i(\mathbf{q}+\mathbf{G})\mathbf{r}} \varepsilon(\mathbf{r}, \mathbf{r}', \omega) e^{i(\mathbf{q}+\mathbf{G}')\mathbf{r}'}. \quad (3.21)$$

Here  $\mathbf{G}$  denotes a reciprocal lattice vector and  $\mathbf{q}$  the wave-vector of the external potential i.e.  $v_{\text{ext}} \propto e^{-i\mathbf{q}\cdot\mathbf{r}}$ . The connection to macroscopic electrodynamics is made by averaging the total potential resulting from an optical field ( $\propto e^{-i\mathbf{q}\cdot\mathbf{r}}$ ) over a single unit cell. In the reciprocal space representation this can be conveniently expressed as[97, 98]

$$\varepsilon_{\mathbf{M}}(\mathbf{q}, \omega) = \frac{1}{[\varepsilon_{\mathbf{G}\mathbf{G}'}^{-1}(\mathbf{q}, \omega)]_{00}}. \quad (3.22)$$

This formula provides the recipe for obtaining the macroscopic dielectric response from the microscopic dielectric function.

## 3.4 Optical properties from first principles

Starting from Eq. (3.18) the non-interacting density response function can be written as[99]

$$\chi_{\mathbf{G}\mathbf{G}'}^0(\mathbf{q}, \omega) = \frac{2}{\Omega} \sum_k^{\text{BZ}} \sum_{n < m} (f_{n\mathbf{k}} - f_{m\mathbf{k}+\mathbf{q}}) \langle u_{n\mathbf{k}} | e^{-i\mathbf{G}\cdot\mathbf{r}} | u_{m\mathbf{k}+\mathbf{q}} \rangle \langle u_{m\mathbf{k}+\mathbf{q}} | e^{i\mathbf{G}'\cdot\mathbf{r}} | u_{n\mathbf{k}} \rangle \times \left( \frac{1}{\tilde{\omega} + \epsilon_{n\mathbf{k}} - \epsilon_{m\mathbf{k}+\mathbf{q}}} - \frac{1}{\tilde{\omega} - (\epsilon_{n\mathbf{k}} - \epsilon_{m\mathbf{k}+\mathbf{q}})} \right). \quad (3.23)$$

where  $\tilde{\omega} = \omega + i\eta$ ,  $\Omega = \Omega_{\text{cell}} N_{\mathbf{k}}$  with  $\Omega_{\text{cell}}$  and  $N_{\mathbf{k}}$  being the unit cell volume and the number of  $\mathbf{k}$ -points, respectively,  $n, m$  denote band indices,  $f$  are occupation numbers,  $|u\rangle$  are the periodic part of the Bloch states of the crystal and  $\epsilon$  are the eigenenergies.

The limit  $\eta \rightarrow 0^+$  is taken as implied but often a finite  $\eta$  is used when integrating the response function in practice. This expression can be calculated directly for finite  $\mathbf{q}$  by sampling the Brillouin zone with a homogeneous  $\mathbf{k}$ -point sampling of  $\Delta\mathbf{k} = \mathbf{q}$ . In the optical limit, however, where  $\mathbf{q} \rightarrow 0$  this finite sampling becomes practically impossible. Instead, the asymptotic limit of the matrix elements, the occupation numbers and the energy denominator when  $\mathbf{q} \rightarrow 0$  is taken. For interband transitions when  $n \neq m$  the density response function in the optical limit becomes

$$\chi_{0,0}^{0,\text{inter}}(\mathbf{q} \rightarrow 0, \omega) = \frac{2}{\Omega} \sum_k^{\text{BZ}} \sum_{n < m} (f_{n\mathbf{k}} - f_{m\mathbf{k}}) |\mathbf{q} \cdot \langle u_{n\mathbf{k}} | \nabla_{\mathbf{q}} u_{m\mathbf{k}} \rangle|^2 \times \quad (3.24)$$

$$\left( \frac{1}{\tilde{\omega} + \epsilon_{n\mathbf{k}} - \epsilon_{m\mathbf{k}}} - \frac{1}{\tilde{\omega} - (\epsilon_{n\mathbf{k}} - \epsilon_{m\mathbf{k}})} \right). \quad (3.25)$$

where we have used that  $|u_{m\mathbf{k}+\mathbf{q}}\rangle \approx |u_{m\mathbf{k}}\rangle + \mathbf{q} \cdot \nabla_{\mathbf{q}} |u_{m\mathbf{k}}\rangle$  and the orthogonality of the Bloch states  $\langle u_{n\mathbf{k}} | u_{m\mathbf{k}} \rangle = 0$  for  $n \neq m$ . The matrix elements can then be obtained from  $k \cdot p$ -perturbation theory[99] as

$$\langle u_{n\mathbf{k}} | \nabla_{\mathbf{q}} u_{m\mathbf{k}} \rangle = \frac{\langle n\mathbf{k} | \hat{\mathbf{p}} | m\mathbf{k} \rangle}{\epsilon_m - \epsilon_n} \quad (3.26)$$

where  $\hat{\mathbf{p}} = -i\nabla$  is the momentum operator (not to be confused with the dipole moment of the previous chapter). The treatment for the intraband contribution  $n = m$  to the density response function takes a slightly different form. In this case  $\langle u_{n\mathbf{k}} | u_{n\mathbf{k}+\mathbf{q}} \rangle \rightarrow 1$  but the energy difference and the occupation factor difference go to zero. A careful analysis shows that

$$f_{n\mathbf{k}} - f_{n\mathbf{k}+\mathbf{q}} \approx -\mathbf{q} \cdot \nabla_{\mathbf{k}} f_{n\mathbf{k}} = -\mathbf{q} \cdot \frac{\partial f(\epsilon_{n\mathbf{k}})}{\partial \epsilon_{n\mathbf{k}}} \nabla_{\mathbf{k}} \epsilon_{n\mathbf{k}} \quad (3.27)$$

$$\frac{1}{\tilde{\omega} + \epsilon_{n\mathbf{k}} - \epsilon_{m\mathbf{k}}} - \frac{1}{\tilde{\omega} - (\epsilon_{n\mathbf{k}} - \epsilon_{m\mathbf{k}})} \approx \frac{2}{\tilde{\omega}^2} \mathbf{q} \cdot \nabla_{\mathbf{k}} \epsilon_{n\mathbf{k}}. \quad (3.28)$$

The intraband contribution to the density response function then becomes

$$\chi_{0,0}^{0,\text{intra}}(\mathbf{q} \rightarrow 0, \omega) = -\frac{4}{\Omega\omega^2} \sum_k^{\text{BZ}} \frac{\partial f(\epsilon_{n\mathbf{k}})}{\partial \epsilon_{n\mathbf{k}}} (\mathbf{q} \cdot \nabla_{\mathbf{k}} \epsilon_{n\mathbf{k}}) (\mathbf{q} \cdot \nabla_{\mathbf{k}} \epsilon_{n\mathbf{k}}) \quad (3.29)$$

The  $\nabla_{\mathbf{k}} \epsilon_{n\mathbf{k}}$  can be determined using the Hellman-Feynman theorem

$$\nabla_{\mathbf{k}} \epsilon_{n\mathbf{k}} = \nabla_{\mathbf{k}} \langle u_{n\mathbf{k}} | \hat{H}(\mathbf{k}) | u_{n\mathbf{k}} \rangle = \langle u_{n\mathbf{k}} | \nabla_{\mathbf{k}} \hat{H}(\mathbf{k}) | u_{n\mathbf{k}} \rangle = \langle n\mathbf{k} | \hat{\mathbf{p}} / m | n\mathbf{k} \rangle \quad (3.30)$$

In the case of low temperatures  $\frac{\partial f(\epsilon_{n\mathbf{k}})}{\partial \epsilon_{n\mathbf{k}}} \approx -\delta(\epsilon_{n\mathbf{k}} - \epsilon_F)$  and the intraband contribution reduces to an integral over Fermi surface. These results show that  $\chi^0 \propto q^2$  and that the density response function therefore goes to zero in the optical limit  $q \rightarrow 0$ . The dielectric function, however, assumes a finite value in the optical limit because of the  $q$ -dependence of the Coulomb kernel  $v_c(\mathbf{q}) = 4\pi q^{-2}$  which cancels the  $q$ -dependence of the density response function (see Eq. (3.20)).

# CHAPTER 4

## Summary of the results

---

In this chapter the most important results of the papers are summarized.

### 4.1 Paper I: Limitations of effective medium theory in multilayer graphite/hBN heterostructures

The motivation for hyperbolic metamaterials is often based on the framework of effective medium theory (EMT) in which the optical response is treated by an effective anisotropic dielectric tensor[19, 46, 76, 100]. The validity of the EMT description, Eqs. (2.62) and (2.63), depends on the subwavelength nature of the metallic and dielectric components compared to the electromagnetic field within the materials, which is why common wisdom dictates that EMT should become more accurate with decreasing component sizes (Sec. 2.5). However, once the component thickness reaches the atomic scale, quantum mechanical effects must be taken into account[77]. In this paper, we have investigated the extreme limit of atomically thin components by assessing the validity of effective medium theory for (doped) graphite/hexagonal boron nitride (hBN) heterostructures. Hyperbolic behaviour have been predicted in such heterostructures[101] and our work expands on those results.

By calculating the dielectric properties of finite heterostructures we show that the graphene/hBN layers close to the interfaces exhibit different dielectric properties compared with the properties of graphite/bulk hBN which makes EMT break down when the interface layers constitute a sufficiently large volume fraction of the heterostructure. In practice we find that this happens when the number of layers in a single component is 5 or less.

An improvement of effective medium theory (EMTi) is proposed by taking the changed interface properties into account. Here the two interface layers are regarded as an additional component in the heterostructure and their dielectric properties are determined by a finite slab calculation containing only the interface layers. The resulting effective medium theory provides a much better description of the dielectric properties of the heterostructures, especially for low frequencies.

We have investigated the validity of effective medium theory in describing the Fresnel reflection coefficients of the heterostructures and find that EMTi also improves the description of the reflection coefficients. However, significant discrepancies still exist

between EMTi and the true reflection coefficients and we show that these discrepancies are due to interference between multiple reflections within the heterostructures.

Finally, we show that even for component thicknesses where interface and interference effects are negligible, EMT can fail to describe the Purcell factor of the heterostructures. This failure is caused by ohmic losses in the heterostructure, which make fields within the heterostructure strongly evanescent and mean that the dipole field only probe the topmost layers and not the entire heterostructure.

## 4.2 Paper II: Bandstructure engineered metals for low-loss plasmonics

The problem of loss in plasmonic structures was described in Section 2.3.2. Losses have been shown to be fundamentally dominated by intrinsic ohmic losses occurring in the metallic parts of plasmonic components which highlights the need for new metals. The strategies undertaken so far, as explained in Section 2.3.2, have generally relied on the philosophy of reducing carrier concentrations to reduce the plasma frequencies and on reducing the relaxation rate by employing materials with more feasible manufacturing properties. The elusive loss-less metal band structure model provided an alternative route to eliminating losses by band structure engineering, however, the model remained in the theoretical realm at the time.

In this paper we show that some layered materials exhibit band structures with characters resembling the ideal loss-less metal. In particular, we find that 2H-TaS<sub>2</sub> (Fig. 4.1), 3R-NbS<sub>2</sub> and 1T-AlCl<sub>2</sub> all exhibit band structures with a narrow conduction band separated by finite energy gaps, however, the size of the energy gaps are insufficient to render the metals entirely loss-less. This discovery shows that the proposed band structure of the elusive loss-less metal is not just a theoretical construction, but belongs in the practical realm as well.

A super-cell calculation of an aluminium defect in 1T-AlCl<sub>2</sub> showed that the finite energy gaps indeed entailed a reduced relaxation rate compared to the constant relaxation rate approximation. To accurately reflect the decrease in density of states for scattering we employed a frequency dependent relaxation rate proportional to the joint density of states (JDOS)

$$\eta(\omega) \propto \frac{\text{JDOS}(\omega)}{\omega}, \quad (4.1)$$

which accurately described both the relaxation rate in the noble and layered metals.

Upon investigation of the merits of the layered metals, it was found that while the metals outperformed silver and gold in transformation optical applications this was not the case for surface plasmon wave guiding on single interfaces, where propagation lengths were larger on silver by orders of magnitude. This is caused by the large skin-depth of the electric field in the layered metals compared to the noble metals. In the latter the electric field is forced into the dielectric by the highly negative dielectric

function of the noble metals which reduces the skin depths and thus the metallic losses. By considering the propagation of the SRSPP in the thin-film waveguide geometry we show the increased field fraction within the metal leads to a comparable and sometimes improved performance of some of the layered metals to silver. These results show that the merits of a plasmonic material depend significantly on the specific application and in particular on the associated electric field distribution in the application.

The performance of the layered metals can be improved by increasing the size of the energy gaps. We show that such an effect can be engineered in layered metals by substituting the group V transition metals (Ta, Nb) with the less electronegative group IV transition metals (Ti, Zr, Hf) while compensating the loss of electrons by substituting some chalcogen atoms (S, Se, Te) with halogen atoms (Cl, Br, I) which leads to a significantly lower imaginary part of the dielectric function and much longer plasmon lifetimes than silver.

### 4.3 Paper III: Layered materials with hyperbolic light dispersion

It was shown in Section 2.5.1 that the performance of hyperbolic metamaterials was limited by the finite size of the metallic components that compose the hyperbolic metamaterials. As an alternative to metamaterials, it was recently discovered that some naturally occurring materials, such as bulk hexagonal boron nitride, exhibit hyperbolic properties. Due to their lack of artificial structuring, naturally hyperbolic materials are not subject to the limitations of hyperbolic metamaterials mentioned above, and as a consequence their hyperbolic response extends to much larger wave vectors.

In this paper, we have investigated the optical properties 31 layered transition metal dichalcogenides and find that *all* of them exhibit hyperbolic properties, that span frequencies ranging from the NIR to the UV. This result is interesting because it was previously argued that bulk hyperbolic materials were rare[19] in contrast to our results that indicate otherwise. Their hyperbolic properties are ultimately a consequence of their anisotropic crystal structure affecting the transition matrix elements of the density response function meaning that any anisotropic material should be expected to exhibit hyperbolic behaviour in some frequency regimes (provided that the momentum matrix elements are large enough to render the materials metallic).

By comparing with the Purcell factor of a hyperbolic metamaterial consisting of silver and SiO<sub>2</sub>, we show that the natural hyperbolic materials exhibit Purcell factors 3 orders of magnitude larger than the hyperbolic metamaterials; a direct consequence of the increased photonic density of states within the natural hyperbolic materials.

We show that the contribution to the Purcell factor from quenching can be minimized by employing one of the bandstructure engineered low-loss plasmonic materials from the previous paper (2H-HfBrS). For 2H-HfBrS, the low loss at the upper

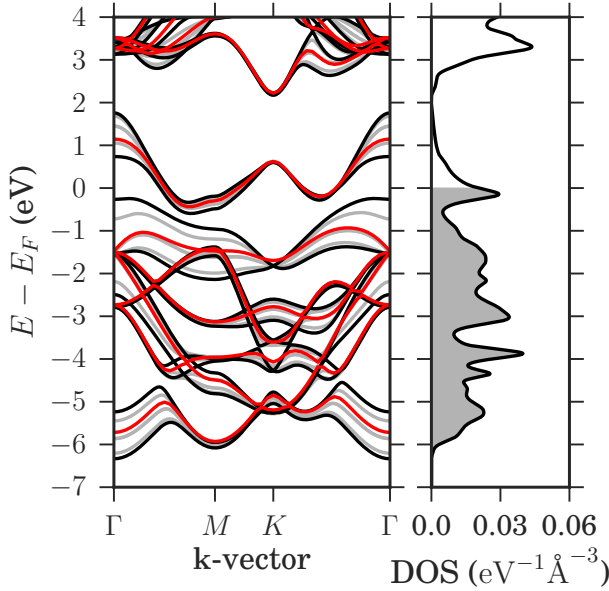


**Figure 4.1:** The bandstructure of 2H-TaS<sub>2</sub> (black lines) which resembles that of the elusive loss-loss metal depicted in Fig. 2.7(a). The grey lines depict the bandstructure along a displaced path in the out-of-plane direction. The monolayer bandstructure is shown in red.

frequency edge of the hyperbolic regime entails a rapid drop of the Purcell factor as soon the frequency is tuned out of the hyperbolic regime (Fig. 4.2). This drop could be taken advantage of if a quantum emitter can be tuned in and out of the hyperbolic regime, such that emission happens rapidly after the emitter is tuned into the hyperbolic regime. This effect is not observed in 2H-TaS<sub>2</sub> because the optical losses are considerably higher.

The hyperbolic frequency regimes of hyperbolic metamaterials are usually tuned by varying the metallic fill fraction. While this option is also available in van der Waals heterostructures of the layered TMDs, we show that the diverse electronic properties of the TMDs enable a similar effect whereby a significant tuning can be achieved by changing heterostructure components. The significant tailoring that can be achieved by this process is demonstrated by calculating the hyperbolic regimes of all two-component heterostructures (50% fill-fraction) and subsequently fitting them to the emission and absorption spectrum of an NV-center, resulting in many heterostructure candidates that improve the performance of the natural hyperbolic materials.

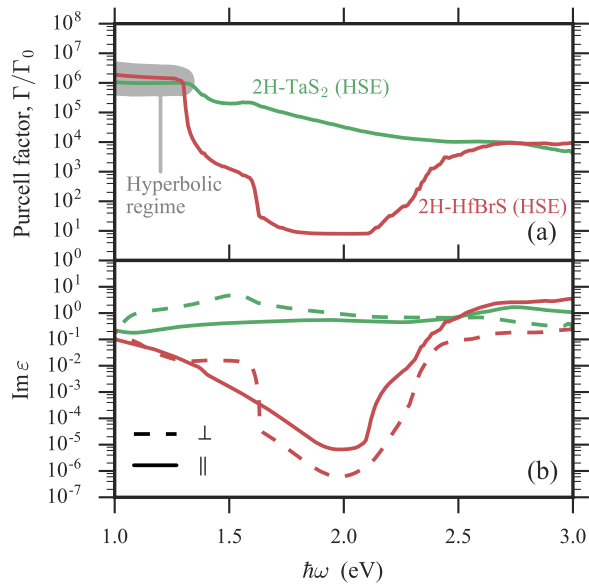


**Figure 4.2:** (a) Purcell factor and (b) imaginary part of the dielectric function of 2H-TaS<sub>2</sub> and the chalcogen-halogen layered compound 2H-HfBrS. Note that the lower losses of 2H-HfBrS entail a sharp drop in the Purcell factor as the frequency is tuned out of the hyperbolic regime.



# CHAPTER 5

## Papers

---

- 5.1 Paper I: Limitations of effective medium theory in multilayer graphite/hBN heterostructures

## Limitations of effective medium theory in multilayer graphite/hBN heterostructures

René Petersen\* and Thomas Garm Pedersen

*Department of Physics and Nanotechnology, Aalborg University, DK-9220 Aalborg East, Denmark  
and Center for Nanostructured Graphene (CNG), DK-9220 Aalborg East, Denmark*

Morten Niklas Gjerding and Kristian Sommer Thygesen

*Institute of Physics, Technical University of Denmark (DTU), DK-2800 Kgs. Lyngby, Denmark  
and Center for Nanostructured Graphene (CNG), DK-2800 Kgs. Lyngby, Denmark*

(Received 3 March 2016; revised manuscript received 2 June 2016; published 12 July 2016)

We apply effective medium theory (EMT) to metamaterials consisting of a varying number of consecutive sheets of graphene and hexagonal boron nitride, and compare this with a full calculation of the permittivity and the reflection based on the tight binding method and the transfer matrix method in order to study the convergence to EMT. We find that convergence is reached for both in-plane and out-of-plane directions already for five sheets but that for  $\approx 30$  sheets multiple reflection effects causes the reflection spectrum to differ from EMT. We show that modes that are evanescent in air are extremely sensitive to the electronic details of the sheets near the structure boundary and that EMT estimates poorly the reflection of these modes, causing an overestimation of the Purcell factor. Finally, we offer an improved EMT, which gives far better convergence in the low-energy regime.

DOI: 10.1103/PhysRevB.94.035128

### I. INTRODUCTION

Hyperbolic metamaterials (HMMs) have recently attracted much attention due to their interesting applications including hyperlenses and lifetime engineering [1–5]. Of particular interest are graphene based HMMs because of the possibility of exploiting the semimetallic nature of graphene in tuning of the optical properties in the THz regime via gating or doping [6,7]. Due to the subwavelength nature of these HMMs it has become common practice to homogenize the structure using effective medium theory (EMT) in order to facilitate a simpler description and focus on the HMM properties [5,8–10]. Experimental studies have confirmed the validity of EMT in Au/MgF<sub>2</sub>, Ag/MgF<sub>2</sub>, and Au/Al<sub>2</sub>O<sub>3</sub> heterostructures [5,11], but EMT is known to describe incorrectly the reflection of evanescent modes [12] and to fail describing even deep subwavelength structures in some cases [13]. EMT ignores effects near the boundaries between layers that may affect the electronic structure of the constituents and thereby the local refractive index, and the phase shifts introduced as light propagates through individual layers are treated in an average sense. For these reasons, it is important to investigate the accuracy and understand the limitations of EMT, also in the limit of extremely thin layers. In this work, we apply EMT to periodic and finite layered graphite-hexagonal boron nitride (Gr-hBN) heterostructures with a varying number of consecutive graphene/hBN sheets (see Fig. 1) and calculate the permittivity and the reflection. These structures constitute a strongly anisotropic system sufficiently simple to allow for modeling of the individual constituents as well as the full combined system using tight binding (TB), making Gr-hBN ideal to assess the validity of EMT in both in-plane and out-of-plane directions. We base our EMT calculations on the readily accessible permittivities of graphite and bulk hBN as well as graphene and monolayer hBN. We investigate periodic

structures of the form  $N \times \text{Gr} - M \times \text{hBN}$  where  $N$  and  $M$  denote the number of graphene and hBN sheets in the unit cell, but restrict our studies to structures for which  $M = N$  for simplicity. In the following we will denote such periodic structures by  $\{N, N\}$ , not to be confused with the notation  $(N, N)$ , which will be introduced later for finite structures. We have checked that our conclusions hold also for asymmetric structures for which  $M \neq N$ , but in the few cases where major differences arise, we provide an explicit discussion hereof.

In EMT, a uniaxial stratified periodic metamaterial consisting of a metal and a dielectric can be characterized by the effective diagonal permittivity tensor  $\epsilon^{\text{EMT}} = \text{diag}(\epsilon_{\parallel}^{\text{EMT}}, \epsilon_{\parallel}^{\text{EMT}}, \epsilon_{\perp}^{\text{EMT}})$ , with effective components given by [4]

$$\epsilon_{\parallel}^{\text{EMT}} = \rho \epsilon_{\parallel, \text{m}} + (1 - \rho) \epsilon_{\parallel, \text{d}}, \quad (1)$$

$$\frac{1}{\epsilon_{\perp}^{\text{EMT}}} = \frac{\rho}{\epsilon_{\perp, \text{m}}} + \frac{1 - \rho}{\epsilon_{\perp, \text{d}}}, \quad (2)$$

where  $\epsilon_{\text{m}} = \text{diag}(\epsilon_{\parallel, \text{m}}, \epsilon_{\parallel, \text{m}}, \epsilon_{\perp, \text{m}})$  and  $\epsilon_{\text{d}} = \text{diag}(\epsilon_{\parallel, \text{d}}, \epsilon_{\parallel, \text{d}}, \epsilon_{\perp, \text{d}})$  are the permittivity tensors of the metal and the dielectric and  $\rho$  is the fill fraction of metal, which will be  $\frac{1}{2}$  in all our calculations. By parallel ( $\parallel$ ) we refer to the in-plane component (perpendicular to the optical axis) and by perpendicular ( $\perp$ ) to the out-of-plane component (parallel to the optical axis). We will refer to a single atomic monolayer of graphene or hBN within the structure as a sheet and to a stack of identical sheets as a layer. Thus, Fig. 1(b) shows four layers and twelve sheets. When referring to the graphitelike or the bulk-hBN-like parts of the structure we will do so by writing Gr or hBN, respectively. It would be incorrect to refer to the graphitelike part as graphite or graphene since the presence of the hBN changes its properties.

To assess how well EMT describes the properties of the structure we calculate the permittivity and the reflection spectrum. For the parallel case we compare directly the permittivity calculated using a full model with the EMT permittivity, while for the perpendicular case we calculate the

\*rp@nano.aau.dk

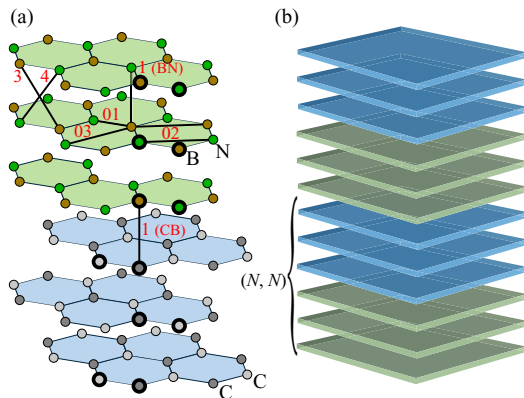


FIG. 1. (a) Model of the periodic structure used for atomistic calculations with coupling constants indicated by red numbers and the atoms of the unit cell marked with thick stroke. The shown structure is denoted by  $\{3,3\}$  ( $3 \times \text{Gr} - 3 \times \text{hBN}$ ). Notice that graphite is AB stacked while hBN is AA' stacked. The interlayer distance is  $3.35 \text{ \AA}$ . (b) Schematic of the layered structure used for reflection calculations.  $(N, N)$  denotes the finite building block of the stack which for the case shown is  $(3,3)$ . We denote the entire 12-sheet stack shown by  $2 \times (3,3)$ .

permittivity of each sheet of the unit cell and employ the transfer matrix method (TMM) to calculate the reflection in the full model and in EMT, in order to account for the field variation throughout the structure. We expect the permittivity of  $\{N, N\}$  structures to converge to the bulk-based EMT value as the number of sheets increases. On the other hand, as the layers become thicker we no longer satisfy the condition for EMT that the period of the structure is much larger than the wavelength, especially for large  $k$  wave vectors. Thus, we expect EMT to work well in a certain range of the number of sheets.

Since many applications of graphene-based HMMs rely on the ability to tune the properties by doping, we investigate in detail how doping of the structure influences the convergence and we provide a simple improvement of EMT to better describe doped structures. Finally, we calculate Purcell factors to see how EMT performs in applications relying on lifetime engineering.

## II. METHODS

We use a nonorthogonal  $\pi$ -electron TB model to calculate eigenenergies and eigenmodes of the structure shown in Fig. 1(a), i.e., we solve

$$\mathbf{H} \cdot \mathbf{c} = E \mathbf{S} \cdot \mathbf{c} \quad (3)$$

using standard methods. For the Gr part we use the DFT-LDA fitted TB parameters suggested by Grüneis *et al.* [16] while for the hBN part we use our own fit to a DFT band structure by employing a least-squares technique. We fit all four  $\pi$  bands along the line  $\Gamma$ - $M$ - $K$ - $H$ - $L$ - $A$  [16] of the irreducible Brillouin zone (BZ) starting  $\frac{6}{7}$  along the line  $\Gamma$ - $M$  and ending  $\frac{1}{7}$  along

the line  $L$ - $A$ , effectively including only the parts of the band structure that contribute to optical transitions below  $\approx 8 \text{ eV}$ . The zero point of energy in Eq. (3) is chosen as the graphene Dirac point such that for all calculations  $E_F = 0.0 \text{ eV}$  corresponds to undoped structures.

DFT band structures and optical response have been calculated using the electronic structure code GPAW [17]. We use a plane-wave cutoff energy of  $600 \text{ eV}$  and a  $\Gamma$ -centered Monkhorst-Pack  $k$ -point sampling of size  $30 \times 30 \times 10$  and  $120 \times 120 \times 38$  in ground-state calculations for the band structure and for the response calculations, respectively. For graphite, we use a higher  $k$ -point sampling of  $60 \text{ \AA}$  in the vicinity of the edge from the  $K$  to  $H$  points of the BZ. We use a Fermi smearing of  $25 \text{ meV}$ . The local density approximation (LDA) was chosen as exchange-correlation functional since it is not expected to influence the conclusions compared to other functionals [18]. The optical response has been calculated in the linear response regime [19] including local field effects using a cutoff energy of  $60 \text{ eV}$ , at which the local field effects were found to be converged, and a level broadening of  $5 \text{ meV}$ . Excitonic effects are ignored. The BZ integrations are done using the linear tetrahedron integration method [20].

In all calculations we use the graphite lattice parameters, that is,  $a_0 = 2.46 \text{ \AA}$  for the lattice constant and  $c_0 = 3.35 \text{ \AA}$  for the sheet distance [16]. Experimental and *ab initio* studies have found the lattice constant of bulk hBN to be  $2\%$  greater than that of graphite and the sheet distance to be  $3.33 \text{ \AA}$  [21,22], but as an approximation we ignore these differences since they are expected to have no significant influence on our results. We use AA' stacking for the hBN part (boron over nitrogen) [22] and AB stacking (boron over carbon) for the Gr-hBN interface [23], and assume that the Gr and hBN layers are not rotated with respect to each other.

The hBN TB parameters are given in Table I, where the notation corresponds to Fig. 1(a). We have chosen our conventions for couplings in hBN to be similar to those of Ref. [16] for graphite, except for  $\gamma_3$  and  $\gamma_4$  where the interpretation is slightly different.

We calculate the permittivity by: (i) calculating the real part of the interband conductivity  $\sigma_{\text{inter}}(\omega)$  in the zero-broadening limit; (ii) folding this with a Lorentzian to reintroduce broadening; (iii) doing a Kramers-Kronig transformation to find the imaginary part; (iv) adding the complex intraband conductivity  $\tilde{\sigma}_{\text{intra}}(\omega)$ ; and finally, (v) determining the permittivity from  $\epsilon = \epsilon_{\infty} + i\tilde{\sigma}(\omega)/\epsilon_0\omega$  [24], where  $\epsilon_{\infty}$  is treated as a fitting parameter accounting for  $\sigma$  electrons and  $\tilde{\sigma}(\omega)$  is the complex conductivity. In all spectra, unless otherwise stated, the

TABLE I. hBN TB parameters. Onsite energies and hopping elements ( $E$  and  $\gamma$ , respectively) are specified in eV, while overlap integrals ( $s$ ) are unitless. The carbon-boron coupling  $\gamma_1^{\text{CB}}$  is taken from [14].

$E_0^{\text{B}} = 1.6026$	$E_0^{\text{N}} = -2.9180$	$\gamma_{01} = -2.5989$
$\gamma_{02}^{\text{BB}} = -0.17068$	$\gamma_{02}^{\text{NN}} = -0.37578$	$\gamma_{03} = -0.4056$
$\gamma_1^{\text{BN}} = 0.13009$	$\gamma_3 = 0.57442$	$\gamma_4 = -0.16411$
$\gamma_1^{\text{CB}} = 0.4300$	$s_{01} = 0.07760$	$s_{02}^{\text{BB}} = 0.04588$
$s_{02}^{\text{NN}} = 0.065273$	$s_{03} = 0.052306$	$s_1 = -0.10355$

broadening is set to 50 meV and the thermal energy to 25 meV. The real part of the interband conductivity is found using the first-order perturbation theory result [24,25]

$$\sigma_{\text{inter}}(\omega) = \frac{e^2}{4\pi^2\hbar^2\omega} \sum_{\substack{m \\ n > m}} \int_{\text{BZ}} f_{mn} M_{mn} \delta(E_{nm} - \hbar\omega) d^3k, \quad (4)$$

where  $E_{nm} = E_n - E_m$  is the energy difference between band  $n$  and  $m$ ,  $f_{mn} = f(E_m) - f(E_n)$  is the Fermi occupation factor, and  $M_{mn} = |P_{mn}|^2$  are the absolute squared momentum matrix elements (MMEs) given by either

$$M_{\parallel, mn} = \frac{1}{2} |\langle \Psi_m | \frac{\partial \hat{H}}{\partial k_x} | \Psi_n \rangle|^2 + \frac{1}{2} |\langle \Psi_m | \frac{\partial \hat{H}}{\partial k_y} | \Psi_n \rangle|^2 \quad (5)$$

for the parallel component of the conductivity, or

$$M_{\perp, mn} = |\langle \Psi_m | \frac{\partial \hat{H}}{\partial k_z} | \Psi_n \rangle|^2 \quad (6)$$

for the perpendicular component, with  $\Psi$  being the wave function of the system constructed from the eigenvectors found from Eq. (3) and the atomic  $\pi$  wave functions. The MME for the parallel component has been symmetrized in  $x$  and  $y$  to allow the  $\mathbf{k}$  integration to be done over the irreducible BZ only [25].

The intraband conductivity is modeled as a Drude term  $\sigma_{\text{intra}}(\omega) = i\varepsilon_0\omega_p^2/(\omega + i\Gamma)$  where  $\Gamma$  is the broadening and  $\omega_p$  is the plasma frequency given by

$$\omega_p^2 = \frac{-e^2}{4\pi^3\hbar^2\varepsilon_0} \sum_n \iint_{\text{BZ}} M_{nn} \delta(E_n - E) d^3k f'(E) dE. \quad (7)$$

In Fig. 2, we present the parallel and perpendicular permittivity of bulk hBN and graphite calculated using both DFT and TB. To match the DFT calculations, the real part of the TB spectrum for bulk hBN has been shifted by an additive

constant of 1.70 for the parallel component and by 1.15 for the perpendicular component, in order to account for energetically distant transitions due to  $\sigma$  electrons that are not included in our TB model [25,26]. For the parallel component the real and imaginary parts are in excellent agreement with DFT, while the perpendicular component is less well reproduced by TB due to the distribution of  $k$  points in the fitting procedure favoring the more important in-plane parameters. For graphite we shift the real part of the parallel permittivity by 1.1 to match the spectrum measured by Taft and Philipp [15]. For the perpendicular component contradicting values of the permittivity are reported in the literature [27] and we therefore shift the TB curve by 1.62 to match our DFT calculations. Excellent agreement between DFT and TB is found, except for low energies due to difficulties with obtaining converged results in DFT in this regime. We observe also good agreement with experiment for the parallel component. The disagreement around 4.25 eV is partly explained by broadening such that increasing the broadening in our spectra gives better agreement (not shown).

Equation (4) is accurate for homogeneous materials such as bulk hBN described above, in which local field effects due to atomic-scale variations can be ignored, and the driving field considered to be approximately constant throughout the entire structure. For inhomogeneous materials such as Gr/hBN heterostructures, however, this approximation applies only to the parallel field component  $\mathcal{E}_{\parallel}$ , for which the electromagnetic boundary condition states that  $\mathcal{E}_{\parallel,1} = \mathcal{E}_{\parallel,2}$  with 1 and 2 referring to the two sides of a boundary. The perpendicular field component  $\mathcal{E}_{\perp}$  varies throughout the heterostructure as can be seen from the boundary condition  $\varepsilon_{\perp,1}\mathcal{E}_{\perp,1} = \varepsilon_{\perp,2}\mathcal{E}_{\perp,2}$  [3]. Given that  $\varepsilon_{\perp,1} \neq \varepsilon_{\perp,2}$ , we will have also  $\mathcal{E}_{\perp,1} \neq \mathcal{E}_{\perp,2}$ .

To include the field variation we calculate the contribution to the permittivity from each sheet of an  $\{N, N\}$  structure, from here referred to as the projected permittivity, and use the TMM to calculate the reflection from finite stacks consisting of  $S$  sheets in an ambient of air in the configurations  $\frac{S}{2N} \times (N, N)$

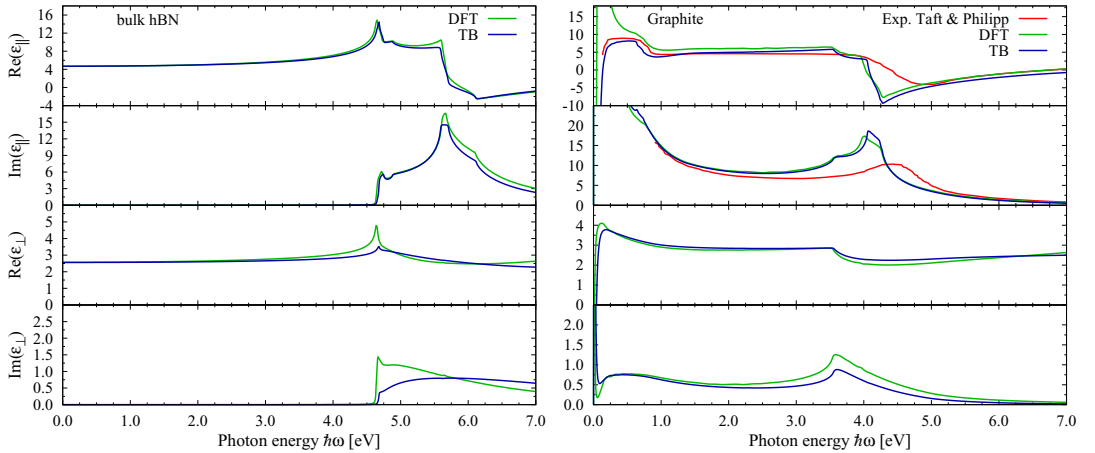


FIG. 2. Comparison between the permittivity of bulk hBN (left) and graphite (right) calculated using DFT and TB with a broadening of  $\Gamma = 5$  meV. The two top panels show the real and imaginary parts of  $\varepsilon_{\parallel}$  and the bottom two panels show the real and imaginary parts of  $\varepsilon_{\perp}$ . The real parts of  $\varepsilon_{\parallel}$  and  $\varepsilon_{\perp}$  have been shifted by 1.70 and 1.15 for bulk hBN and by 1.1 and 1.62 for graphite, to account for  $\sigma$  electrons. For graphite we show also experimental results from Taft and Philipp [15] for the parallel component.

for which  $\frac{S}{2N}$  is an integer. Here,  $(N, N)$  should be understood as the finite building block consisting of  $N$  sheets of Gr and  $N$  sheets of hBN [cf. Fig. 1(b)] with the sheet permittivities given by the projected permittivities of the corresponding periodic structure  $\{N, N\}$ . We ignore the different environment of the sheets near the air boundaries. The choice of the topmost layer has a significant impact on the reflection [12], and therefore we average the reflection of the two possible configurations in all calculations. The TMM catches the field variation, since we, in effect, calculate the field strength in each sheet of the structure.

To calculate the conductivity due to the atoms belonging to the set  $A = \{\alpha_1, \alpha_2, \dots\}$  of atom indices  $\alpha_n$ , we need only change the MME in Eqs. (4) and (7). To this end, we define the projected MME

$$P_{mn}^A = \frac{1}{2} \sum_{\alpha \in A} \sum_{\beta} [c_{m,\alpha}^* c_{n,\beta} + c_{m,\alpha} c_{n,\beta}^*] \langle \alpha | \hat{p} | \beta \rangle, \quad (8)$$

where, e.g.,  $c_{m,\alpha}$  refers to element  $\alpha$  of eigenvector  $m$  and  $\langle \alpha | \hat{p} | \beta \rangle$  is the MME between the atomic  $\pi$  wave functions  $\alpha$  and  $\beta$ . If we sum over all such disjoint sets we get the MME for the entire structure  $P_{mn} = \sum_A P_{mn}^A$ . Now, we wish to define the projected conductivity  $\sigma^A$  due to the atoms belonging to  $A$  such that  $\sigma = \sum_A \sigma^A$ , that is, the projected conductivities should sum up to the total conductivity. Defining the squared projected MME as

$$\begin{aligned} M_{mn}^A &= \frac{1}{2} \sum_B (P_{mn}^{B*} P_{mn}^A + P_{mn}^{A*} P_{mn}^B) \\ &= \frac{1}{2} P_{mn}^A P_{mn}^{A*} + \frac{1}{2} P_{mn}^{A*} P_{mn}^A \\ &= \text{Re}(P_{mn}^A P_{mn}^{A*}), \end{aligned} \quad (9)$$

and substituting  $M_{mn}$  with  $M_{mn}^A$  in Eq. (4), it is an easy task to show that  $\sigma^A$  sum up to  $\sigma$ . To find the conductivity of a single sheet we identify the indices of the unit cell atoms belonging to this sheet, e.g., numbering the unit cell atoms from below, the bottom Gr sheet of Fig. 1(a) is described by the set  $A_1 = \{1, 2\}$ , the next Gr sheet by  $A_2 = \{3, 4\}$ , etc.

In Fig. 3, we show the projected sheet conductivity for a  $\{7, 7\}$  structure along with the conductivity of graphite and bulk hBN divided by 7. We show only sheets 1–4 (S1–S4) as, for symmetry reasons, S5 is identical to S3, etc. Sheets that are close to the boundary (S1) derive characteristics from the other material: The conductivity of hBN S1 has a peak at 4.1 eV that coincides with the Gr sheets and also nonzero conductivity below the band gap that cannot be attributed to broadening, while Gr S1 has a peak at 5.7 eV coinciding with the hBN sheets. We have checked that the projected conductivities sum up to the conductivity for the entire structure. Overall, close resemblance with the bulk conductivity is seen (also for the out-of-plane conductivity, which is not shown), suggesting that the response should be well described using bulk values. From the permittivities of the individual sheets it is a simple matter to calculate the reflection from the finite structure using the TMM and the Fresnel reflection coefficients between two anisotropic materials given by Eq. (A10) of Appendix.

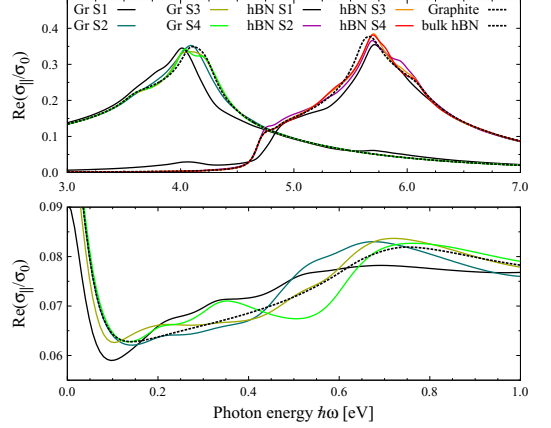


FIG. 3. Projected conductivity in the energy range 3–7 eV (top) and 0–1 eV (bottom) of a  $\{7, 7\}$  structure along with the graphite/bulk hBN conductivity divided by 7. The conductivity is given in units of the graphene minimum conductivity  $\sigma_0 = e^2/4h$  [24].

### III. RESULTS AND DISCUSSION

We have calculated  $\varepsilon_{||}$  for  $E_F = 0.0$  eV for several periodic Gr-hBN heterostructures in order to investigate the convergence to EMT. We expect the TB calculations to converge to EMT as the number of sheets is increased, since deviations for thin layers are merely a measure of the importance of the Gr-hBN coupling ( $\gamma_1^{\text{CB}}$ ) and of the difference between the individual constituents and their bulk counterparts (that is, graphite and bulk hBN), both of which vanish for increasing number of layers. Local field variations can be safely ignored in the parallel case as it has been argued above.

In Fig. 4, we show the results where the colored lines are full TB calculations using Eq. (4), the solid black curve is EMT based on permittivities of graphite and bulk hBN, and the dashed black curve is EMT based on graphene and monolayer hBN. Only for the  $\{1, 1\}$ ,  $\{3, 3\}$ , and  $\{5, 5\}$  cases we find significant discrepancies compared to EMT (bulk) while for  $\{11, 11\}$  the curves are difficult to distinguish on the chosen scale for both the real and imaginary part. For reference, we show in the bottom panel the absolute value of the deviation from EMT in percent for the imaginary part of  $\varepsilon_{||}$  calculated as  $|\text{Im}(\varepsilon_{||}^{\text{TB}} - \varepsilon_{||}^{\text{EMT}})|/\text{Im}(\varepsilon_{||}^{\text{EMT}})$ . For the low-energy spectrum the convergence is slower than it may be expected. It is usually stated that EMT works well when the wavelength is much larger than the period of the structure [12], and this is true when applying EMT to calculations in which the phase of the incoming light is important. However, Fig. 4 represents a study of convergence in electronic structure for which the phase of the incoming light plays no role.

One may intuitively expect that EMT based instead on monolayer permittivities is in good agreement with the  $\{1, 1\}$  structure, but the dashed black curve of Fig. 4 shows that this is not the case. Monolayer graphene or hBN in a periodic structure behaves rather differently than its isolated counterparts, as one also finds if the projected conductivity

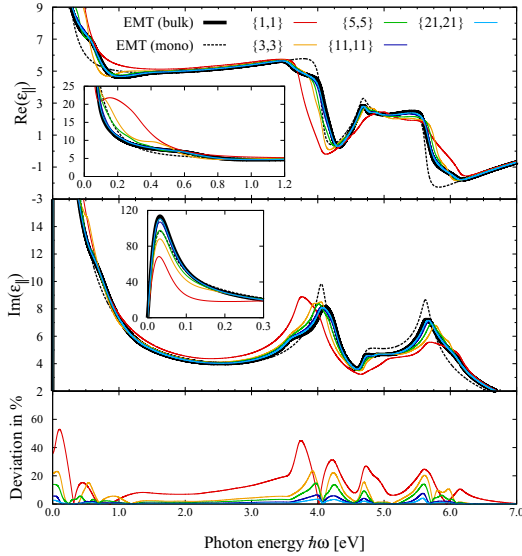


FIG. 4. Real (top) and imaginary (middle) part of the parallel permittivity  $\epsilon_{\parallel}$  versus bulk and monolayer based EMT for  $E_F = 0.0$  eV. The insets show a zoom of the low-energy region. The bottom panel shows the absolute value of the deviation from EMT for the imaginary part in percent

of the Gr or hBN sheet of a {1,1} structure is calculated (not shown). In the left panel of Fig. 5, we plot the equivalent of Fig. 4 for  $E_F = 0.5$  eV. From this plot it is seen that the convergence to EMT (bulk) is slower than for  $E_F = 0.0$  eV in the same energy range and that, in particular for the {1,1},

{3,3}, and {5,5} structures, EMT predicts the incorrect sign of  $\text{Re}(\epsilon_{\parallel})$  in some energy ranges.

One of the major deficiencies of EMT is the failure to include the coupling between the layers, thus, we suggest a simple improvement to EMT, which significantly improves the slower convergence in doped structures for low energies, and we refer in the following to this as EMTi. Many applications of graphene-based devices rely on the response in the regime close to  $2E_F$ , thus, good convergence in this regime is important. We consider the effective medium to consist of three materials: bulk Gr, bulk hBN, and an interface layer. The interface layer is described as a finite slab of graphene on hBN, such that the thickness of the slab is  $2c_0$ , and its permittivity is calculated using the in-plane hopping parameters of graphite and bulk hBN as well as the carbon-boron coupling  $\gamma_1^{\text{CB}}$ . We then average these three materials according to

$$\epsilon_{\parallel}^{\text{EMTi}} = \rho_m \epsilon_m + \rho_d \epsilon_d + (1 - \rho_m - \rho_d) \epsilon_{\text{interface}}, \quad (10)$$

$$\frac{1}{\epsilon_{\perp}^{\text{EMTi}}} = \frac{\rho_m}{\epsilon_m} + \frac{\rho_d}{\epsilon_d} + \frac{1 - \rho_m - \rho_d}{\epsilon_{\text{interface}}},$$

where  $\rho_m$  and  $\rho_d$  are the fractions of metal and dielectric, respectively, and  $\epsilon_{\text{interface}}$  is the permittivity of the graphene/hBN slab. For a {5,5} structure, for example, we would have  $\rho_m = 0.3$  and  $\rho_d = 0.3$ . In this way the effect of coupling between Gr and hBN is to some extent included in the effective medium.

In the right panel of Fig. 5 we show the results of using EMTi. From the bottom panels showing the deviations it is clear that EMTi offers an improvement compared to ordinary EMT. The huge improvement on the {1,1} structure is somewhat surprising, and suggest that in this structure the effects of interlayer coupling between Gr and hBN are more important than the effects of periodicity. For energies above  $3E_F$  we see only minor improvement using EMTi.

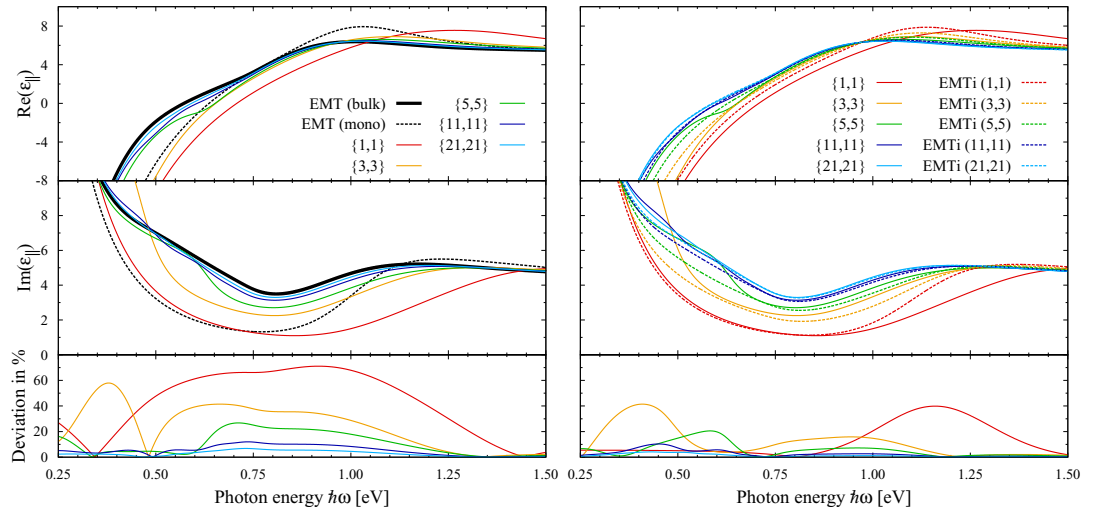


FIG. 5. Convergence to EMT (left) and EMTi (right) for  $E_F = 0.5$  eV. The top panels show  $\text{Re}(\epsilon_{\parallel})$ , the middle panels  $\text{Im}(\epsilon_{\parallel})$ , and the bottom panels the absolute value of the deviation from EMT/EMTi for the imaginary part in percent.

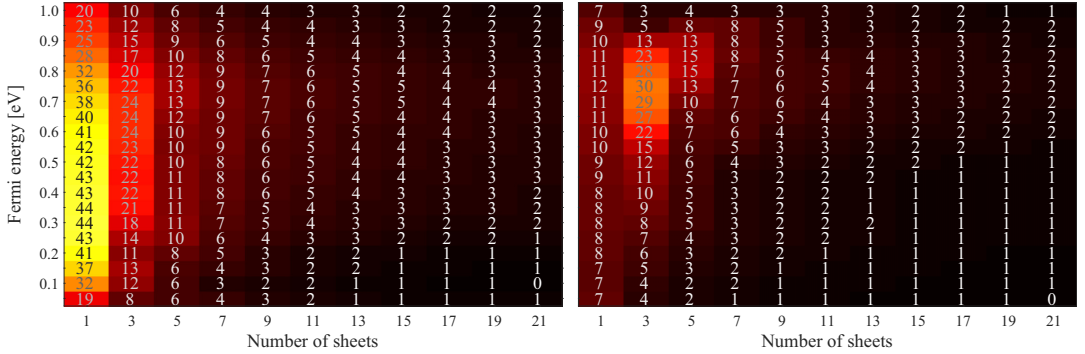


FIG. 6. Compilation of the averaged absolute value of the deviation of TB from EMT (left) and EMTi (right) in percent for a number of layers and Fermi levels. The average is taken over the energy interval 0 eV to  $3E_F$ .

To provide an overview of the error introduced using EMT, we show in the left and right panels of Fig. 6 a compilation of the averaged absolute value of the deviation for  $\text{Im}(\epsilon_{\parallel})$  in percent calculated using EMT and EMTi, respectively, for different structures and for a number of Fermi levels. The average is taken over the energy interval 0 eV to  $3E_F$ , since for higher energies the spectrum is only weakly dependent on  $E_F$ . We find that for all structures the error reaches a maximum at a certain value of  $E_F$  both for EMT and for EMTi. This can be explained by comparing the band structure of the full structure with the band structures of the constituents on which EMT and EMTi are based. One finds then that for these particular Fermi levels, the averaging from 0 to  $3E_F$  includes predominantly transitions between states of the band structures that differ strongly. Large deviations from EMT are seen in the left panel, and these deviations exist over a broad range of  $E_F$ . Small structures in particular are consistently ill described in EMT. Great improvement is found by using EMTi, especially for the  $\{1,1\}$  structure which is well described for all  $E_F$ , but also for larger structures. Generally, we find that although the deviation in some cases increases in EMTi, the large deviations are confined to a smaller interval of  $E_F$ .

For the perpendicular permittivity  $\epsilon_{\perp}$ , we take into account the local field variation due to the stratified nature of the structure using the approach described in Sec. II. TMM does not allow us to directly calculate the permittivity, and so our figure of merit becomes the reflection. In Fig. 7, we show for  $E_F = 0.5$  eV the reflection  $|r_p|^2$  of  $p$ -polarized light for two incident angles from the stacks  $210 \times (1,1)$ ,  $70 \times (3,3)$ ,  $42 \times (5,5)$ ,  $14 \times (15,15)$ ,  $10 \times (21,21)$ , and  $6 \times (35,35)$  all of thickness  $420c_0$ , and from the corresponding effective medium using EMT (black line). For  $\theta_{\text{incident}} = 0^\circ$  we probe only the parallel component of the permittivity tensor, thus, we expect rapid convergence to EMT for  $\hbar\omega > 3E_F$  because we have seen that the permittivity converges rapidly in this range. For the stacks  $210 \times (1,1)$ ,  $70 \times (3,3)$ , and  $42 \times (5,5)$  the convergence is as expected in the shown energy range, while for  $14 \times (15,15)$ ,  $10 \times (21,21)$ , and  $6 \times (35,35)$  the convergence is only as expected in the low-energy regime while in the range 4–7 eV deviations from EMT that cannot be attributed to the EMT permittivity are seen. These deviations

stem from interference effects due to multiple reflections at the interfaces between Gr and hBN layers that are not present in the EMT model, and these effects become increasingly important at smaller wavelengths (in the structure). To see this we plot also the reflection from a stack modeled as 12 layers of alternating graphite and bulk hBN each of thickness  $35c_0$ , and we denote this stack as  $6 \times (35B,35B)$  to emphasize that we use the bulk and not the sheet permittivities. The resemblance with the corresponding curve based on projected sheet permittivities confirms that the deviations from EMT are in fact caused by multiple reflections, and thereby that the permittivity has converged to the EMT value. From the insets it

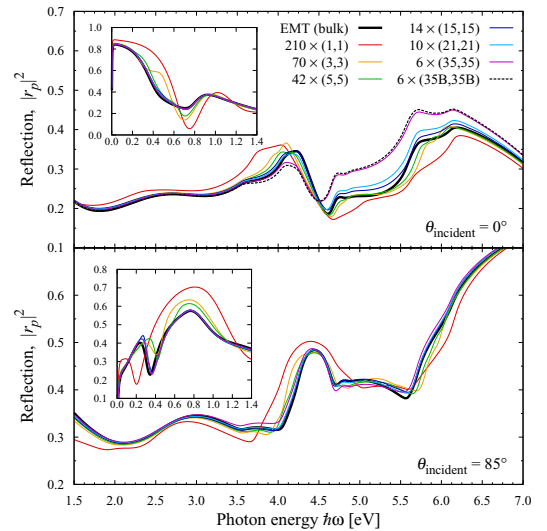


FIG. 7. Reflection of  $p$ -polarized light by the shown structures in an ambient of air at two angles of incidence and at  $E_F = 0.5$  eV. The dashed black curve in the top panel is the reflection by a layered structure built using  $\epsilon$  of graphite and bulk hBN. The insets show the spectral range between 0 eV and 1.4 eV.

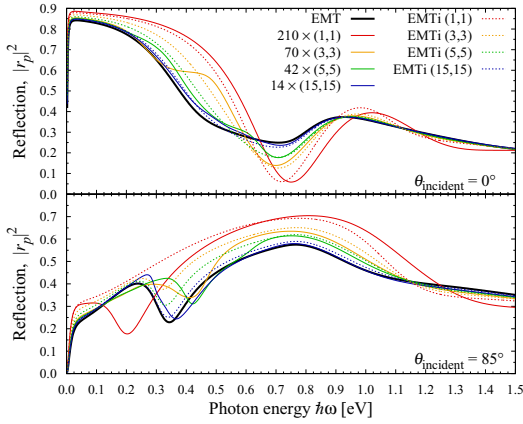


FIG. 8. Reflection of  $p$ -polarized light by the shown structures in an ambient of air at two angles of incidence and at  $E_F = 0.5$  eV, calculated using full TB permittivities and EMTi. For easy comparison, we show also the EMT result (solid black line).

is clear that the convergence is slow for  $h\omega < 3E_F$  as expected from the discussion of Fig. 5.

For  $\theta_{\text{incident}} = 85^\circ$  we probe primarily  $\varepsilon_{\perp}$ . At this angle of incidence we expect multiple reflections to give a much smaller contribution. In the bottom panel of Fig. 7, it can be seen that the reflection spectrum converges to the EMT spectrum calculated using Eq. (2) and that the convergence is as fast as for  $\varepsilon_{\parallel}$ . Small deviations are still seen in the range 4–7 eV due to multiple reflections, but they are much smaller than for  $\theta_{\text{incident}} = 0^\circ$ . We show in Fig. 8 the reflection spectra calculated using the EMTi permittivities from Eq. (10) and compare with full TB-based spectra. It is clear that the convergence to EMTi is improved especially for normal incidence, where only  $\varepsilon_{\parallel}$  is probed, but also at  $\theta_{\text{incident}} = 85^\circ$  showing that also the perpendicular permittivity is described better in EMTi.

We have checked that our results remain valid also for asymmetric structures, but we remark that for structures with low absorption, that is, if the number of graphene sheets is low compared to the number of hBN sheets, multiple reflections become more important and may cause deviations from EMT if the number of layers is large. In particular, we have checked our results for a  $15 \times (3,25)$  structure (3 Gr sheets per unit cell) and found that multiple reflections cause major deviations from EMT while for a  $4 \times (3,25)$  good agreement with EMT is found.

Calculating projected permittivities and using the TMM to include the field variation is rather tedious. Therefore, one may be tempted to calculate simply the perpendicular response of the entire structure by using the MMEs Eq. (6) in Eqs. (4) and (7), thereby ignoring the field variation throughout the structure. We show in Fig. 9, that this method does not provide convergence to EMT and thus, that this simpler method of calculation is not feasible for the structures considered. The observed convergence is merely an expression for convergence in the electronic structure of the considered

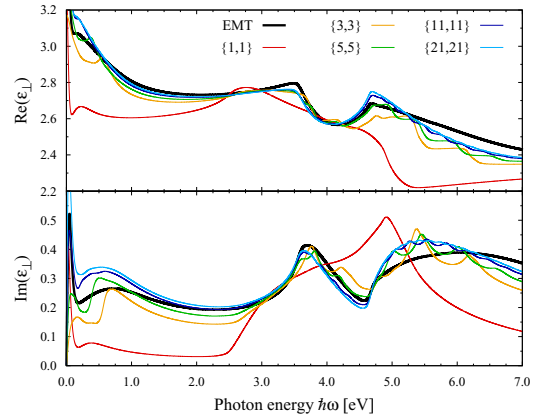


FIG. 9. Real (top) and imaginary (bottom) part of the perpendicular permittivity calculated using the MMEs Eq. (6) and thereby ignoring local field effects. This simpler method of calculation does not agree well with EMT, showing the importance of local field effects in the studied heterostructures.

structures, but this is generally not the same as convergence in optical response due to the importance of local field effects in heterostructures. We stress, however, that for asymmetric structures with  $M \neq N$  ignoring the field variation is a reasonable approximation if one layer is much thicker than the other. We have run simulations for  $\{3, M\}$  and  $\{M, 3\}$  structures with  $M = 1, 5, 7, 11, 17, 25$  (not shown) and found reasonable agreement with EMT for  $M = 11$  and above, although the convergence is slow.

Finally, we have calculated also the enhancement of spontaneous emission (the Purcell factor) of a dipole oriented parallel to and located a distance  $h = 20$  nm above the surface of a Gr/hBN stack using the expression in Ref. [28]. Both propagating and evanescent modes of  $s$  and  $p$  polarization contribute to the enhanced emission, although the huge Purcell factors that have been reported for HMMs [28,29] are due to the coupling of evanescent modes of large parallel wave-vector component  $k_x$  with the HMM. When entering the structure the perpendicular wave-vector component will be  $k_z^s = \sqrt{\varepsilon_{\parallel} k_0^2 - k_x^2}$  and  $k_z^p = \sqrt{\varepsilon_{\parallel} k_0^2 - (\varepsilon_{\parallel}/\varepsilon_{\perp}) k_x^2}$  where  $k_0 = \omega/c$  is the vacuum wave number, for  $s$ - and  $p$ -polarized modes, respectively. If  $k_x$  is large, both  $k_z^s$  and  $k_z^p$  can have large (positive) imaginary parts, and this is the case also in the hyperbolic regime where  $\text{Re}(\varepsilon_{\parallel})\text{Re}(\varepsilon_{\perp}) < 0$  because of losses. The large imaginary part causes these modes to decay rapidly within the structure and therefore to see only the topmost sheets of the structure. Thus, even though the wavelength of the incoming light may be sufficiently large that EMT should hold, the rapid decay of the modes may cause EMT to break down far sooner than anticipated. We illustrate this in Fig. 10, where we plot the reflection coefficient of  $p$ -polarized evanescent modes of energy  $h\omega = 0.30$  eV incident on the stacks  $42 \times (5,5)$ ,  $14 \times (15,15)$ , and  $6 \times (35,35)$  and on the corresponding effective medium, all with  $E_F = 0.5$  eV. At this Fermi level these structures all exhibit hyperbolic behavior in

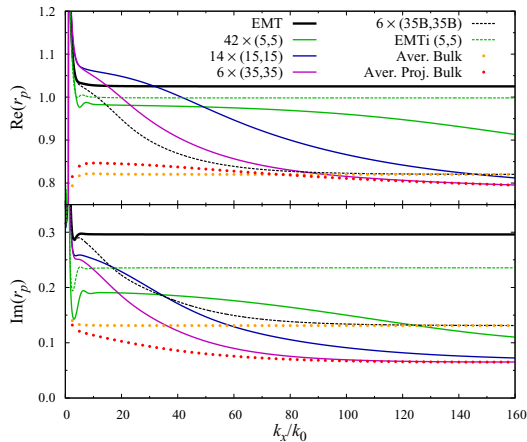


FIG. 10. Real and imaginary part of the reflection coefficient for  $k_x/k_0$  up to 160. The energy is  $\hbar\omega = 0.3$  eV and the Fermi level is  $E_F = 0.5$  eV. The red dots represent the average of the reflection coefficient from a stack of graphite and bulk hBN both of thickness  $420c_0$ . The same for the orange dots, but using the projected permittivities from a  $\{35,35\}$  structure for the 17 topmost layers and the graphite/bulk hBN value for remaining layers.

the energy range 50 meV to 0.6 eV. The pole near  $k_x = k_0$  corresponds to a surface plasmon excitation typical for a  $p$ -polarized wave incident on a metal/dielectric interface. We remark that reflection coefficients greater than unity for modes of  $k_x > k_0$  impose no violation of energy conservation due to their nonpropagating character in the medium of incidence.

For  $k_x \approx 5k_0$  EMT breaks down even for the very thin but still electronically converged  $\{5,5\}$  based structures. That the explanation for this shall not be found in the multiple reflection scheme used to describe the discrepancies of Fig. 7, is seen from the dashed black curve, which represents the reflection from a stack based on layered graphite/bulk hBN just as the black dashed curve of Fig. 7. To confirm the hypothesis that only the topmost sheets contribute to the reflection for large  $k_x$  we plot the averaged reflection coefficient from graphite and bulk hBN of thickness  $420c_0$  (orange dots). The agreement for large  $k_x$  with the reflection from the  $6 \times (35B, 35B)$  stack, shows that indeed only the topmost sheets contribute to the reflection, since the orange dots represents the reflection from a nonlayered bulk structure. They both, however, suffer from similar deficiencies as EMT with incorrect limiting behavior. We calculate instead the averaged reflection coefficient from graphite and bulk hBN, but for the 17 topmost of the 420 sheets we use sheet 1–17 (Gr) or sheet 36–52 (hBN) of a  $\{35,35\}$  calculation (red dotted curve). Doing this, we find exactly the correct limiting behavior, again confirming the hypothesis that only the topmost sheets contribute, but, more importantly, demonstrating the crucial role of effects near the interface in obtaining the correct limiting behavior. We have tested that these results are also valid for other energies within and outside the hyperbolic regime. These findings are well in line with other studies showing the importance of even single

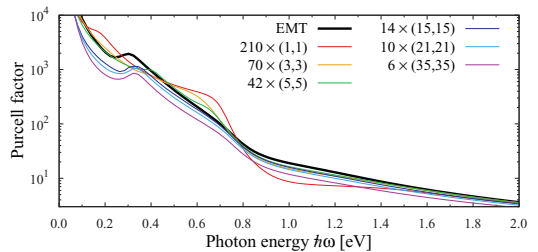


FIG. 11. Purcell factor for a dipole located 20 nm from and oriented parallel to the surface of the HMM. The Fermi level is  $E_F = 0.5$  eV. For the large electronically converged structures shown, EMT overestimates the Purcell factor by up to a factor of 4.

layers [12,13] on transmission and reflection, but our results show also that the often ignored differences in electronic structure arising at an interface may in fact be very important.

For completeness we have included EMTi for the  $42 \times (5,5)$  structure. Improvement over EMT is certainly seen, but we remark that for thick layers EMTi suffers from the same deficiencies as EMT exactly because only the topmost layers, and not the layer interfaces, contribute.

The Purcell factor depends on the reflection coefficient of the structure at large  $k_x$  and we therefore expect deviations from EMT for all structures. In Fig. 11, we present a calculation of the Purcell factor for a dipole-oriented parallel to and located 20 nm from the surface, showing as expected an increase within the hyperbolic region [28,29]. The increase in the Purcell factor depends critically on the damping and on the temperature and due to the relatively high broadening and temperature used in our calculations (50 meV and 25 meV) we do not see enhancements as large as predicted by others [29]. For structures  $210 \times (1,1)$ ,  $70 \times (3,3)$  and  $42 \times (5,5)$  the deviations from EMT are due to nonconverged permittivities, while the deviations observed for the converged structures are due to EMT not predicting correctly the reflection coefficient for high  $k_x$  modes. The important conclusion to be made from our calculations, is the fact that EMT is a rather poor approximation for all structures in the energy range shown, overestimating the Purcell factor by up to a factor of 4 even for the converged structures.

#### IV. CONCLUSION

We have investigated the validity of EMT in the extreme limit of metamaterials constructed from alternating layers of single atomic sheets of graphite and hBN and layers of up to 35 consecutive coupled sheets, and found that already for five sheets both  $\varepsilon_{\parallel}$  and  $\varepsilon_{\perp}$  has converged. For structures in which the Gr part is doped, the convergence is slower. We offer a simple improvement to EMT, which greatly improves the convergence in the spectral range 0 eV to  $3E_F$ . For relatively thick layers of  $\approx 10$  nm (30 sheets) and more, multiple reflections at layer interfaces become important and causes EMT to break down for certain energies. In calculating the reflection of evanescent modes of large  $k_x$ , EMT always fails because only the topmost sheets of the structure contribute and this makes

calculations very sensitive to the electronic details of these sheets. This causes EMT to overestimate the Purcell factor for the converged structures. In fact, we have shown that ignoring the atomistic effects caused by the boundaries of a structure can lead to quite different results. Our findings are important for the numerous works already using EMT and for future works in which EMT is used as a simple tool for providing a quick first estimate of material properties.

#### ACKNOWLEDGMENTS

The authors gratefully acknowledge the financial support from the Center for Nanostructured Graphene (Grant No. DNRF103) financed by the Danish National Research Foundation and from the QUSCOPE project financed by the Villum Foundation.

#### APPENDIX: REFLECTION COEFFICIENTS

In the following we outline the procedure used to determine the Fresnel reflection coefficients between two anisotropic materials characterized by the permittivity tensors

$$\boldsymbol{\epsilon}_1 = \begin{pmatrix} \epsilon_{\parallel,1} & 0 & 0 \\ 0 & \epsilon_{\parallel,1} & 0 \\ 0 & 0 & \epsilon_{\perp,1} \end{pmatrix}, \quad \boldsymbol{\epsilon}_2 = \begin{pmatrix} \epsilon_{\parallel,2} & 0 & 0 \\ 0 & \epsilon_{\parallel,2} & 0 \\ 0 & 0 & \epsilon_{\perp,2} \end{pmatrix}. \quad (\text{A1})$$

The starting point is the wave equation in anisotropic media

$$\nabla^2 \boldsymbol{\mathcal{E}} + k_0^2 \boldsymbol{\epsilon} \cdot \boldsymbol{\mathcal{E}} - \nabla(\nabla \cdot \boldsymbol{\mathcal{E}}) = 0, \quad (\text{A2})$$

where  $\boldsymbol{\mathcal{E}}$  is of the form Eq. (A1),  $\boldsymbol{\mathcal{E}}$  is the electric field and  $k_0 = \omega/c$ . Assuming plane-wave solutions of the form  $\boldsymbol{\mathcal{E}}(\mathbf{r}) = \boldsymbol{\mathcal{E}}_0 e^{i\mathbf{k} \cdot \mathbf{r}}$  the wave equation takes the form

$$-k^2 \boldsymbol{\mathcal{E}}_0 + k_0^2 \boldsymbol{\epsilon} \cdot \boldsymbol{\mathcal{E}}_0 + \mathbf{k}(\mathbf{k} \cdot \boldsymbol{\mathcal{E}}_0) = 0. \quad (\text{A3})$$

For  $s$  polarization the reflection coefficients are the same as in the isotropic case with permittivity  $\epsilon_{\parallel}$ . For  $p$  polarization the procedure is (i) determine the field directions in the anisotropic materials; (ii) express the incident, reflected and transmitted fields; and (iii) use the electromagnetic boundary conditions to determine the reflection/transmission coefficients. For  $p$

polarization we use a result from Refs. [30,31] giving the non-normalized direction vector of the electric field inside an anisotropic material characterized by  $\epsilon_{\parallel}$  and  $\epsilon_{\perp}$  as

$$\mathbf{q}_{\pm} = \frac{n^p}{k_0} \left[ \frac{k_x}{\epsilon_{\perp}} \hat{\mathbf{z}} \mp \frac{k_z^p}{\epsilon_{\parallel}} \hat{\mathbf{x}} \right], \quad (\text{A4})$$

where  $n^p$  is the effective index of refraction defined by

$$n^p = \frac{|k_{\pm}^p|}{k_0} = \sqrt{\epsilon_{\parallel} + \left(1 - \frac{\epsilon_{\parallel}}{\epsilon_{\perp}}\right) \frac{k_x^2}{k_0^2}}, \quad (\text{A5})$$

with  $k_{\pm}^p = k_x \hat{\mathbf{x}} \pm k_z^p \hat{\mathbf{z}}$  and  $k_z^p = \sqrt{k_0^2 \epsilon_{\parallel} - (\epsilon_{\parallel}/\epsilon_{\perp}) k_x^2}$ . We notice that the effective refractive index reduces to the in-plane refractive index  $\sqrt{\epsilon_{\parallel}}$  in the isotropic case and when  $k_x = 0$ , corresponding to  $s$ -polarized light.

We can now formulate expressions for the incident, reflected, and transmitted fields in the two anisotropic materials. We assume light to be incident from material 1 and transmitted into material 2, thus

$$\boldsymbol{\mathcal{E}}_i = \mathcal{E}_0 \mathbf{q}_{-,1} e^{i\mathbf{k}_{-,1}^p \cdot \mathbf{r}}, \quad \boldsymbol{\mathcal{B}}_i = \frac{\mathcal{E}_0}{ck_0} n_1^p \hat{\mathbf{y}} e^{i\mathbf{k}_{-,1}^p \cdot \mathbf{r}}, \quad (\text{A6})$$

$$\boldsymbol{\mathcal{E}}_r = r \mathcal{E}_0 \mathbf{q}_{+,1} e^{i\mathbf{k}_{+,1}^p \cdot \mathbf{r}}, \quad \boldsymbol{\mathcal{B}}_r = r \frac{\mathcal{E}_0}{ck_0} n_1^p \hat{\mathbf{y}} e^{i\mathbf{k}_{+,1}^p \cdot \mathbf{r}}, \quad (\text{A7})$$

$$\boldsymbol{\mathcal{E}}_t = t \mathcal{E}_0 \mathbf{q}_{-,2} e^{i\mathbf{k}_{-,2}^p \cdot \mathbf{r}}, \quad \boldsymbol{\mathcal{B}}_t = t \frac{\mathcal{E}_0}{ck_0} n_2^p \hat{\mathbf{y}} e^{i\mathbf{k}_{-,2}^p \cdot \mathbf{r}}. \quad (\text{A8})$$

From the electromagnetic boundary conditions ( $\mathcal{E}_{\parallel,1} = \mathcal{E}_{\parallel,2}$  and  $\mathcal{B}_{\parallel,1} = \mathcal{B}_{\parallel,2}$  at the interface  $z=0$ ) we obtain the Fresnel reflection and transmission coefficients between two anisotropic materials as

$$r_p = \frac{\epsilon_{\parallel,2} k_{z,1}^p - \epsilon_{\parallel,1} k_{z,2}^p}{\epsilon_{\parallel,2} k_{z,1}^p + \epsilon_{\parallel,1} k_{z,2}^p}, \quad (\text{A9})$$

$$t_p = \frac{2\epsilon_{\parallel,2} k_{z,1}^p n_1^p / n_2^p}{\epsilon_{\parallel,2} k_{z,1}^p + \epsilon_{\parallel,1} k_{z,2}^p}. \quad (\text{A10})$$

The expression for  $t_p$  reduces to Eq. (17) in Ref. [30] in the special isotropic case  $\epsilon_{\parallel,1} = \epsilon_{\perp,1} = 1$ .

- 
- [1] Z. Liu, H. Lee, Y. Xiong, C. Sun, and X. Zhang, Far-field optical hyperlens magnifying sub-diffraction-limited objects, *Science* **315**, 1686 (2007).
- [2] M. Noginov, H. Li, Y. A. Barnakov, D. Dryden, G. Nataraj, G. Zhu, C. Bonner, M. Mayy, Z. Jacob, and E. Narimanov, Controlling spontaneous emission with metamaterials, *Opt. Lett.* **35**, 1863 (2010).
- [3] P. Shekhar, J. Atkinson, and Z. Jacob, Hyperbolic metamaterials: fundamentals and applications, *Nano Converg.* **1**, 1 (2014).
- [4] A. Poddubny, I. Iorsh, P. Belov, and Y. Kivshar, Hyperbolic metamaterials, *Nat. Photon.* **7**, 948 (2013).
- [5] K. Sreekanth, T. Biaglow, and G. Strangi, Directional spontaneous emission enhancement in hyperbolic metamaterials, *J. Appl. Phys.* **114**, 134306 (2013).
- [6] M. A. Othman, C. Guclu, and F. Capolino, Graphene-based tunable hyperbolic metamaterials and enhanced near-field absorption, *Opt. Express* **21**, 7614 (2013).
- [7] A. Andryieuski, A. V. Lavrinenko, and D. N. Chigrin, Graphene hyperlens for terahertz radiation, *Phys. Rev. B* **86**, 121108 (2012).
- [8] K. Sreekanth, A. De Luca, and G. Strangi, Negative refraction in graphene-based hyperbolic metamaterials, *Appl. Phys. Lett.* **103**, 023107 (2013).
- [9] L. Zhang, Z. Zhang, C. Kang, B. Cheng, L. Chen, X. Yang, J. Wang, W. Li, and B. Wang, Tunable bulk polaritons of graphene-based hyperbolic metamaterials, *Opt. Express* **22**, 14022 (2014).
- [10] R. Ning, S. Liu, H. Zhang, B. Bian, and X. Kong, A wide-angle broadband absorber in graphene-based hyperbolic metamaterials, *Eur. Phys. J. Appl. Phys.* **68**, 20401 (2014).

- [11] T. Tumkur, Y. Barnakov, S. Kee, M. Noginov, and V. Liberman, Permittivity evaluation of multilayered hyperbolic metamaterials: Ellipsometry vs. reflectometry, *J. Appl. Phys.* **117**, 103104 (2015).
- [12] O. Kidwai, S. V. Zhukovsky, and J. Sipe, Effective-medium approach to planar multilayer hyperbolic metamaterials: Strengths and limitations, *Phys. Rev. A* **85**, 053842 (2012).
- [13] H. H. Sheinfux, I. Kaminer, Y. Plotnik, G. Bartal, and M. Segev, Subwavelength Multilayer Dielectrics: Ultrasensitive Transmission and Breakdown of Effective-Medium Theory, *Phys. Rev. Lett.* **113**, 243901 (2014).
- [14] J. Sławińska, I. Zasada, and Z. Klusek, Energy gap tuning in graphene on hexagonal boron nitride bilayer system, *Phys. Rev. B* **81**, 155433 (2010).
- [15] E. Taft and H. Philipp, Optical properties of graphite, *Phys. Rev.* **138**, A197 (1965).
- [16] A. Grüneis, C. Attacalite, L. Wirtz, H. Shiozawa, R. Saito, T. Pichler, and A. Rubio, Tight-binding description of the quasiparticle dispersion of graphite and few-layer graphene, *Phys. Rev. B* **78**, 205425 (2008).
- [17] J. J. Mortensen, L. B. Hansen, and K. W. Jacobsen, Real-space grid implementation of the projector augmented wave method, *Phys. Rev. B* **71**, 035109 (2005).
- [18] W. Kohn and L. J. Sham, Self-consistent equations including exchange and correlation effects, *Phys. Rev.* **140**, A1133 (1965).
- [19] J. Yan, J. J. Mortensen, K. W. Jacobsen, and K. S. Thygesen, Linear density response function in the projector augmented wave method: Applications to solids, surfaces, and interfaces, *Phys. Rev. B* **83**, 245122 (2011).
- [20] A. MacDonald, S. Vosko, and P. Coleridge, Extensions of the tetrahedron method for evaluating spectral properties of solids, *J. Phys. C: Solid State* **12**, 2991 (1979).
- [21] W. Paszkowicz, J. Pelka, M. Knapp, T. Szyszko, and S. Podsiadlo, Lattice parameters and anisotropic thermal expansion of hexagonal boron nitride in the 10–297.5 k temperature range, *Appl. Phys. A* **75**, 431 (2002).
- [22] G. Constantinescu, A. Kuc, and T. Heine, Stacking in Bulk and Bilayer Hexagonal Boron Nitride, *Phys. Rev. Lett.* **111**, 036104 (2013).
- [23] B. Sachs, T. Wehling, M. Katsnelson, and A. Lichtenstein, Adhesion and electronic structure of graphene on hexagonal boron nitride substrates, *Phys. Rev. B* **84**, 195414 (2011).
- [24] T. G. Pedersen, C. Flindt, J. Pedersen, A.-P. Jauho, N. A. Mortensen, and K. Pedersen, Optical properties of graphene antidot lattices, *Phys. Rev. B* **77**, 245431 (2008).
- [25] T. G. Pedersen, Analytic calculation of the optical properties of graphite, *Phys. Rev. B* **67**, 113106 (2003).
- [26] L. G. Johnson and G. Dresselhaus, Optical properties of graphite, *Phys. Rev. B* **7**, 2275 (1973).
- [27] G. E. Jellison Jr, J. D. Hunn, and H. N. Lee, Measurement of optical functions of highly oriented pyrolytic graphite in the visible, *Phys. Rev. B* **76**, 085125 (2007).
- [28] A. M. DaSilva, Y.-C. Chang, T. Norris, and A. H. MacDonald, Enhancement of photonic density of states in finite graphene multilayers, *Phys. Rev. B* **88**, 195411 (2013).
- [29] I. V. Iorsh, I. S. Mukhin, I. V. Shadrivov, P. A. Belov, and Y. S. Kivshar, Hyperbolic metamaterials based on multilayer graphene structures, *Phys. Rev. B* **87**, 075416 (2013).
- [30] R. J. Gehr, G. L. Fischer, R. W. Boyd, and J. Sipe, Nonlinear optical response of layered composite materials, *Phys. Rev. A* **53**, 2792 (1996).
- [31] J. J. Saarinen and J. Sipe, A green function approach to surface optics in anisotropic media, *J. Mod. Opt.* **55**, 13 (2008).

## 5.2 Paper II: Band structure engineered layered metals for low-loss plasmonics

The paper is submitted.

# Band structure engineered layered metals for low-loss plasmonics

Morten N. Gjerding and Kristian S. Thygesen\*

*Center for Atomic-scale Materials Design (CAMD) and Center for Nanostructured Graphene (CNG),  
Department of Physics, Technical University of Denmark,  
Anker Engelundsvej 1, 2800, Kgs. Lyngby, Denmark*

Mohnish Pandey

*Center for Atomic-scale Materials Design (CAMD),  
Department of Physics, Technical University of Denmark,  
Anker Engelundsvej 1, 2800, Kgs. Lyngby, Denmark*

(Dated: December 21, 2016)

Plasmonics currently faces the problem of seemingly inevitable optical losses occurring in the metallic components that challenges the implementation of essentially any application. In this work we show that Ohmic losses are reduced in certain layered metals, such as the transition metal dichalcogenide TaS<sub>2</sub>, due to an extraordinarily small density of states for scattering in the near-IR originating from their special electronic band structure. Based on this observation we propose a new class of band structure engineered van der Waals layered metals composed of hexagonal transition metal chalcogenide-halide layers with greatly suppressed intrinsic losses. Using first-principles calculations we show that the suppression of optical losses lead to improved performance for thin film waveguiding and transformation optics.

## INTRODUCTION

The basic idea of plasmonics is to utilise the sub wavelength confinement of light on metallic surfaces in the form of plasmon-polaritons to enable a range of applications including negative index materials[1], imaging[2–4], energy conversion[5, 6], quantum information processing[7] and transformation optics[8, 9]. However, in practice many of these applications are challenged by optical losses occurring in the metallic components [10–12]. So far, no viable alternatives to the noble metals have been found and the detrimental losses have appeared to be an unavoidable property of any conducting material.

Optical losses in metals originate from electronic transitions between the occupied and unoccupied parts of the crystal band structure, see Figure 1. In the absence of any scattering mechanisms, absorption of photons can take place only via vertical transitions in the Brillouin zone due to the small momentum of the photon, cf. transition (iii). However, scattering on crystal imperfections, phonons or other electrons, can provide the extra momentum required for light absorption via non-vertical electronic transitions, cf. transitions (i) and (ii). Typically, losses increase significantly above the onset of interband transitions which sets a hard upper limit on the operating frequencies of a plasmonic material. The effect of intra-band scattering (transition (ii)) on the optical properties of metals is often accounted for by a phenomenological relaxation time. As we show here, a key to describe and discover intrinsic low-loss metals is to move beyond the commonly used constant relaxation time approximation and include band structure effects in the scattering rate.

Previous searches for new plasmonic materials in

the optical regime have explored the alkali-noble intermetallics[13, 14] and transition metal nitrides[15]. Some materials showed promise although their performance was still lower than that of the noble metals. Because all optical losses ultimately depend on the existence of an initial occupied and final unoccupied electronic state, one strategy for reducing losses has been to reduce the number of states available for scattering. Following this principle, doped semiconductors and transparent conducting oxides have been proposed for applications in the mid and near-infrared, respectively[16]. Recently, graphene plasmonics has been extensively studied due to its low density of states around the Dirac cone and easily tuneable plasma frequency[17, 18].

The ‘elusive loss-less metal’[19] represents the ideal plasmonic material where no states are available for scattering in a particular frequency range thus eliminating optical losses completely, cf. transition (iv) in Figure 1. Such a metal is obtained when the metallic, i.e. partially filled, band(s) are separated from all higher and lower lying bands by sufficiently large energy gaps. Metals with such isolated intermediate bands are very rare among the conventional bulk materials. On the other hand, low-dimensional materials, in particular layered materials, with a significant fraction of under-coordinated atoms and thus overall weaker hybridization, might be more likely to exhibit such characteristic band structures.

In this paper we test this hypothesis by examining the computed band structures of the metallic layered materials identified in Ref. [20]. We discover that the transition metal dichalcogenides (TMDs) TaS<sub>2</sub> and NbS<sub>2</sub> as well as aluminum(II) chloride, AlCl<sub>2</sub>, have monolayer band structures that resemble that of the ‘elusive loss-less metal’, and confirm by first-principles calculations that the special electronic structure does entail lowered

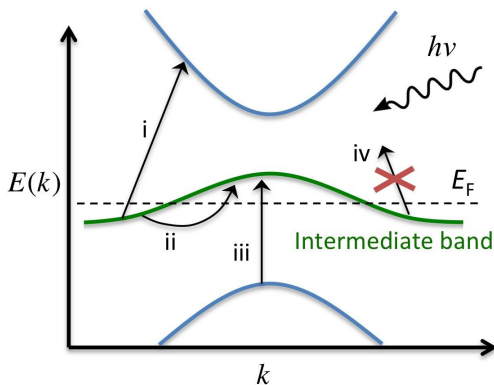


FIG. 1. **Origin of optical losses in metals.** The optical loss in metals originate from electronic transitions from occupied to unoccupied states in the crystal band structure (i, ii, iii). Only vertical transitions (iii) are allowed if scattering mechanisms are disregarded. Scattering mechanisms (impurity scattering, phonon absorption and emission, electron-electron scattering) can give the momentum required to allow for indirect transitions (i, ii). A metal with an intermediate band separated by gaps will suppress the number of transitions available (direct and indirect) at specific frequencies like in (iv) where no unoccupied state exists. When the gaps are sufficiently large to separate intraband(i) from interband(ii, iii) losses, some spectral ranges become immune to all quasi-elastic loss mechanisms.

optical losses. The constant relaxation time approximation is shown to be insufficient for describing the optical permittivity of these materials and we propose a simple model of the scattering rate based on the joint density of states to remedy this deficiency. Based on the promising results obtained for the TMDs we propose a new class of bandstructure engineered layered materials composed of transition metal chalcogenide-halide layers that greatly suppress the optical losses, and demonstrate the improved performance of these materials for thin film waveguiding and transformation optics.

## RESULTS

**Identifying low loss layered metals.** Examining the computed band structures of the metallic layered materials identified in Ref. [20] by data filtering the Inorganic Crystal Structure Database (ICSD, Sec. S1) reveal that the transition metal dichalcogenides (TMDs) 2H-TaS<sub>2</sub> and 2H-NbS<sub>2</sub> as well as aluminum(II) chloride, AlCl<sub>2</sub>, have monolayer band structures that resemble that of the 'elusive loss-less metal'. While 2H-TaS<sub>2</sub> and 3R-NbS<sub>2</sub> have been synthesized in bulk form, AlCl<sub>2</sub> was derived from the experimentally known AlCl<sub>3</sub> by removing an interstitial Cl layer.

Figure 2 shows the atomic structures, band structures, and density of states (DOS) for (a) 2H-TaS<sub>2</sub>, (b) 3R-NbS<sub>2</sub>, and (c) 1T-AlCl<sub>2</sub>. The band structures of the monolayers are shown (red) although we will focus on the bulk structures throughout this work. In the case of 2H-TaS<sub>2</sub> and 3R-NbS<sub>2</sub> the formation of the bulk from the monolayer breaks the degeneracy of the highest valence band at the  $\Gamma$  point and closes the gap to the metallic band, but the DOS above and below the intermediate band remains fairly low. Inter-layer hybridization plays a smaller role for 1T-AlCl<sub>2</sub>; in particular, the band gaps are present for both the monolayer and bulk. The metallic band in AlCl<sub>2</sub> is formed by the Al *s*-states, and the small band width of 1 eV is a consequence of the weak hybridization between the Al atoms within the same atomic plane with the Cl atoms acting mainly as spacers. We stress that AlCl<sub>2</sub> is thermodynamically unstable. Although its calculated heat of formation is negative (-0.89 eV/atom) relative to the standard states of Al and Cl, it lies 0.7 eV above the 'convex hull' when considering other competing phases (see Methods). In contrast, the layered compound AlCl<sub>3</sub> is stable and has been experimentally synthesised. Starting from AlCl<sub>3</sub> it may be feasible to remove the loosely bound Cl interstitial layer and thereby form metastable AlCl<sub>2</sub>.

We verify that the gapped metallic band structures entail lowered optical losses by performing first-principles calculations to obtain the dielectric function of AlCl<sub>2</sub> with an Al vacancy introduced in a 3x3x2 supercell. The introduction of a vacancy is necessary to probe the optical losses due to intraband transitions where the defect provides the required momentum, see Figure 1, transition ii. (Qualitatively similar results would be expected from phonon or electron scattering, however, such processes are more complicated to describe from first principles.) For comparison, a similar calculation was performed for a 3x3x3 supercell of Ag with a single vacancy (see Methods). Figure 3 (full lines) shows the imaginary part of the dielectric function which is directly related to the optical losses of the metal. Optical losses at low frequencies due to the intraband transitions are indeed observed.

The dielectric function of a metal can be divided into contributions from interband and intraband transitions, respectively. It is customary to approximate the latter by a Drude response:

$$\varepsilon(\omega) = \varepsilon_{\text{inter}}(\omega) + \varepsilon_{\text{Drude}}(\omega), \quad (1)$$

$$\varepsilon_{\text{Drude}} = 1 - \frac{\omega_p^2}{\omega^2 - i\omega\eta}, \quad (2)$$

where  $\omega_p$  is the plasma frequency and  $\eta$  is the constant relaxation rate of the free carriers. In Figure 3 we show the result of the Drude model (thick grey lines) with  $\eta$  fitted to obtain the best correspondence with the first-principles results using the bulk plasma frequency for  $\omega_p$ . Excellent agreement is found for silver all the way

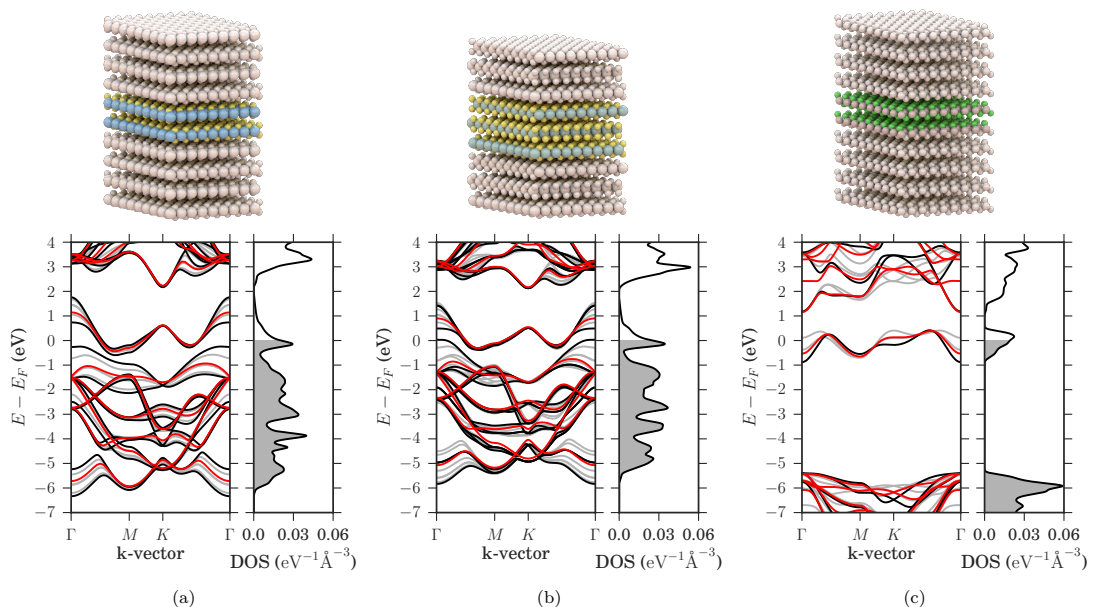


FIG. 2. **Band structures of vdW-metals.** (a) 2H(AA')-TaS<sub>2</sub>, (b) 3R-NbS<sub>2</sub> have and (c) 1T-AlCl<sub>2</sub> exhibit special band structures where the metallic band is separated from higher and lower lying bands by finite energy gaps. Such band structures entail a strongly reduced number of states available for scattering as depicted in Fig. 1. Comparing the monolayer band structures (red lines) with the bulk band structures (black) reveal that inter layer hybridization break the valence band degeneracy at the  $\Gamma$  point for 2H-TaS<sub>2</sub> and 3R-NbS<sub>2</sub> and closes the gap below the Fermi level. The interlayer hybridization is non-essential for 1T-AlCl<sub>2</sub>. The dispersion in the out-of-plane direction does not effect the existence of an intermediate band as evidenced by the grey lines showing band structures at band paths translated in the out of plane direction.

up to the onset of inter-band transitions demonstrating the validity of the constant relaxation time approximation for this material. In contrast, it is not possible to fit the dielectric function of AlCl<sub>2</sub> by the simple Drude model below the onset of interband transitions at 1.5 eV. This is a result of the special band structure of AlCl<sub>2</sub> which introduces a strong energy dependence of the joint density of states (JDOS). The JDOS gives the density of electron-hole pairs at a given frequency (disregarding momentum conservation) and thus represents the density of final states entering the expression for the scattering rate. In particular, the Drude model is not able to capture the strong reduction of the losses in the range 1-1.5 eV. In this energy range there are essentially no states available for scattering because of (i) the finite band width of the partially filled metallic band and (ii) the presence of band gaps separating the metallic band from the rest of the bands. Consequently, the JDOS will vanish at energies above the intraband transitions and below the onset of inter band transitions. In the case of AlCl<sub>2</sub>, the band gaps are not large enough to completely separate the interband transitions from the intraband transitions, and consequently neither the JDOS nor  $\text{Im}\epsilon$  become exactly

zero. However, the JDOS is strongly suppressed in the range 1-1.5 eV and this is the origin of the low-loss nature of AlCl<sub>2</sub>.

**Relaxation rate model.** A more realistic description of the relaxation rate should include information about the number of available electron-hole transitions, i.e. the JDOS. A simple way to incorporate such a dependence is via

$$\eta(\omega) = a \frac{\text{JDOS}(\omega)}{\omega} \quad (3)$$

where  $a$  is a constant controlling the scattering strength. The expression can be motivated in different ways, but here it suffices to observe that (i) it reduces to the constant relaxation time approximation for a metal with a constant DOS in a region around Fermi energy (in which case the  $\text{JDOS} \propto \omega$ ) and (ii) it correctly leads to a vanishing relaxation rate for energies where there are no final states for the scattering. As can be seen from Figure 3 (dashed lines) the model provides an excellent description of the optical losses of both materials. In the rest of the paper we use Eq. (3) to include scattering effects in a generic way setting the constant  $a$  to the same value for all materials. This value is chosen to reproduce the

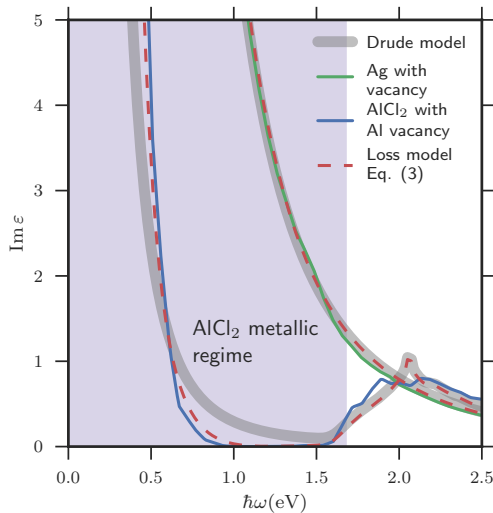


FIG. 3. **Defect induced optical losses and energy-dependent relaxation time model.** The calculated optical losses ( $\text{Im}\epsilon$ ) for silver (green) and  $\text{AlCl}_2$  (blue) with a vacancy defect. The thick grey line shows the standard Drude expression (2) with a constant relaxation time,  $\tau = \hbar/\eta$ , fitted to the ab-initio results. For silver this provides an accurate description of the low-frequency (intraband) losses while the description is less accurate for  $\text{AlCl}_2$  where it misses the strong suppression of losses in the 1-1.5 eV range. Results of the Drude expression with the energy-dependent relaxation rate model (3) (dashed lines) are in excellent agreement with the ab-initio results for both systems.

experimental line width of the Ag surface plasmon (see Figure 4c).

We note that the JDOS model only accounts for first-order (quasi-)elastic scattering processes. Higher-order processes involving generation of several phonons or electron-hole pairs in one coherent photon-mediated event, could lead to absorption (loss) at energies between the intraband and interband transitions where the JDOS model would otherwise predict  $\text{Im}\epsilon$  to vanish. We expect losses due to higher-order processes to be small in the near-IR and therefore neglect them in the following.

The potential of the vdW metals has been evaluated for two different plasmonic applications: Plasmonic waveguiding and transformation optics[22] discussed in detail below. The calculated dielectric functions, DOS, JDOS and relaxation rate  $\eta$  for all the layered metals studied in this work are provided in Sec. S9.

**Plasmonic waveguiding.** Plasmonic waveguides are envisioned as faster and less power consuming alternatives to the electronic interconnects currently used in integrated circuits. Essential prerequisites for such applications are long plasmon lifetimes and propagation lengths

as well as tight spatial confinement of the plasmon to interface efficiently with the nanometer scale electronic components[23]. To evaluate the potential of the layered metals for such applications we investigate plasmon propagation in 5 nm thin-film waveguides and single interface waveguides, respectively, see Figure 4(a+e).  $\text{SiO}_2$  was used as the surrounding dielectric with a dielectric constant of  $\epsilon = 2.1$  ( $\lambda \sim 700$  nm).

Figure 4 shows the normalized propagation length,  $\text{Re}(k_p)/\text{Im}(k_p)$ , where  $k_p$  is the plasmon wave vector (b+c), the plasmon lifetime (c+g) and the mode extension into the dielectric (d+h), for silver, 2H-TaS<sub>2</sub>, 1T- $\text{AlCl}_2$ , and the chalcogenide HfBrS, to be discussed later. The plasmon lifetime,  $\tau$ , is calculated from the relationship  $L = v_p\tau$  where  $v_p$  is the plasmon velocity (see Methods for details). The scattering strength (a) determining the frequency-dependent relaxation rate in Eq. (3) has been fixed by fitting the experimental result for the lifetime of the Ag surface plasmon.

For the thin film waveguide, only the symmetric plasmon mode was considered. The light-like anti-symmetric mode extends far into the dielectric with mode widths on the order of 1 micron in which case the requirement of small coupling to the environment is not fulfilled. For the single interface plasmonic waveguide silver shows significantly longer propagation lengths and lifetimes than any of the vdW metals. This is caused by the more efficient dielectric screening of Ag compared to the vdW metals, which implies that only a tiny fraction of the electromagnetic energy is contained within the silver surface, see Sup. mat. Fig. S1(a). The downside of the strong screening is the accompanying large mode widths caused by the electric field being pushed into the dielectric.

As the thickness of the thin-film plasmonic waveguide is reduced a larger fraction of the electric field is contained in the metal (Sup. mat. Fig. S1(b)) resulting in generally larger losses and decreasing plasmon group velocities[24]. Together these two effects combine to give superior propagation lengths, lifetimes and mode widths for the layered metals. The dependence of the plasmon lifetime on the intrinsic optical losses and the electric field distribution inside the metal is

$$\tau^{-1} \propto \int d\mathbf{r} |E_0(\mathbf{r})|^2 \text{Im}\epsilon. \quad (4)$$

From this it is clear that the relatively better performance of the layered metals in thin film waveguides as compared to Ag must be due to lower intrinsic losses because the electric field fraction within the vdW metal is much larger than in silver (Sup. mat. Fig. S1(b)).

It is well known that the PBE exchange-correlation (xc) functional underestimates both band gaps of semiconductors and interband transition energies in metals[25]. To test the influence of the xc-functional we have computed the dielectric function of 2H-TaS<sub>2</sub> using the range separated hybrid functional (HSE06) which

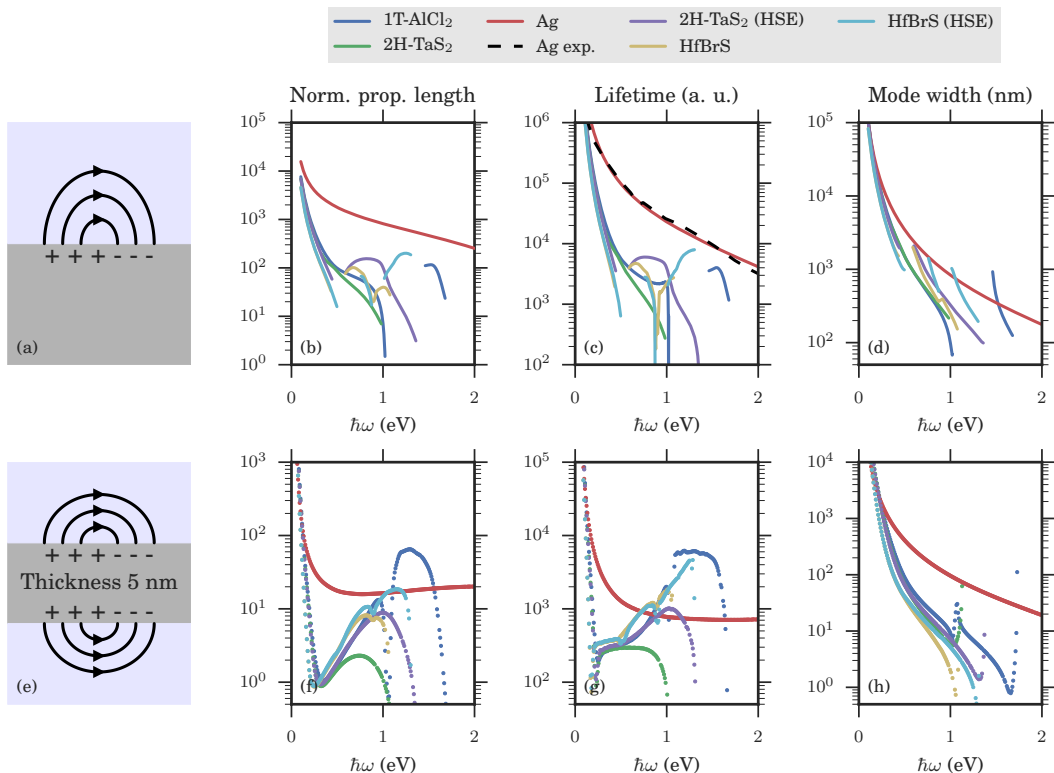


FIG. 4. **Plasmon waveguiding figures of merit.** The upper panels show the normalized plasmon propagation lengths  $\text{Re}(k_p)/\text{Im}(k_p)$  (b), lifetimes (c) and mode width (d) for a plasmon on a single interface. The lower panels show the same results for a 5 nm thin film. The more efficient dielectric screening in silver reduces the fraction of the electric field located within the metal as compared to the case of the vdWH metals, resulting in lower losses, longer propagation lengths and lifetimes. On the other hand, since most of the electromagnetic energy is stored in the part of the electric field distributed over the dielectric, the mode widths of the surface plasmon becomes relatively large. Reducing the thickness of the metal to a 5 nm thin film pushes a larger fraction of the electric field into the metal leading to more confined modes. The redistribution of the electric field from dielectric to metal is more significant for silver explaining the overall better performance of the vdWH metals for the thin film geometry. Experimental data for the Ag surface plasmon was adapted from Ref. [21]

generally yield more reliable band energies[26]. The primary effect of the HSE is to increase the size of the two gaps around the intermediate metallic band by around 0.5 eV (see Fig. S11) compared to PBE. This blue shifts the onset of interband transitions resulting in a significantly larger plasma frequency and lower losses. Consequently, the calculated plasmon propagation lengths and lifetimes becomes comparable to the noble metals while maintaining a small mode width (Fig. 4(f-h)).

**Band structure engineered layered metals.** With the goal of identifying new materials with band structures similar to those of 2H-TaS<sub>2</sub> and 2H-NbS<sub>2</sub>, we have considered the class of layered materials of the form 2H-MXY (Fig. 5(a)), where M is a group 3 transition metal

(Ti,Zr,Hf), X is oxygen or a chalcogen (O,S,Se) and Y is a halogen (Cl,Br,I). While conserving the total electron number, the lower electronegativity of the group 3 compared to group 4 transition metals and the higher electronegativity of the halides compared to chalcogens, should increase the gap between the bands below and above the intermediate metallic band, which are composed mainly of chalcogen *p* and metal *d*, respectively. This should blue shift the interband transitions and decrease optical losses.

The calculated formation energies of the MXY compounds range from -2.53 eV to -0.92 eV per atom relative to the standard states. To check thermodynamic stability against other competing phases we compare the forma-

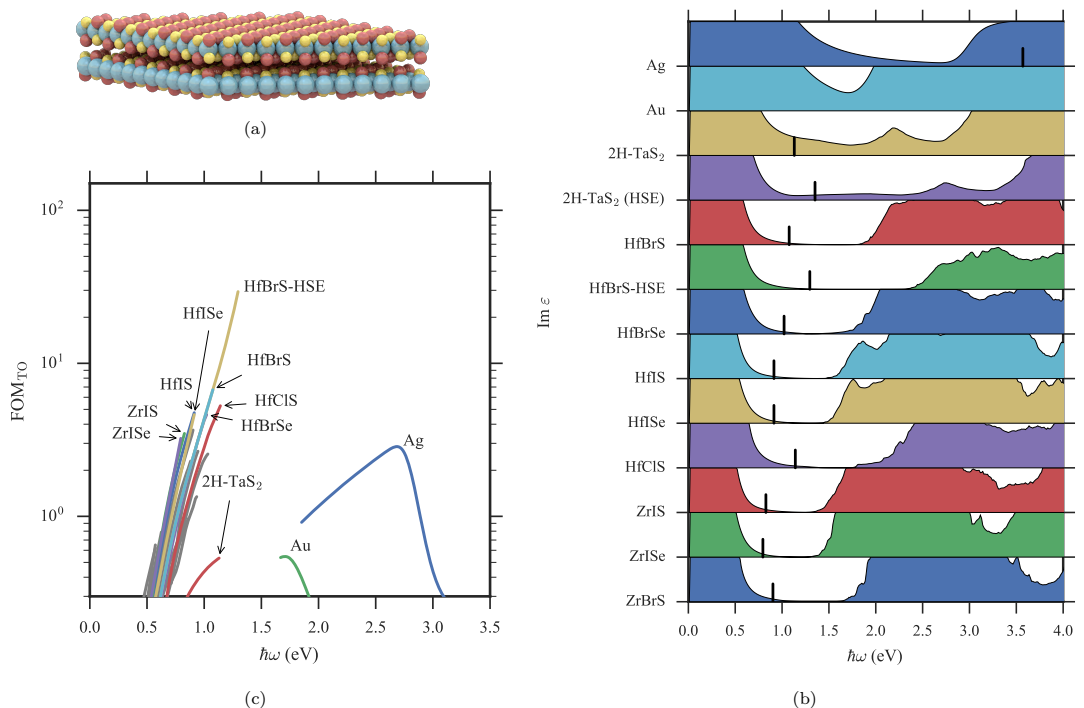


FIG. 5. **Optical properties of layer transition metal chalcogen-halogens.** Layered materials of the form 2H-MXY (a) where M is a group 3 transition metal, X is oxygen or a chalcogen (S, Se) and Y is a halogen (Cl, Br, I) are proposed as new plasmonic metals. The optical losses (b) shows that many of these compounds have considerable spectral ranges of low optical losses both compared to silver and to 2H-TaS<sub>2</sub> (the losses are normalized so that they can be directly compared between different materials). This is due to the decreased electronegativity of (Hf, Zr, Ti) compared to Ta which increases the gap below the Fermi level. As a result, the predicted FOM (c) is orders of magnitude better than silver in the near infrared.

tion energies to the convex hull, see Figure S5. Out of the 27 compounds, 19 are found to be stable while the rest are only weakly unstable with formation energies lying less than 50 meV above the convex hull. The structural stability of the chalo-halides was checked by performing relaxations of the monolayers in supercells containing 2 primitive cells (containing 12 atoms). With initial random distortions, the atoms relaxed back to restore the symmetry of the hexagonal lattice indicating that the structures are at least locally stable. The DFT calculations were performed fully spin polarised, but all the materials converged to a non-magnetic ground state.

The calculated  $\text{Im } \epsilon$  are presented in Figure 5(b), and are characterized by significantly lower optical losses in the NIR regime 1-1.5 eV; a direct signature of the reduction in the density of states for scattering (Fig. S2). Figure 4 shows that the lowered optical losses entail an improved plasmon propagation length and lifetime as compared to 2H-TaS<sub>2</sub> for one of the compounds that exhibit the lowest optical losses, 2H-HfBrS, in both the

single interface and thin-film geometries. As we found for 2H-TaS<sub>2</sub>, the HSE functional increases the band gaps of the MXY compounds by approximately 0.5 eV which reduces the losses even further and increases the plasma-frequencies, as illustrated for HfBrS (Fig. 5(b)). In the thin-film geometry this results in significantly improved plasmon lifetimes as compared to silver in the technologically important NIR frequency range (Fig. 4(g)) while maintaining a small mode volume (Fig. 4(h)).

**Transformation optics.** We now turn to an assessment of the potential of the layered metals for transformation optics (TO). Here the goal is to engineer the propagation of a wavefront through the volume of a metamaterial[22] for various applications. For a metamaterial structure containing metal-dielectric interfaces it is required that the metallic response ( $\text{Re } \epsilon_M$ ) is compensated by the dielectric response ( $\text{Re } \epsilon_D$ ) while losses remaining low. Consequently, the typical figure of merit for TO applications is  $\text{FOM}_{\text{TO}} = 1/\text{Im } \epsilon_M$  while  $-\text{Re } \epsilon_M \approx \text{Re } \epsilon_D$ [22]. Assuming that the metallic response can al-

ways be matched by a dielectric within the range  $1 < \text{Re}\epsilon_D < 20$ , the relevant FOM becomes

$$\text{FOM}_{\text{TO}} = \frac{1}{\text{Im}\epsilon_M} \theta(-\text{Re}\epsilon_M) \theta(\text{Re}\epsilon_M + 20) \quad (5)$$

where  $\theta(x)$  is the Heaviside step function. Figure 5(c) shows the calculated FOM for the MXY-compounds and the best of the 18 metallic TMDs identified in Ref. [20] (see Sec. S1 for the full list of materials). Reassuringly the best TMD turns out to be 2H-TaS<sub>2</sub> which is one of the metals with an intermediate metallic band. In general, the losses in the TMDs increase from sulphides to selenides to tellurides due to a lowering of the onset of interband transition. A similar trend is known for the semi-conducting TMDs where the band gaps decrease when progressing through the chalcogenide group towards higher atomic number[27]. All the MXY compounds outperform both 2H-TaS<sub>2</sub> and the noble metals in the technologically important near-infrared frequency range. The improved performance is attributed to the larger gaps surrounding the intermediate metallic band which increases the plasma frequency and extends the loss-less regime between the intraband and interband transitions, see Figure 5(b).

**Loss-less layered halides.** Motivated by the excellent plasmonic properties of the (thermodynamically unstable) 1T-AlCl<sub>2</sub>, we have performed a systematic study of layered bulk halides of the form (1T, 2H)-AY<sub>2</sub> where  $A$  is a group 3-13 element and  $Y$  is a halogen (Cl, Br or I). After filtering out materials with positive formation energies and finite magnetic moments and examining the band structures of the remaining materials we identify several candidates with close to perfect resemblance with the 'elusive loss-less material'. For example, 1T-GaCl<sub>2</sub> (see Fig. S8) has an isolated intermediate metallic band of width 1.0 eV, and an interband edge of 2.6 eV, a plasma frequency of 1.4 eV (Fig. S9). As a result the calculated plasmon propagation length and  $\text{FOM}_{\text{TO}}$  are essentially infinite (Fig. S10). Unfortunately, these halides are unlikely to be thermodynamically stable when considering other competing phases, although we have not explored this systematically. Nevertheless, we find it interesting that these metastable structures exhibit such extreme properties.

## DISCUSSION

A critical issue for the layered metals considered in this work is stability. Even though most of the chalcogenides were found to be thermodynamically stable relative to other competing phases involving the same elements, the materials could oxidize and disintegrate when exposed to air or moisture. Whether this will happen is largely a matter of kinetics and a theoretical assessment requires calculation of reaction barriers which is beyond

the present study. However, we note that encapsulation could be a way to protect the materials from reacting with other species. For example, it was recently demonstrated that encapsulation in hexagonal boron-nitride can protect and stabilize phosphorene in air, which in its free form is highly unstable and oxidizes quickly ([28]). Airtight encapsulation of sensitive materials are routinely used in other fields such as organic light emitting diodes where the organic layer is sealed between glass plates.

A potential problem that pervades all narrow band metals is the risk of a phase-transition to magnetic-, charge density wave-, or Mott-insulating ground states. Such phase-transitions are often driven by a high density of states at the Fermi level. Thus the ideal metallic band for plasmonics should be wide enough to avoid such phase transitions and narrow enough to separate the intraband transitions from the interband transitions. Our calculations indicate that the chalcogenides are stable towards local structural distortions, but do not rule out the possibility of charge density wave-like distortions with larger periodicity. In fact, some of the metallic TMDs are known to exhibit charge density waves at low temperatures. On the other hand, at room temperature the presence of these phases is not expected to influence the optical properties that are governed by the gross features of the electronic structure. Moreover, the band width of the chalcogenides are comparable to those of the TMDs (see Figure 5(b)) which are known to behave as normal metals at room temperature, even for few layer samples[29].

Finally, we point to an added benefit of the vdW metals proposed in this work. Namely, their 2D nature allow them to be stacked with other non-metallic 2D materials like MoS<sub>2</sub> or hexagonal boron-nitride, to produce van der Waals metamaterials with ultra thin layer thickness and atomically well defined interfaces. We stress that it is very likely that the van der Waals metals proposed here should exhibit a lower scattering strength (controlled by the parameter  $a$  in Eq. (3)) compared to conventional metals like silver and gold. Indeed, the noble metals primarily used in plasmonics, exhibit relatively high losses arising from intraband transitions via scattering on surface and interface roughness[11, 30-32]. In contrast, the 2D materials form highly crystalline interfaces thus lowering the concentration of interfacial defects in actual devices. Combined with their intrinsic low-loss nature, this opens new perspectives for the fields of plasmonics and optical metamaterials.

## METHODS

### Electronic structure code

All electronic structure calculations have been performed with GPAW[33, 34] employing a plane wave basis sets and, unless explicitly stated, the PBE xc-functional.

The linear response optical properties were calculated on top of PBE ground states using the random phase approximation (RPA) for the density response function. The k-point integration required in the calculation of the response function was performed using the linear tetrahedron interpolation scheme[35]. Local field effects were included in all calculations of the optical response but were found to be unimportant. Spin-orbit coupling is shown in Sec. S6 to be negligible.

### Band structures

The bandstructures of 2H-TaS<sub>2</sub> (ICSD ID: 651092), 3R-NbS<sub>2</sub> (ICSD ID: 645309) and 1T-AlCl<sub>2</sub> (AlCl<sub>3</sub> ICSD ID: 155670) were calculated with a plane wave cutoff of 600 eV and a k-point density of 10 Å<sup>-1</sup>. In case of 1T-AlCl<sub>2</sub> (derived from AlCl<sub>3</sub>) we determined the out-of-plane lattice constant to be 5.9 Å from structural relaxations using the optB88-vdW functional.

### Relaxation of layered compounds

The out-of-plane lattice constant of all the layered materials were determined using the optB88-vdW functional. A plane wave cutoff of 600 eV was used when relaxing unless the compound contained oxygen in which case a cutoff of 900 eV was used. This approach was found to reproduce the experimental interlayer binding distance of 2H-TaS<sub>2</sub> to within 1%, see Fig. S3. The relaxed out-of-plane lattice constant of all the MX<sub>2</sub> compounds are presented in Fig. S4.

### Supercell calculations of defects

Optical response calculations reported in Figure 3 employed supercells of 3 × 3 × 3 and 3 × 3 × 2 primitive cells for silver and 1T-AlCl<sub>2</sub>, respectively. For silver a Monkhorst-Pack k-point sampling of 30 × 30 × 30 was employed and for 1T-AlCl<sub>2</sub> we used a sampling of size (24 × 24 × 16). A plane wave cutoff of 400 eV was employed in both response calculations. States up to at least 50 eV above the Fermi energy were included in the sum over states. These parameters were found to be sufficient for convergence of the optical response.

### Optical response of known TMDs

In calculating the optical response of the layered metals identified in Ref. [20] (Fig. 4) we employ a plane wave cutoff of 600 eV and a Monkhorst-Pack k-point density of at least 30 Å<sup>-1</sup>. States up to 40 eV above the Fermi energy were included in the sum over states. These settings were sufficient to converge the optical properties.

### Surface plasmon propagation

Surface plasmons on uniaxial substrates have been analysed in Ref. [36]. They show that in the case of purely real dielectric functions the single interface surface plasmon polaritons (Fig. 4) exist only if  $\varepsilon_{\parallel} < 0$  and either  $\varepsilon_{\parallel}\varepsilon_{\perp} > \varepsilon_D^2$  or  $\varepsilon_{\perp} > \varepsilon_D$  where  $\varepsilon_D$  is the dielectric function

of the dielectric and  $\varepsilon_{\parallel}$  and  $\varepsilon_{\perp}$  are respectively the in-plane and out-of-plane component of the dielectric tensor of the uniaxial material. The curves in Fig. 4(b-d) are only shown when the real parts of the dielectric functions fulfill one of these requirements.

For the IMI waveguide the surface plasmon modes have been determined using the method of Ref. [37]. For TM-polarized modes in uniaxial waveguides the dispersion relations to be solved become

$$L+ : \quad \varepsilon_{M,\parallel}k_{\perp,D} + \varepsilon_D k_{\perp,M} \tanh\left(\frac{-ik_{\perp,M}d}{2}\right) = 0 \quad (6)$$

$$L- : \quad \varepsilon_{M,\parallel}k_{\perp,D} + \varepsilon_D k_{\perp,M} \coth\left(\frac{-ik_{\perp,M}d}{2}\right) = 0 \quad (7)$$

for the antisymmetric (L+) and the symmetric (L-) modes with respect to the tangential electric field. Here  $k_{\perp,M} = \sqrt{\varepsilon_{\parallel}\omega^2/c^2 - \varepsilon_{\parallel}k_{\parallel}^2/\varepsilon_{\perp}}$  and  $k_{\perp,D} = \sqrt{\varepsilon_D\omega^2/c^2 - k_{\parallel}^2}$  are the wave vector components perpendicular to the metal-insulator interface in the metal and dielectric, respectively.

### HSE06 calculations

The HSE06 calculations were performed non-self consistently on top of PBE. In case of 2H-TaS<sub>2</sub>, the HSE06 calculation employed a gamma-centered Monkhorst Pack k-point sampling of (22, 22, 6) and a plane wave cutoff of 600 eV. For HfBrS we used a gamma-centered Monkhorst Pack k-point sampling of (8, 8, 4) and a plane wave cutoff of 600 eV.

### HSE response calculations

For 2H-TaS<sub>2</sub> we found that a scissor operator of 0.55 eV on both gaps reproduced the DOS calculated by HSE (Fig. S11). For HfBrS we found that scissor operators of 0.7 eV and 0.5 eV on the lower and upper gaps, respectively, was sufficient to reproduce the DOS of HSE. We calculated the HSE response by applying the scissor operators to the PBE ground states using the PBE transition matrix elements.

### Stability of MX<sub>2</sub>-compounds and halides

The monolayer stability of the transition metal chalcogen-halogen (MX<sub>2</sub>) compounds was evaluated based on the convex hull of the competing phases. The competing phases were determined using the Open Quantum Materials Database (OQMD) and includes 2-4 different structures in addition to the elemental phases. The heat of formation of the MX<sub>2</sub> compounds and all the competing phases were calculated using the fitted elemental phase reference energies (FERE) for the standard states [38]. A Monkhorst-Pack k-point sampling of (7, 7, 3) and a plane wave cutoff of 800 eV was employed and found to be sufficient for converging the total energy. The computed hull energies and heats-of-formation are presented in Table SII and Fig. S5.

## 5.3 Paper III: Layered van der Waals crystals with hyperbolic light dispersion

The paper is submitted.

# Layered van der Waals crystals with hyperbolic light dispersion

M.N. Gjerding and K.S. Thygesen

*Institute of Physics, Technical University of Denmark (DTU), DK-2800 Kgs. Lyngby,  
Denmark and Center for Nanostructured Graphene (CNG), DK-2800 Kgs. Lyngby, Denmark*

R. Petersen and T.G. Pedersen

*Department of Physics and Nanotechnology, Aalborg University, DK-9220 Aalborg East,  
Denmark and Center for Nanostructured Graphene (CNG), DK-9220 Aalborg East, Denmark*

N.A. Mortensen

*Department of Photonics Engineering, Technical University of Denmark, DK-2800 Kongens Lyngby,  
Denmark and Center for Nanostructured Graphene (CNG), DK-2800 Kgs. Lyngby, Denmark*

(Dated: December 19, 2016)

Artificially structured materials with hyperbolic light dispersion represent one of the most intriguing and useful types of electromagnetic metamaterials[1, 2]. Their unusual properties include strong enhancement of spontaneous emission[3, 4], diverging density of states[5], negative refraction and hyperlensing[6], all originating from their sub-wavelength structured anisotropy. Here we show, using first principles calculations, that the broad class of layered transition metal dichalcogenides (TMDs) are naturally hyperbolic. The diverse electronic properties of the TMDs result in a large variation of the hyperbolic frequency regimes ranging from the near-IR to the UV. Compared to artificially structured metamaterials[7, 8], the absence of internal structure reduces scattering losses and greatly increases the number of hyperbolic modes leading to extremely large and broadband Purcell factors. We demonstrate how the hyperbolic properties can be further controlled by combining different two-dimensional crystals into van der Waals heterostructures opening new perspectives for atomic-scale design of photonic metamaterials and as an application, we identify candidates for Purcell factor control of emission from diamond nitrogen-vacancy centers.

The dispersion relation of light in a homogeneous, anisotropic layered medium is determined by the equation

$$\frac{k_{\parallel}^2}{\varepsilon_{\perp}(\omega)} + \frac{k_{\perp}^2}{\varepsilon_{\parallel}(\omega)} = \frac{\omega^2}{c^2} \quad (1)$$

where  $\parallel$  and  $\perp$ , respectively, indicate the in-plane and out-of-plane components of the dielectric function,  $\varepsilon$ , and the wave vector  $k$ . For frequencies where the in-plane and out-of-plane dielectric functions differ in sign, the isofrequency surfaces become hyperbolic with an apparent divergence of the photonic density of states. Effective medium theory[1] (EMT) predicts that metamaterials

composed of metallic nanostructures embedded in a dielectric medium, as sketched in Figure 1(a,b), become hyperbolic over wide frequency ranges and that effects such as the enhanced Purcell factor become broadband[5], in stark contrast to alternative methods for Purcell factor enhancement based on resonant cavities or localized surface plasmon resonances that are inherently narrow band[9].

In reality, however, EMT and the homogeneity assumption underlying Eq. (1) break down when the electromagnetic modes vary on a length scale comparable to the structural periodicity of the material ( $d$ )[10]. Consequently, the hyperbolic dispersion of the medium becomes limited to wave vectors smaller than  $k_{\max} \sim \pi/d$ , see Figure 1. On the microscopic level, the broadband response of the metamaterial results from the hybridization of surface plasmons at the metal-dielectric interfaces. This implies that broadband response can be realised only if the surface plasmons have significant spatial overlap over a wide frequency range. It turns out that this condition is hardly fulfilled for conventional metamaterials[11]. In principle, the problem could be overcome by reducing the film thickness. However, downscaling of metal-dielectric structures to sub-10 nm periodicity is highly challenging and inevitably leads to increased interface roughness and enhanced scattering losses that are detrimental to metamaterial performance[12].

Recently, a few materials have been reported to exhibit hyperbolic dispersion in their pristine form[13–15]. Hexagonal boron nitride (hBN) was shown to be hyperbolic in its Reststrahlen band between the longitudinal and transverse optical phonon branches[16, 17] while graphite[13] and the tetradymites  $\text{Bi}_2\text{Se}_3$  and  $\text{Bi}_2\text{Te}_3$ [14] are hyperbolic in the UV and near-IR to visible, respectively. Natural hyperbolic materials have the obvious advantages over traditional metamaterials that they require no artificial structuring and contain no internal interfaces for the electrons to scatter off. Moreover, due to their homogeneous nature, the hyperbolic dispersion is expected

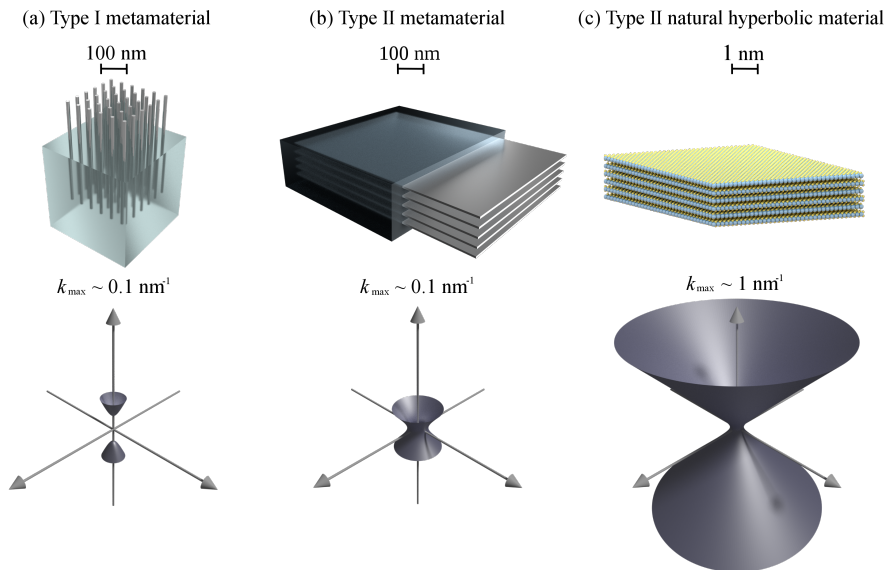


FIG. 1. **Hyperbolic materials.** Metal nanowire- (a) and planar multilayer- (b) metamaterials are artificially structured materials engineered to exhibit metallic response in some directions and dielectric response in others. In the effective medium limit this anisotropy leads to hyperbolic isofrequency surfaces which in principle would result in a diverging photonic density of states. In reality, the hyperbolic dispersion is only realized for wave vectors up to  $k_{\max} \sim \pi/d$ , where  $d$  is the periodicity of the medium which is typically on the order of tens of nanometers. Natural hyperbolic materials (c) possess no artificial structuring and their hyperbolic dispersion extends much further in reciprocal space being limited only by the atomic periodicity of the crystal structure.

to extend much further in reciprocal space (Fig. 1(c)) - in principle only limited by the atomic periodicity of the crystal lattice or effects of non-local dielectric response. Although these advantages appear plausible their significance have so far not been quantified.

Here we report on the discovery of a large class of natural hyperbolic materials with optical properties greatly surpassing those of conventional metamaterials and presently known natural hyperbolic materials. Out of a set of 31 layered TMDs, our first-principles calculations predict hyperbolic dispersion for all the materials over a broad frequency span from the near-IR to the UV. As a unique feature, the metallic TMDs are hyperbolic below the onset of interband transitions leading to extremely large broadband Purcell factors governed by weakly damped hyperbolic modes. Using effective medium theory to evaluate dielectric tensors, we show how the hyperbolic properties can be further tuned by stacking layers from different TMDs into van der Waals (vdW) heterostructures allowing for the design of atomic-scale structured metamaterials with Purcell factors tailored for specific emission sources.

We used first-principles density functional theory (DFT) and linear response calculations to investigate the

optical properties of 31 non-magnetic TMDs with experimentally known crystal structures[18]. Figure 2 shows the calculated hyperbolic spectral range of the TMDs. Quite surprisingly all the materials, including metals and semiconductors, are predicted to be hyperbolic in some frequency range. The materials exhibit predominantly Type II dispersion corresponding to metallic response in-plane and dielectric response out-of-plane. The strong dielectric anisotropy arises from the weak interlayer coupling that lowers carrier velocities and plasma frequencies perpendicular to the layers. We note that while the qualitative trends predicted by our DFT calculations, that employ the Perdew-Burke-Ernzerhof (PBE) exchange-correlation (xc) functional, are very reliable, the quantitative accuracy is subject to some uncertainty. In particular, PBE is known to underestimate band gaps and interband transition energies which is expected to influence the optical properties including the precise position of the hyperbolic regimes. To investigate the role of the xc-functional we have compared the dielectric function of 2H-TaS<sub>2</sub> obtained with the PBE and the more accurate but computationally expensive HSE[19] functional (see Fig. S1 in the supplementary information). We find that the HSE blueshifts the interband transitions by around

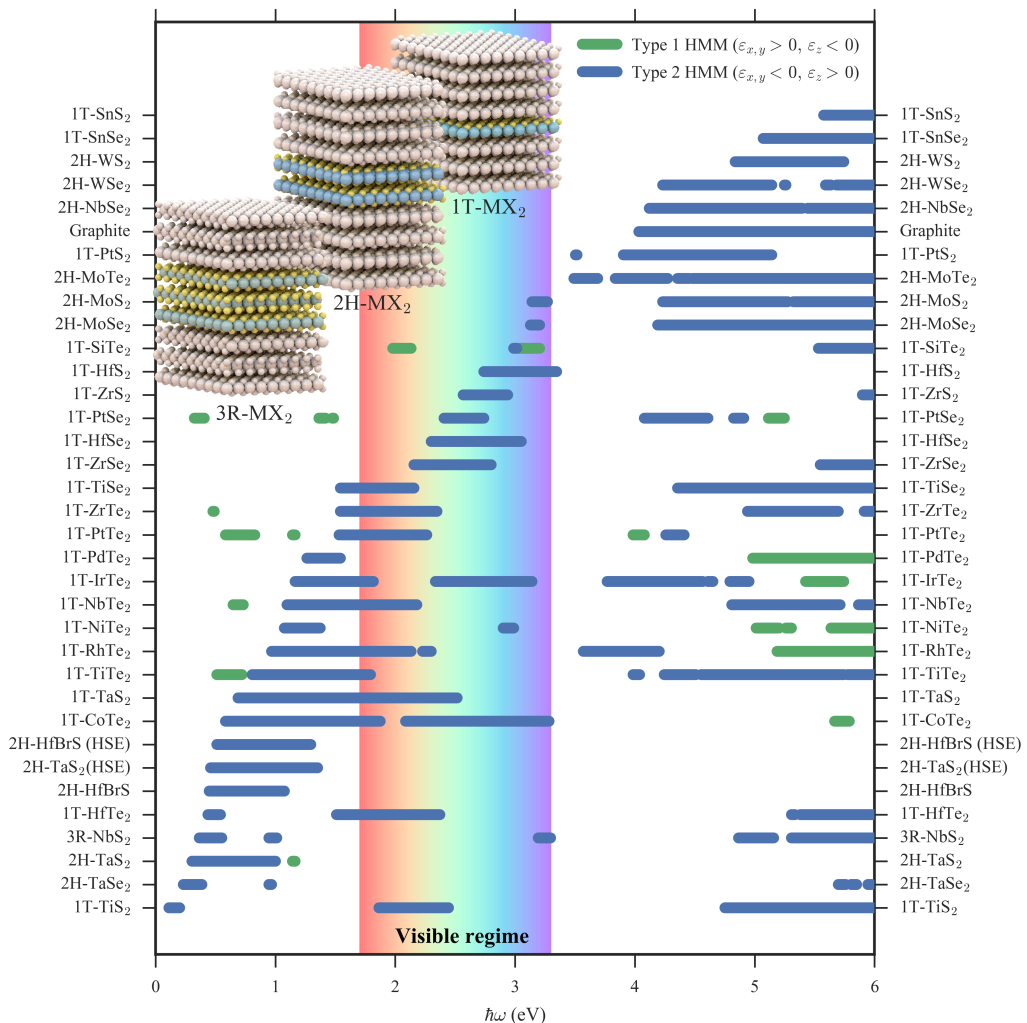


FIG. 2. **Natural hyperbolic materials.** The hyperbolic frequency ranges of the transition metal dichalcogenides (TMDs) investigated in this work. The hyperbolic dispersion of the TMDs is predominantly Type II (blue) corresponding to metallic response in-plane and dielectric response out-of-plane. The dielectric functions have been calculated on top of DFT-PBE wave functions. The result for 2H-TaS<sub>2</sub> and 2H-HfBrS obtained with the HSE functional is shown for comparison.

0.5 eV relative to the PBE result. These shifts change the Type II hyperbolic regime of 2H-TaS<sub>2</sub> from 0.3 – 1.1 eV (PBE) to 0.4 – 1.3 eV (HSE), see Figure 2. Similar changes are expected for the other materials.

To compare the performance of the natural hyperbolic TMDs to a conventional metamaterial we used the transfer matrix method to calculate the Purcell factor for a point dipole placed 1 nm above the surface of 2H-TaS<sub>2</sub> and a Ag-SiO<sub>2</sub> heterostructure, respectively (see Fig.

3(a)). For the Ag-SiO<sub>2</sub> structure we used fill-fraction of 50% and a periodicity of  $d = 20$  nm. The Purcell factor is defined as the ratio between the actual decay rate of the emitter ( $\Gamma$ ) and the free-space value ( $\Gamma_0$ ) and was calculated as described in the Methods section. The Ag-SiO<sub>2</sub> structure is hyperbolic in the range 0 – 2.4 eV while the 2H-TaS<sub>2</sub> crystal is hyperbolic from 0.4 – 1.3 eV (we use the HSE result for this example).

The broadband Purcell factor of TaS<sub>2</sub> exceeds that

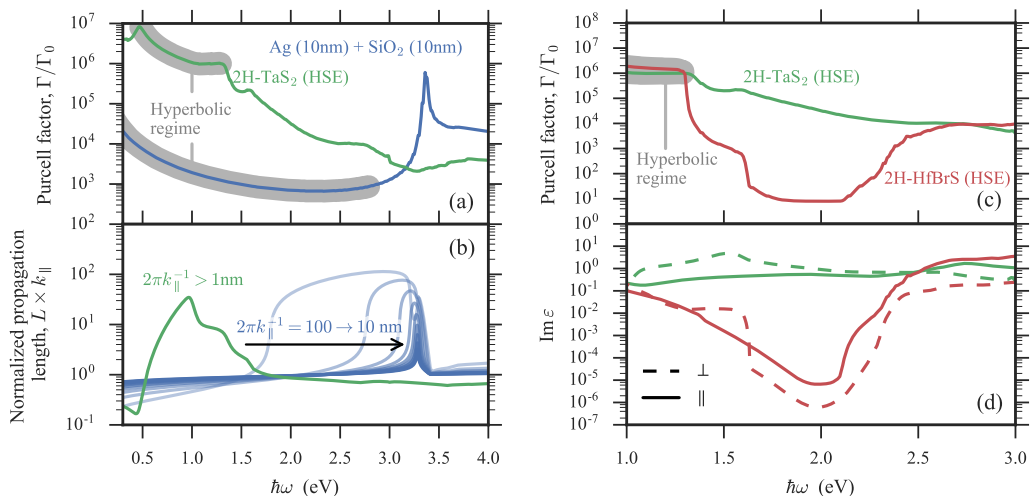


FIG. 3. **Purcell factors and losses.** (a) Purcell factors and (b) propagation lengths for a 50 nm thick film of the TMD 2H-TaS<sub>2</sub> compared with a 100 nm thick hyperbolic metamaterial consisting of alternating Ag-SiO<sub>2</sub> films with a period of 20 nm (10 nm Ag - 10 nm SiO<sub>2</sub>) and 50% fill fraction. The dipole is placed a distance of  $h = 1$  nm above the substrate. The Purcell factors were calculated using the transfer matrix method. The propagation lengths are shown for various in-plane wave vector components corresponding to wavelengths in the nanometer regime ( $\lambda = 2\pi k_{\parallel}^{-1}$ ). Reduced optical losses in 2H-HfBrS compared to 2H-TaS<sub>2</sub> significantly reduces the associated quenching of spontaneous emission which is evident when comparing (a) Purcell factors of 50 nm thin films with (b) the imaginary part of their dielectric functions.

of the metamaterial by 2-3 orders of magnitude. This is a direct consequence of the homogeneous nature of the TaS<sub>2</sub> crystal which extends the hyperbolic isofrequency surface to atomic-scale wavevectors. Indeed, in the present example, the Purcell factor is not limited by the intrinsic properties of the TaS<sub>2</sub> crystal but rather by the finite distance between the emitter and the surface which introduces a natural cut-off on the wave vectors that can couple to the near-field of the emitter. For distances below 1 nm, the Purcell factor of TaS<sub>2</sub> increases further while that of the Ag-SiO<sub>2</sub> metamaterial remains constant being limited by the heterostructure periodicity. When the emitter is brought closer to the surface, the Purcell factor of TaS<sub>2</sub> is eventually limited by the non-local response of the medium (also known as spatial dispersion)[20] which arises from the atomic periodicity of the crystal and manifests itself in a non-trivial wavevector dependence of the dielectric function[21]. A detailed analysis of the effect of non-local response is provided in the supplementary material Sec. S2. The relatively low Purcell factor of the Ag-SiO<sub>2</sub> structure is due to the small hyperbolic isofrequency surface and corresponding small enhancement of the density of states. The strong decay of the electromagnetic field inside the Ag layers leads to negligible hybridization between the surface plasmons implying that the broadband response is lost and explaining the narrow peak in the Purcell fac-

tor at 3.3 eV which originates from the unhybridized Ag surface plasmon.

Applications such as hyperlensing depend critically on the propagation of light modes through the hyperbolic medium. In Figure 3(b) we show the propagation length (normalized by the in-plane wavelength) of the hyperbolic modes in the direction normal to the film. The relatively low propagation lengths found for the Ag-SiO<sub>2</sub> metamaterial originates from the weak hybridisation of the silver surface plasmons which leads to weak dispersion and thus low group velocities in the normal direction. The attenuation length,  $\kappa^{-1}$ , of the electromagnetic field inside the Ag slabs is determined by the dispersion  $\kappa^2 = k_{\parallel}^2 - \epsilon_{\text{Ag}}(\omega)\omega^2/c^2$ [22] explaining the observed dependence of the propagation length on frequency and in-plane wavevector. In comparison, the hyperbolic modes in TaS<sub>2</sub>, propagate deeper into the film and exhibit a much weaker dependence on wavelength.

The metallic nature of 2H-TaS<sub>2</sub> is key to its large Purcell factor. Indeed, we find similar results for the other metallic TMDs while the semiconductors generally show much lower values (see Sec. S4 of the SI). Due to the dramatic increase of damping above the onset of interband transitions, the Purcell factor becomes completely dominated by quenching and the normalized propagation length of hyperbolic modes rarely exceeds unity (Fig. S4). Our calculations show that this problem is severe for

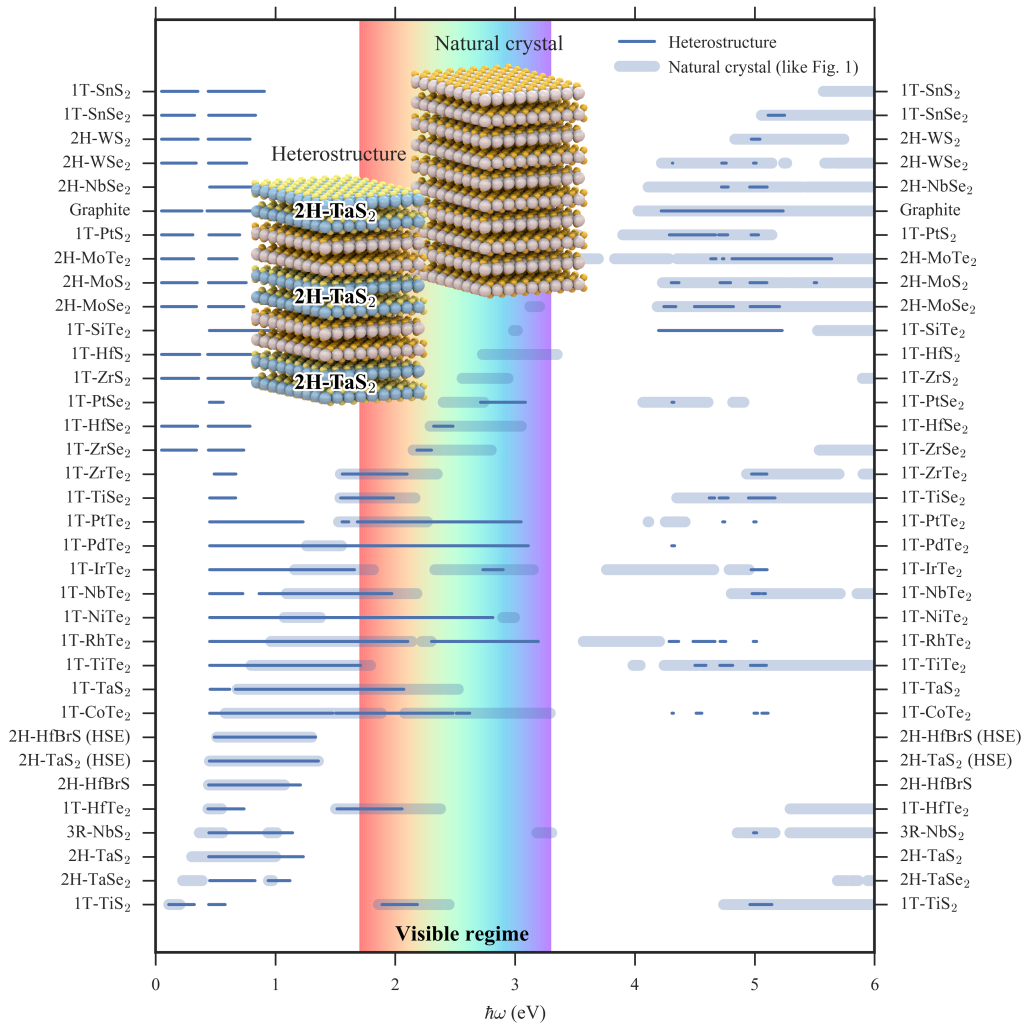
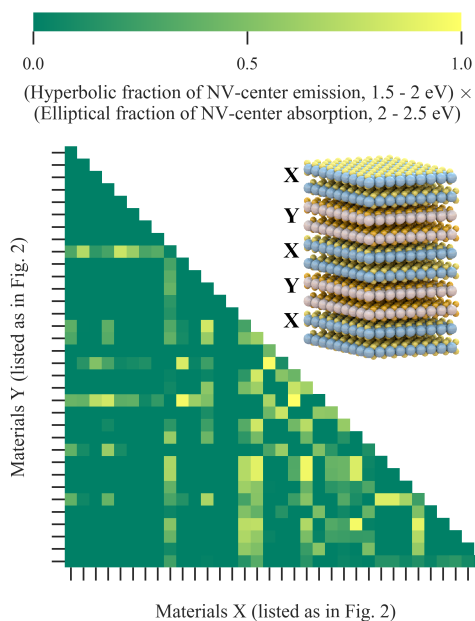


FIG. 4. **Hyperbolic van der Waals heterostructures.** The hyperbolic spectral regimes of heterostructures consisting of 50 % 2H-TaS<sub>2</sub> and 50 % of another TMD (narrow lines). For comparison the hyperbolic regimes of the pristine TMDs are repeated from Fig. 1 (faded wide lines). The hyperbolic regimes of the heterostructures can differ substantially from those of the constituent compounds.

graphite and we expect similar results for all other known natural hyperbolic materials none of which are metals. In contrast, clear signatures on the Purcell factor enhancement due to propagating hyperbolic modes are observed for the metallic TMDs showing that quenching does not dominate the properties of the metals. The long propagation lengths of 2H-TaS<sub>2</sub> is a consequence of its special band structure with conduction bands being separated from other bands by finite energy gaps which reduces damping at finite frequencies[23].

Materials exhibiting a large variation in Purcell factor over a narrow frequency range could be used to control the emission rate of an emitter *via* the emission frequency[24]. Such control is essential for generating single photons on demand as required by many applications in quantum information technology[25]. Returning to Figure 3(a) we note that 2H-TaS<sub>2</sub> shows a rather modest decrease in Purcell factor outside the hyperbolic regime (0.4 – 1.3 eV). The reason for the weak relative change in Purcell factor is quenching, i.e. enhanced emission due to



**FIG. 5. Heterostructures with tailored hyperbolic dispersion.** The possibility of tuning the hyperbolic dispersion by combining different two-dimensional crystals into van der Waals heterostructures is illustrated by the search for a two-component TMD superlattice with hyperbolic (normal) dispersion in the emission (absorption) spectrum of an NV-color center in diamond. The color scheme indicates the fraction of hyperbolic to normal dispersion over the emission band (1.5 - 2 eV) times the fraction of normal to hyperbolic dispersion over the absorption band (2 - 2.5 eV). Lighter color thus correspond to better candidate materials. The sheer number of good candidates found indicates that significant control of the optical properties can be achieved via vdW heterostructuring.

evanescent modes existing at the surface of the material both inside and outside the hyperbolic frequency range. The contribution to the Purcell factor from such evanescent modes is proportional to the imaginary part of the dielectric constant[5] suggesting that Purcell factors with large on/off ratios may be realized in hyperbolic materials with small  $\text{Im}\epsilon$  throughout the hyperbolic frequency regime. The chalcogen-halogen mixed compound 2H-HfBrS, which was recently identified by computational screening of low-loss materials for plasmonics[23], represents such a material. The electronic band structure of 2H-HfBrS features a single metallic band that is separated from all higher and lower lying bands by finite energy gaps. This type of band structure suppresses the number of final states for scattering in an energy range between the intraband and interband transitions, leading to a small imaginary part of the dielectric function.

Figure 3(c) compares the calculated Purcell factors of 2H-TaS<sub>2</sub> and 2H-HfBrS. It is clear that 2H-HfBrS shows a much more dramatic decrease in Purcell factor when the frequency is moved outside the hyperbolic regime. The lower panel of the figure (Fig. 3(d)), showing the imaginary part of the dielectric functions, reveals that this difference is indeed due to the lower losses in 2H-HfBrS which suppresses the effect of quenching on the Purcell factor.

We next explore the possibility of controlling the light dispersion by combining different TMDs, or other two-dimensional materials, into vdW heterostructures. Traditionally, such control is obtained by varying the fill fraction or by changing the metal or dielectric components of the hyperbolic metamaterial[26]. However, in order to ensure sufficient hybridization between surface plasmons at the interfaces, the metallic fill fraction cannot be too large (the example discussed in relation to Figure 3 shows that this problem is severe even for metal films as thin as 10 nm). Moreover, the number of useful metal-dielectric combinations is limited by the lattice matching required when fabricating high quality thin films. In contrast, the weak interlayer bonding in van der Waals crystals relaxes the requirement of lattice matching at the interfaces thereby removing the restriction on the type of materials that can be combined. Furthermore, vdW interfaces can be atomically sharp presenting much fewer defects than covalently bonded, epitaxially grown interfaces.

To illustrate the degree of tuning that can be achieved by vdW heterostructuring, we have used effective medium theory to calculate the hyperbolic frequency regimes of heterostructures obtained by combining each of the investigated TMDs with 2H-TaS<sub>2</sub> (50% fill fraction). By employing effective medium theory we neglect the influence of hybridization at the interfaces, see SI Sec. S3 for justification of this approach. Figure 4 shows that the process of heterostructuring can shift, expand or reduce the hyperbolic frequency regime as compared to those of the constituent materials.

As a specific design example, suppose we are interested in a material with hyperbolic dispersion in the spectral range 1.5 - 2 eV and normal (elliptical) dispersion in the spectral range 2 - 2.5 eV. The two intervals correspond, respectively, to the emission- and absorption spectral range of a nitrogen-vacancy (NV) center in diamond[27], but this is not essential for the present proof-of-concept illustration. We have calculated the hyperbolic regimes of heterostructures formed by combining any two TMDs with a 50% filling fraction. Figure 5 shows the fraction of the interval 1.5 - 2 eV, over which the heterostructure dispersion is hyperbolic, times the fraction of the interval 2 - 2.5 eV where it is elliptical. As can be seen several heterostructure candidates are discovered. The fact that the best candidates are not found on the diagonal (corresponding to the pristine TMDs) shows that the process of vdW heterostructuring represents a genuine extension of

the space of natural hyperbolic materials. Further tuning is obviously possible by varying the fill fraction or by considering heterostructures with more than two material components.

In conclusion, our work not only identifies a new class of natural hyperbolic materials but suggests that many other layered compounds may exhibit similar properties. We expect that these findings will stimulate further work and open new avenues for photonic metamaterials.

## METHODS

### First-principles calculations

All DFT calculations were performed using the GPAW electronic structure code[28] using a plane wave basis with energy cut-off of 600 eV. The dielectric functions of the TMDs were calculated within the random-phase approximation (RPA) using single-particle wave functions and energies obtained from DFT calculations employing the PBE exchange-correlation (xc) functional[29]. Brillouin zone integrals were performed over a k-point grid of density of 30  $\text{\AA}^{-3}$  using the linear tetrahedron method[30]. Unoccupied bands up to at least 40 eV above the Fermi energy were included in the band summation. Local-field effects were included up to a plane-wave cutoff of 60 eV.

To account for higher-order scattering processes, such as phonon- or defect-mediated intraband transitions, we include a phenomenological relaxation rate of the form  $\gamma(\omega) = a\text{JDOS}(\omega)/\omega$ , where  $\text{JDOS}(\omega)$  is the joint density of states per volume and  $a$  is a parameter controlling the scattering strength. The coupling strength parameter  $a$  is highly material- and sample specific and depends on defect concentration, defect type, electron-phonon coupling strength etc. For consistency we use the same value of  $a$  for all materials considered in this work.

### HSE calculations

HSE band structure calculations were performed for 2H-TaS<sub>2</sub> and 2H-HfBrS. In both cases the primary effect is to increase the interband transitions by 0.5 eV compared to the PBE result. The HSE response was calculated based on scissor-corrected PBE eigenvalues and matrix elements were calculated using the PBE wave functions.

### Purcell factor

The Purcell factor of a point dipole in the vicinity of a semi-infinite planar substrate can be derived from the knowledge of the substrate's Fresnell reflection coeffi-

cients and is given by[31]

$$\frac{\Gamma}{\Gamma_0} = 1 + \frac{3}{2k_c} \text{Re} \left( \int_0^\infty k_{\parallel} \frac{dk_{\parallel}}{k_{\perp,c}} \left[ f_{\perp}^2 \frac{k_{\parallel}}{k_c^2} r_p + \frac{1}{2} f_{\parallel}^2 \left( r_s - \frac{k_{\perp,c}^2}{k_c^2} r_p \right) \right] e^{2ik_{\perp}h} \right) \quad (2)$$

where  $k_c = k_0\sqrt{\varepsilon_c}$ ,  $k_{\perp,c} = \sqrt{k_c^2 - k_{\parallel}^2}$ ,  $f_{\perp}^2 = |\mu \cdot \hat{\mathbf{z}}|^2 / (\mu^* \cdot \mu)$ ,  $f_{\parallel}^2 = 1 - f_{\perp}^2$ ,  $\varepsilon_c$  is the dielectric constant of the cladding,  $\mu$  is an electric dipole placed a distance  $h$  above the material and  $r_p$  ( $r_s$ ) is the Fresnell reflection coefficient for  $p$  ( $s$ )-polarized light. The reflection coefficients are given by

$$r_s = \frac{k_{\perp} - k_{\perp,m}^s}{k_{\perp} + k_{\perp,m}^s}, \quad r_p = \frac{k_{\perp}\varepsilon_x - k_{\perp,m}^p\varepsilon_c}{k_{\perp}\varepsilon_x + k_{\perp,m}^p\varepsilon_c}, \quad (3)$$

where

$$k_{\perp,m}^s = \sqrt{k_0^2\varepsilon_{\parallel} - k_{\parallel}^2}, \quad k_{\perp,m}^p = \sqrt{k_0^2\varepsilon_{\parallel} - \frac{\varepsilon_{\parallel}}{\varepsilon_{\perp}}k_{\parallel}^2} \quad (4)$$

and  $k_0 = \omega/c$  is the free space wave vector.

### Propagation lengths

The propagation length of the Ag-SiO<sub>2</sub> heterostructure was calculated for an infinite periodic structure. The periodicity allows the definition of a Bloch wave vector perpendicular to the interfaces  $k_B$ . The propagation length through the slab is then  $L = (\text{Im}k_B)^{-1}$  which we normalize by the in-plane wavevector  $k_{\parallel}$ . The Bloch momentum is obtained by solving the well-known dispersion relation for planar periodic media[31],

$$\cos[k_B(d_m + d_d)] = \cos(k_{\perp,m}d_m) \cos(k_{\perp,d}d_d) \quad (5)$$

$$- \frac{1}{2} \left( \frac{\varepsilon_m k_{\perp,d}}{\varepsilon_d k_{\perp,m}} + \frac{\varepsilon_d k_{\perp,m}}{\varepsilon_m k_{\perp,d}} \right) \sin(k_{\perp,m}d_m) \sin(k_{\perp,d}d_d), \quad (6)$$

where  $d_m$  and  $d_d$  are the metal and dielectric layer thicknesses, respectively,  $k_{\perp,m} = \sqrt{k_0^2\varepsilon_m - k_{\parallel}^2}$  and  $k_{\perp,d} = \sqrt{k_0^2\varepsilon_d - k_{\parallel}^2}$  are the transverse wave numbers for the metal and dielectric, respectively, and  $\varepsilon_m$  and  $\varepsilon_d$  are the dielectric functions of the metal and dielectric components, respectively.

## AUTHOR CONTRIBUTIONS

MNG performed the DFT linear response calculations and RP calculated the Purcell Factors. KST and TGP supervised the project. All authors contributed to the discussion and data analysis. The first draft was written by MNG and all authors commented on the manuscript.

## ACKNOWLEDGEMENTS

The Center for Nanostructured Graphene (CNG) is sponsored by the Danish National Research Foundation, Project No. DNRF103. TGP was supported by VKR center QUSCOPE.

- 
- [1] Poddubny, A., Iorsh, I., Belov, P. & Kivshar, Y. Hyperbolic metamaterials. *Nature Photonics* **7**, 948–957 (2013).
- [2] Ferrari, L., Wu, C., Lepage, D., Zhang, X. & Liu, Z. Hyperbolic metamaterials and their applications. *Progress in Quantum Electronics* **40**, 1–40 (2015).
- [3] Krishnamoorthy, H. N. S., Jacob, Z., Narimanov, E., Kretzschmar, I. & Menon, V. M. Topological Transitions in Metamaterials. *Science* **336**, 205–209 (2012).
- [4] Lu, D., Kan, J. J., Fullerton, E. E. & Liu, Z. Enhancing spontaneous emission rates of molecules using nanopatterned multilayer hyperbolic metamaterials. *Nat Nano* **9**, 48–53 (2014).
- [5] Jacob, Z., Smolyaninov, I. I. & Narimanov, E. E. Broadband Purcell effect: Radiative decay engineering with metamaterials. *Applied Physics Letters* **100**, 181105 (2012).
- [6] Jacob, Z., Alekseyev, L. V. & Narimanov, E. Optical Hyperlens: Far-field imaging beyond the diffraction limit. *Optics express* **14**, 8247–8256 (2006).
- [7] Jahani, S. & Jacob, Z. All-dielectric metamaterials. *Nat Nano* **11**, 23–36 (2016).
- [8] Baev, A., Prasad, P. N., Ågren, H., Samoć, M. & Wegener, M. Metaphotonics: An emerging field with opportunities and challenges. *Physics Reports* **594**, 1–60 (2015).
- [9] Pelton, M. Modified spontaneous emission in nanophotonic structures. *Nat Photon* **9**, 427–435 (2015).
- [10] Petersen, R., Pedersen, T. G., Gjerding, M. N. & Thygesen, K. S. Limitations of effective medium theory in multilayer graphite/hBN heterostructures. *Phys. Rev. B* **94**, 35128 (2016).
- [11] Li, T. & Khurgin, J. What are the merits of hyperbolic metamaterials? In *Conference on Lasers and Electro-Optics, FTh4D.3* (Optical Society of America, 2016).
- [12] Naik, G. V. *et al.* Epitaxial superlattices with titanium nitride as a plasmonic component for optical hyperbolic metamaterials. *Proceedings of the National Academy of Sciences of the United States of America* **111**, 7546–51 (2014).
- [13] Narimanov, E. E. & Kildishev, A. V. Metamaterials: Naturally hyperbolic. *Nature Photonics* **9**, 214–216 (2015).
- [14] Esslinger, M. *et al.* Tetradymites as Natural Hyperbolic Materials for the Near-Infrared to Visible. *ACS Photonics* **1**, 1285–1289 (2014).
- [15] Sun, J., Litchinitser, N. M. & Zhou, J. Indefinite by Nature: From Ultraviolet to Terahertz. *ACS Photonics* **1**, 293–303 (2014).
- [16] Li, P. *et al.* Hyperbolic phonon-polaritons in boron nitride for near-field optical imaging and focusing. *Nature Communications* **6**, 7507 (2015).
- [17] Caldwell, J. D. *et al.* Sub-diffractive volume-confined polaritons in the natural hyperbolic material hexagonal boron nitride. *Nature Communications* **5**, 5221 (2014).
- [18] Lebigue, S., Björkman, T., Klintonberg, M., Nieminen, R. M. & Eriksson, O. Two-dimensional materials from data filtering and Ab Initio calculations. *Physical Review X* **3**, 1–7 (2013).
- [19] Heyd, J., Scuseria, G. E. & Ernzerhof, M. Erratum: Hybrid functionals based on a screened Coulomb potential [J. Chem. Phys. **118**, 8207 (2003)]. *The Journal of Chemical Physics* **124** (2006).
- [20] Yan, W., Wubs, M. & Mortensen, N. A. Hyperbolic metamaterials: Nonlocal response regularizes broadband supersingularity. *Physical Review B* **86**, 205429 (2012).
- [21] Raza, S., Bozhevolnyi, S. I., Wubs, M. & Mortensen, N. A. Nonlocal optical response in metallic nanostructures. *Journal of Physics: Condensed Matter* **27**, 183204 (2015).
- [22] Pitarke, J. M., Silkin, V. M., Chulkov, E. V. & Echenique, P. M. Theory of surface plasmons and surface-plasmon polaritons. *Reports on Progress in Physics* **1**, 54 (2006).
- [23] Gjerding, M. N., Pandey, M. & Thygesen, K. S. Bandstructure engineered metals for low-loss plasmonics. *Preprint, arXiv* (2016).
- [24] Lodahl, P., Mahmoodian, S. & Stobbe, S. Interfacing single photons and single quantum dots with photonic nanostructures. *Rev. Mod. Phys.* **87**, 347–400 (2015).
- [25] Eisaman, M. D., Fan, J., Migdall, A. & Polyakov, S. V. Invited Review Article: Single-photon sources and detectors. *Review of Scientific Instruments* **82**, 071101 (2011).
- [26] Cortes, C. L., Newman, W., Molesky, S. & Jacob, Z. Quantum nanophotonics using hyperbolic metamaterials. *Journal of Optics* **14**, 063001 (2012).
- [27] Doherty, M. W. *et al.* The nitrogen-vacancy colour centre in diamond. *Physics Reports* **528**, 1–45 (2013).
- [28] Enkovaara, J. *et al.* Electronic structure calculations with GPAW: a real-space implementation of the projector augmented-wave method. *Journal of physics: Condensed matter* **22**, 253202 (2010).
- [29] Perdew, J. P., Burke, K. & Ernzerhof, M. Generalized Gradient Approximation Made Simple. *Phys. Rev. Lett.* **77**, 3865–3868 (1996).
- [30] MacDonald, A. H., Vosko, S. H. & Coleridge, P. T. Extensions of the tetrahedron method for evaluating spectral properties of solids. *Journal of Physics C: Solid State Physics* **12**, 2991–3002 (1979).
- [31] Kidwai, O., Zhukovsky, S. V. & Sipe, J. E. Effective-medium approach to planar multilayer hyperbolic metamaterials: Strengths and limitations. *Phys. Rev. A* **85**, 53842 (2012).



# CHAPTER 6

## Additional information

---

This chapter provides additional information and details on the papers, some of which can be found in the supplementary information of the papers.

### 6.1 Paper I: Limitations of effective medium theory in multilayer graphite/hBN heterostructures

The contribution to this paper was mainly the calculation of the dielectric function of graphite and hexagonal boron nitride, as well as the computation of band-structures for the fitting of the tight-binding (TB) on-site and hopping parameters. The quality of the fitting was assessed by comparing the calculated TB dielectric function with the DFT dielectric function. The TB dielectric function revealed many fine band structure effects (Fig. 2 in paper) not initially reproduced by the DFT calculations. The reason for this discrepancy was two-fold. (i) The inexpensive TB calculation could calculate the k-point integrals of the density response function employing a much denser k-point mesh (see Sec. 3.4) and (ii) the eigenvalues and matrix elements were interpolated on 2D-triangulated k-point grids when calculating the k-point integrals.

In contrast, the DFT calculations were performed on much coarser k-point grids with no interpolation of the eigenvalues and matrix elements and the k-point integrals were calculated through a simple point summation with an artificial broadening  $\eta$  (Eq. (3.23)). Figures 6.1(a), (c) and (e) present the imaginary part of the dielectric function of hBN when varying the k-point sampling and artificial broadening. The figure illustrates that as the broadening is decreased, many more k-points are needed to converge the dielectric function. This problem becomes even more severe for graphene and graphite due to their semi-metallic nature which makes the convergence of the dielectric function very difficult for small frequencies.

These difficulties motivated the implementation of the linear tetrahedron integration method for calculating k-point integrals and the utilization of crystal symmetries to reduce the volume that needed to be integrated. The implementations are discussed in detail in Chapter 7 but at this point it is highlighted that the reduction in computing time for a high symmetry system like hBN is around 90% due to the employment of symmetries alone. The equivalent number for graphite is around 95%. The convergence of the dielectric properties of hBN is shown in Figure 6.1(b), (d) and (f) for various artificial broadening parameters and the main conclusion that can

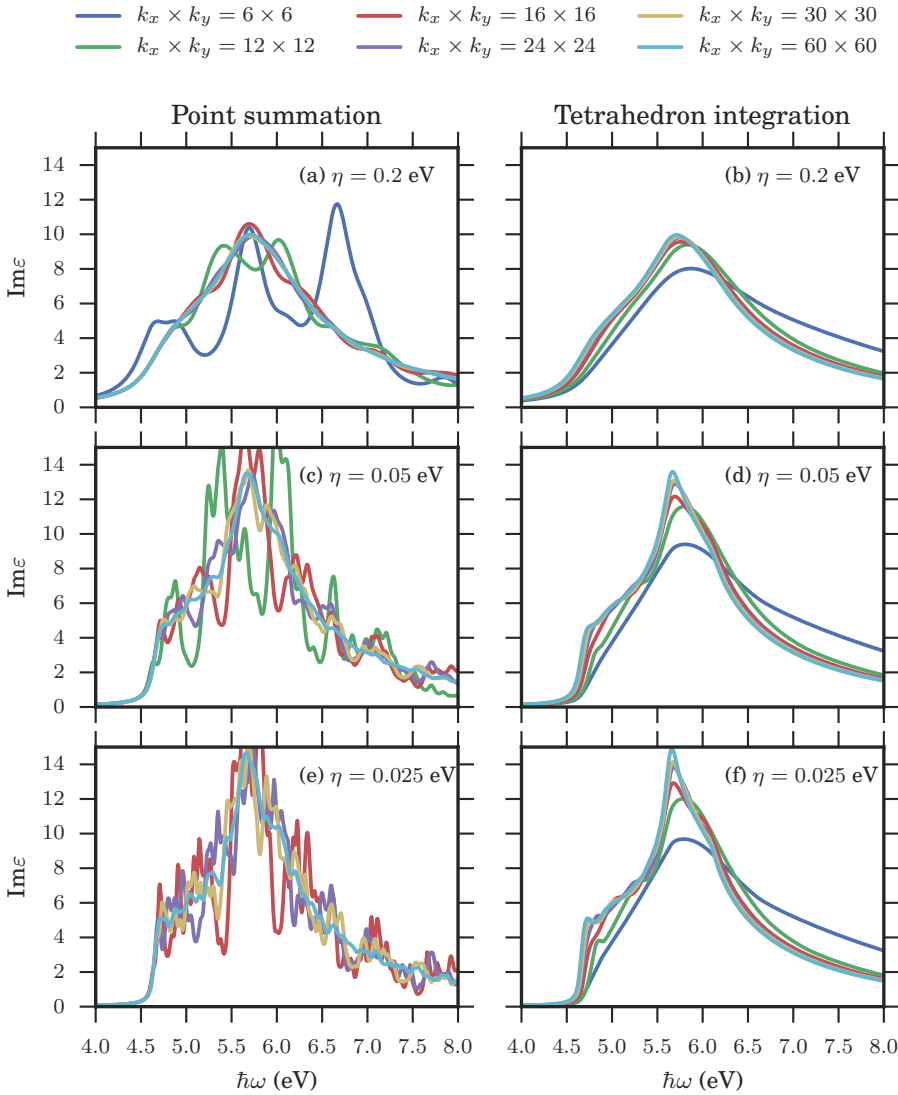


**Figure 6.1:** Testing the tetrahedron method (panels (b), (d) and (f)) for on the calculation of the optical properties of hexagonal boron nitride against the normal point summation method (panels (a), (c) and (e)) for varying broadening factors  $\eta$ . Please note that the lowest k-point samplings are not shown in (c) and (e). As the illustration shows, the tetrahedron method is a powerful method when calculating optical spectra with low broadening.

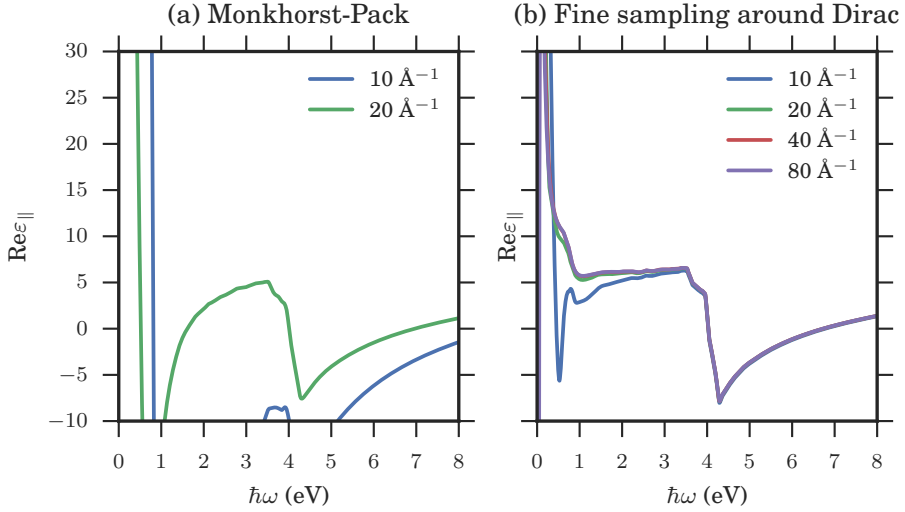


**Figure 6.2:** The tetrahedron method in itself is not enough to converge the dielectric properties of graphite for low frequencies when (a) employing a grid of homogeneously spaced k-points. This problem is tackled by (b) increasing the local k-point sampling density around the Dirac point, M-point and H-point in the Brillouin zone while keeping a rather modest sampling ( $10 \text{ \AA}^{-1}$ ) in the rest of the BZ. The discrepancy between the  $10 \text{ \AA}^{-1}$  lines in (a) and (b) originates from the fact that (b) is not a Monkhorst-Pack sampling.

be drawn is that for low broadening the tetrahedron integration method more than halves the required number of k-points in each direction for convergence, i.e., a speed up of a factor of  $> 8$ , which, combined with the speed up achieved by employing symmetries, results in a total speed up on the order of  $\sim 100$ .

The semimetallic nature of graphite (and graphene) still pose difficulties for low frequencies even when employing the linear tetrahedron method as seen in Figure 6.2(a) showing the convergence of the real part of the dielectric function of graphite with respect to k-point sampling. The origin of the bad convergence are many-fold:

- **The low density of states** at the Fermi level makes it difficult to determine the Fermi level accurately.
- **The strong dispersion** of the Dirac cone can convert a small inaccuracy of the Fermi-level into a large plasma-frequency.
- **An interband onset of 0 eV** in graphene and graphite coupled with the small

DOS means that the low-frequency properties are very sensitive to the precise k-point sampling.

Because most of the difficulties arise from a small region in reciprocal space close to the Dirac point the implemented solution was to increase the local k-point density in a sphere around the Dirac point the results of which are shown in Figure 6.2(b).

## 6.2 Paper II: Bandstructure engineered layered metals for low-loss plasmonics

### 6.2.1 Materials

The 19 metals investigated in this paper are listed in Table 6.1. The majority of the metals are tellurides (11 metals of the form  $X\text{-Te}_2$ ) with only 4 selenides ( $X\text{-Se}_2$ ) and 3 sulfides ( $X\text{-S}_2$ ). The tendency of the tellurides to be metallic originates from the decreasing hybridization of the transition metal atoms as the chalcogen atom is changed from sulfur to selenium to tellurium which increases the in-plane lattice constant (due to the larger size of Te compared to S). A similar tendency is observed for the semi-conducting TMDs[103]. Since low-loss plasmonics require large interband onsets this typically make the sulfides the most interesting candidates.

### 6.2.2 The relaxation rate model

The results on  $\text{AlCl}_2$  showed that the constant relaxation rate model was an insufficient description of the relaxation rate for the intermediate band metals due to the

Formula	Spacegroup	ICSD (ID)	Formula	Spacegroup	ICSD (ID)
$\text{TaSe}_2$	194	651950	$\text{NiTe}_2$	164	159382
$\text{TaS}_2$	194	651092	$\text{IrTe}_2$	164	33934
$\text{TaS}_2$	164	651089	$\text{RhTe}_2$	164	650448
$\text{NbTe}_2$	164	645529	$\text{CoTe}_2$	164	625401
$\text{NbS}_2$	160	645309	$\text{HfTe}_2$	164	638959
$\text{NbSe}_2$	194	645369	$\text{ZrTe}_2$	164	653213
$\text{SiTe}_2$	164	652385	$\text{TiTe}_2$	164	653071
$\text{PtTe}_2$	164	649747	$\text{TiSe}_2$	164	173923
$\text{PtSe}_2$	164	649589	$\text{AlCl}_2$	164	155670
$\text{PdTe}_2$	164	649016			

**Table 6.1:** List of 19 metals from Lebègue et al. [102]. The ICSD ID refers to the unique ID of the materials in the inorganic crystal structure database[102].

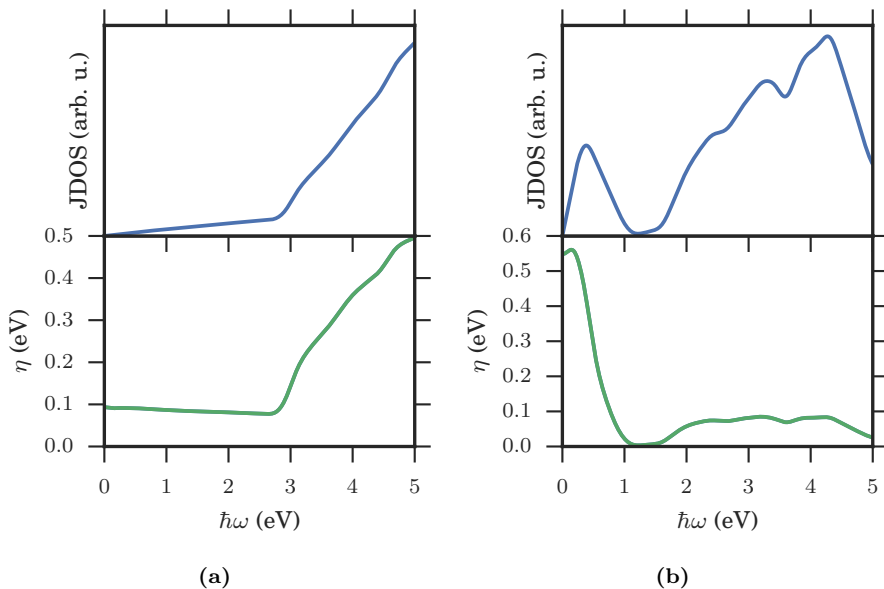


**Figure 6.3:** JDOS and relaxation rate as calculated by the relaxation rate model Eq. (4.1) for (a) silver and (b) 1T-AlCl<sub>2</sub>.

reduction in the density of states for scattering (Fig. 3 in the paper). The simple relaxation rate model based on the JDOS (Eq. (3) in the paper), however, was able to give a more accurate description of the relaxation rate in AlCl<sub>2</sub> while maintaining the good description of the constant relaxation rate approximation for silver. The reason for the latter fact is the linear frequency dependence of the JDOS in silver which means that the relaxation rate model simply reduces to the constant relaxation rate model for low frequencies (Fig. 6.3(a)). The consequence of the gapped nature of the band structure of 1T-AlCl<sub>2</sub> is that the JDOS reaches a minimum for finite frequencies entailing a small scattering rate at finite frequencies (Fig. 6.3(b)).

The relaxation rate model presented in this paper is of course a crude approximation only intended to represent the effect of finite spectral regions with little or no density of states for scattering. The model does not describe non-elastic processes where the scattering process provides (or absorbs) energy to the electron-hole pair, or higher order processes where multiple electron-hole pairs are generated as in electron-electron scattering (Fig. 2.6(d)). The effect of the non-elastic nature of phonon scattering would be to 'wash out' the low loss frequency regimes, however, since phonon frequencies of the TMDs are on the order of 50 meV[104–106] the effect would only be significant at the edges of the low-loss regimes. The relaxation rate model assumes that the scattering mechanism does not perturb the density of states of the material and importantly that no new states are introduced in gaps of the band

structure upon the introduction of a defect. Upon investigation we have found that this happens in the case of Chlorine defects in  $\text{AlCl}_2$  entailing the breakdown of our simple model. It would not be surprising that the TMDs showed similar tendencies, however, it has been shown that chalcogen vacancy defects can be effectively passivated by oxygen[107], possibly providing a method for removing defect states in the band gaps.

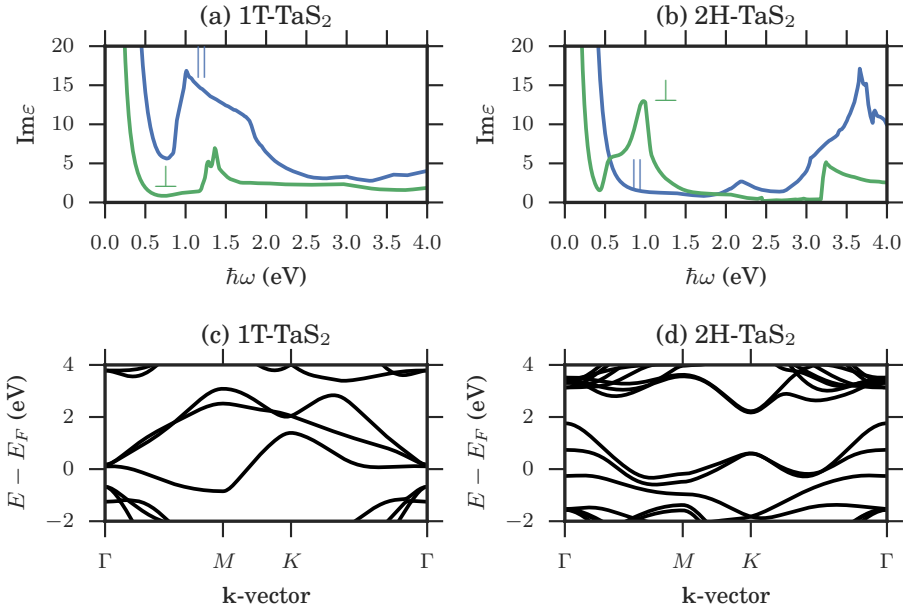
### 6.2.3 1T vs. 2H $\text{TaS}_2$

Figure 2.2 showed that the primary difference between the T and H phases of the group 5 TMDs (Ta, Nb) is the width of the conduction bands with the T structure having the widest conduction band. It is natural to expect that this will have significant implications for the plasmonic properties of the materials. The optical losses and bandstructures of 1T- $\text{TaS}_2$  and 2H- $\text{TaS}_2$  are presented in Figure 6.4 and the results are generally consistent with the simple model of Figure 2.2. The dissimilarity between the in-plane and out-of-plane losses indicate that selection rules forbid some interband transitions, which most significantly leads to different interband onsets for the two components (both in the 1T and 2H structure).

The relative importance of the components of the dielectric function for plasmonic wave guiding depends on the electric field distribution within the materials according to Poyntings theorem Eq. (2.35). For surface plasmons, the out-of-plane component of the electric field can be expressed in terms of the in-plane component as  $E_{\perp} = -\frac{\epsilon_{\parallel} k_{\parallel}}{\epsilon_{\perp} k_{\perp}} E_{\parallel}$  showing that for long wavelengths ( $k_{\parallel} \rightarrow 0$ ) it is predominantly the in-plane component of the dielectric function that matters.

### 6.2.4 HSE06 calculations

A well-known deficiency of the PBE functional is the underestimation of bandgaps for semiconductors by approximately 50%. Since it has been shown that one effect of  $G_0W_0$  on the electronic structure of 2H- $\text{TaS}_2$  is to increase the electronic gaps surrounding the conduction band[108], it seems reasonable to expect that the energy gaps of the low-loss materials in general will be underestimated. In the same reference, it was also shown that the HSE06 functional produced bandstructures in agreement with  $G_0W_0$ . This effect is especially significant for plasmonic applications since the interband onset often sets a hard limit above which losses are too large for practical applications, making it essential to get the interband onset right. Figure 6.5(a) shows that the effect of HSE06 on the DOS of 2H- $\text{TaS}_2$  is mainly to increase the size of both gaps to the conduction band by 0.55 eV. The 'HSE optical response' was therefore calculated by applying a scissor operator of the aforementioned size on the band gaps in 2H- $\text{TaS}_2$ . In doing so, the PBE wave functions were retained in the calculation of transition matrix elements. The HSE response of 2H- $\text{TaS}_2$  is presented in Fig. 6.6 where the main effects are that (i) the losses decrease due to a lower density of



**Figure 6.4:** Comparing the optical losses of (a) 1T-TaS<sub>2</sub> and (b) 2H-TaS<sub>2</sub> illustrates the large role of the crystal structure on the optical properties. The annotations mark the in-plane ( $\parallel$ ) and out-of-plane ( $\perp$ ) components of the dielectric tensor. The differences can be understood in terms of their band structures presented in (c) and (d).

states for scattering and (ii) the plasma frequencies increase due to a lower interband screening.

### 6.2.5 Interlayer vdW bonding

The interlayer vdW bonding of the chalcogen-halogen MXY compounds was initially computed with the BEEF-vdW[94] functional but it was later discovered that the optB88-vdW[95] functional yielded better results for 2H-TaS<sub>2</sub> and 2H-WS<sub>2</sub> as shown in Fig. 6.7. The BEEF-vdW functional in general overestimates the bonding distance of the layered TMDs compared to experiment by  $\sim 10\%$ , whereas the optB88-vdW functional is accurate for 2H-TaS<sub>2</sub> and gives a smaller overestimation of the bonding distance of 2H-WS<sub>2</sub> by approximately 3%. Both functionals are fitted to accurate data and the explanation of the more accurate description of optB88-vdW compared to BEEF-vdW is to be found in the datasets that have been fitted. The BEEF-vdW functional have been fitted to give a good overall description of many different

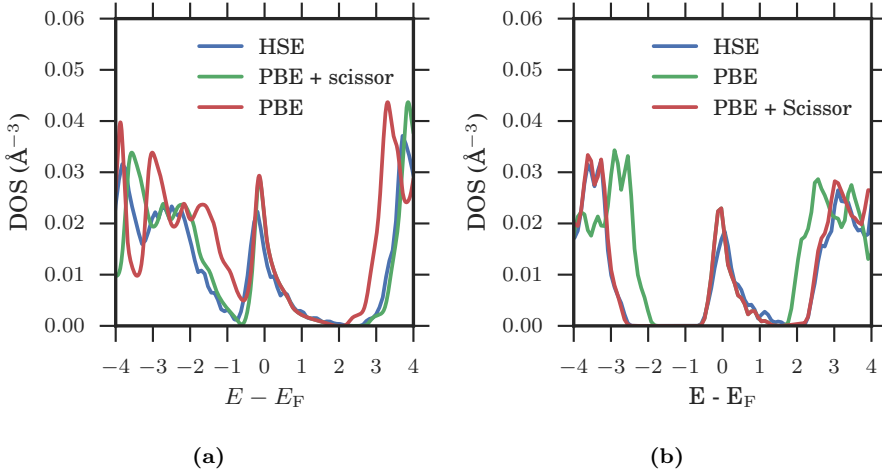


**Figure 6.5:** The effect of the HSE functional on the DOS of (a) 2H-TaS<sub>2</sub> and (b) 2H-HfBrS compared to PBE. The applied scissor operator on 2H-TaS<sub>2</sub> is 0.55 eV for both energy gaps while the operators are given by 0.7 eV (lower gap) and 0.5 eV (upper gap) for HfBrS.

physical systems, including covalently as well as vdW's bonded systems, however, the optB88-vdW functional have been fitted only on vdW bonded systems and it is therefore natural that it performs better.

It is essential to have an accurate description of the vdW's bonding since an overestimation of the bonding distance leads to an underestimation of the plasmafrequency ( $\omega_p \propto \sqrt{\text{electron density}}$ ). The relaxed out-of-plane lattice constants for the MXY compounds are shown in Fig. 6.7(c) along with the Drude plasma frequency, i.e., the unscreened plasma frequency. The materials are sorted after chalcogen, halogen and transition metal atom (in that order) showing that the lattice constant is mainly determined by the halogen atom. The plasmafrequency in general increases for increasing transition metal atomic number with the largest plasmafrequencies exhibited by the Hf compounds. Unsurprisingly, HfBrS, the best performing compound analysed in the paper, is also one of the compounds with largest unscreened plasmafrequencies indicating the importance of a large plasmafrequency.

## 6.2.6 Spin orbit coupling

It is well-known that the spin-orbit coupling (SOC) can be significant when heavy elements like tantalum are present. It has also been shown that spin orbit coupling does break the spin-degeneracy of 2H-TaS<sub>2</sub> at the K-point (Fig. 6.8 (a)). It is however not expected that this will play an important role for the plasmonic properties of the

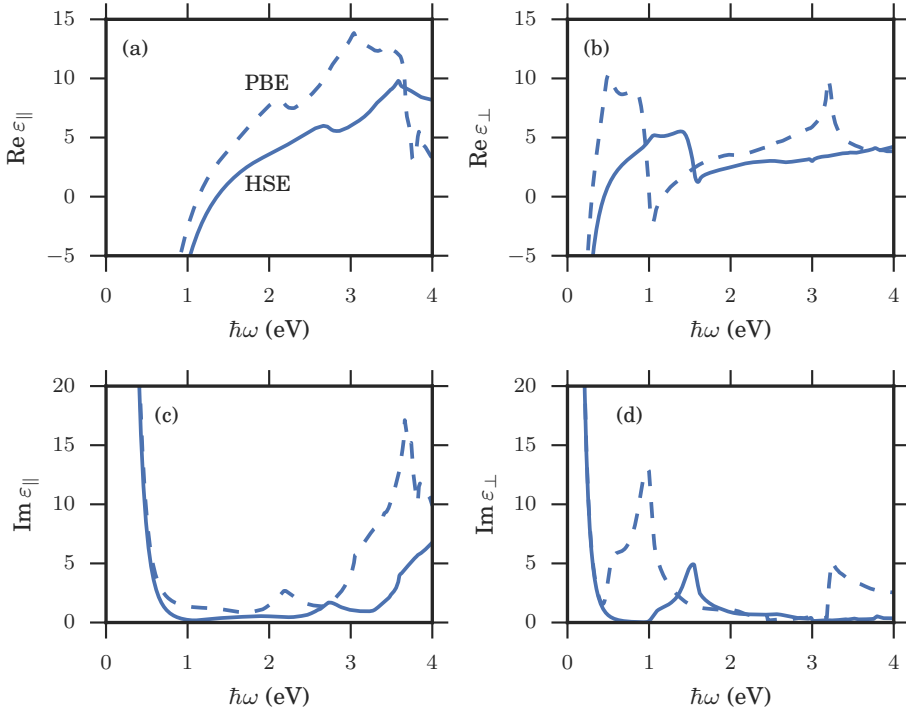


**Figure 6.6:** Calculated dielectric tensor of 2H-TaS<sub>2</sub> based on PBE (full line) and HSE (dashed line) eigen energies. Real (a) and imaginary (c) parts of the in-plane component of the dielectric tensor and real (b) and imaginary (d) parts of the out-of-plane component of the dielectric tensor.

metals because the conduction band width is not influenced, the interband edges are not influenced and the Fermi-velocities only change very slightly. Similar results are presented in Figure 6.8 (b) for HfBrS leading to essentially the same conclusions.

### 6.2.7 Charge density waves

It is well known that many of the metallic layered materials enter charge density wave (CDW) phases when the temperature decreases[28]. However, the critical temperature for these transitions are below 150 K[109] for 2H-TaS<sub>2</sub>, 2H-TaSe<sub>2</sub>, 2H-NbSe<sub>2</sub> and 2H-NbSe<sub>2</sub> and granted that the plasmonic applications are supposed to work at room temperature we do not expect the CDW phase to be important for our results. It is also not expected that the chalcogen-halogen MXY compounds undergo a CDW-phase transition due to their larger in-plane units cells which, according to our experience,

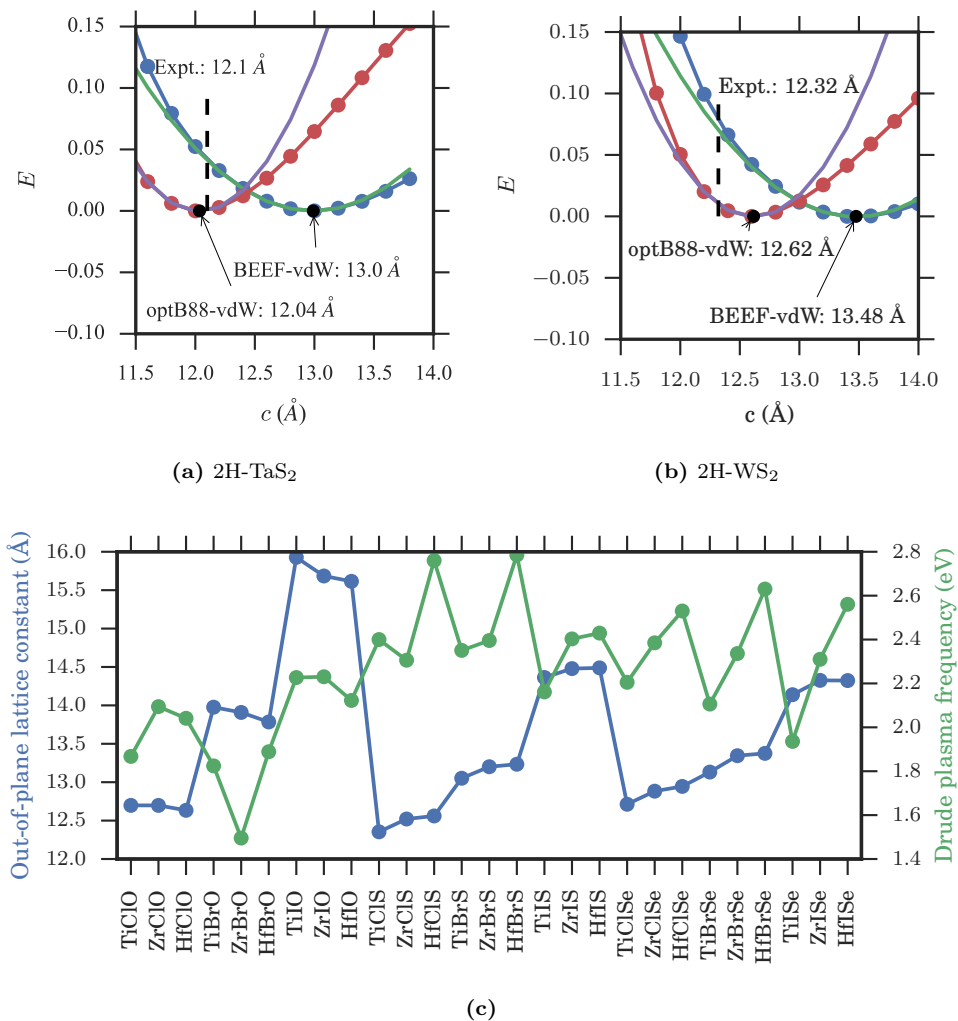


**Figure 6.7:** Relaxation of the out-of-plane lattice constant  $c$  with optB88-vdW and BEEF-vdW compared with experiments for (a) 2H-TaS<sub>2</sub>, (b) 2H-WS<sub>2</sub> and (c) the relaxed lattice constants with optB88-vdW and the associated unscreened plasma frequencies.

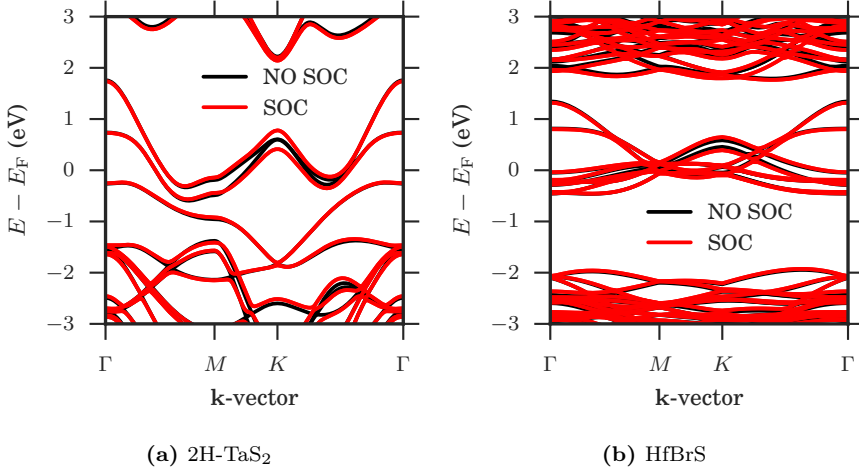


**Figure 6.8:** The effect of the spin-orbit coupling (SOC) on the bandstructure of (a) 2H-TaS<sub>2</sub> and (b) 2H-HfBrS.

often reveal the existence of CDW-phases upon relaxation.

### 6.2.8 Surface plasmons on uniaxial thin films

The description of the surface plasmons on uniaxially anisotropic media is based on the work of Warmbier, Manyali, and Quandt [110], and the derivation is similar to the one for isotropic media. The essence of their results is a changed existence condition for the SPPs on uniaxial substrates derived from the dispersion relation

$$k_{\parallel}^2 = \varepsilon_1 \varepsilon_{\perp} \frac{\varepsilon_1 - \varepsilon_{\parallel}}{\varepsilon_1^2 - \varepsilon_{\parallel} \varepsilon_{\perp}} \frac{\omega^2}{c^2} \quad (6.1)$$

$$k_{\perp,M}^2 = \varepsilon_{\parallel}^2 \frac{\varepsilon_1 - \varepsilon_{\perp}}{\varepsilon_1^2 - \varepsilon_{\parallel} \varepsilon_{\perp}} \frac{\omega^2}{c^2} \quad (6.2)$$

$$k_{\perp,D}^2 = \varepsilon_1^2 \frac{\varepsilon_1 - \varepsilon_{\perp}}{\varepsilon_1^2 - \varepsilon_{\parallel} \varepsilon_{\perp}} \frac{\omega^2}{c^2}, \quad (6.3)$$

where  $k_{\perp,M}$ ,  $k_{\perp,D}$  are the wave vector components perpendicular to the interface in the metal and dielectric, respectively, and  $k_{\parallel}$  is the wave vector component along the propagation direction. SPPs require  $\text{Re}k_{\parallel} > 0$  and  $|\text{Im}k_{\perp,(M,D)}| > 0$  and therefore localized modes are supported only when  $\varepsilon_{\parallel} < 0$  and only when either  $\varepsilon_{\perp} \varepsilon_{\parallel} > \varepsilon_1^2$  or  $\varepsilon_{\perp} > \varepsilon_1$  (for real dielectric functions). Interestingly, while isotropic metals can only support surface plasmons for  $\omega < \omega_p/\sqrt{2}$  (in vacuum), a uniaxial metal support surface plasmons for  $\omega < \omega_p$  as long as  $\varepsilon_{\perp} > 1$  (in vacuum). In contrast to SPPs

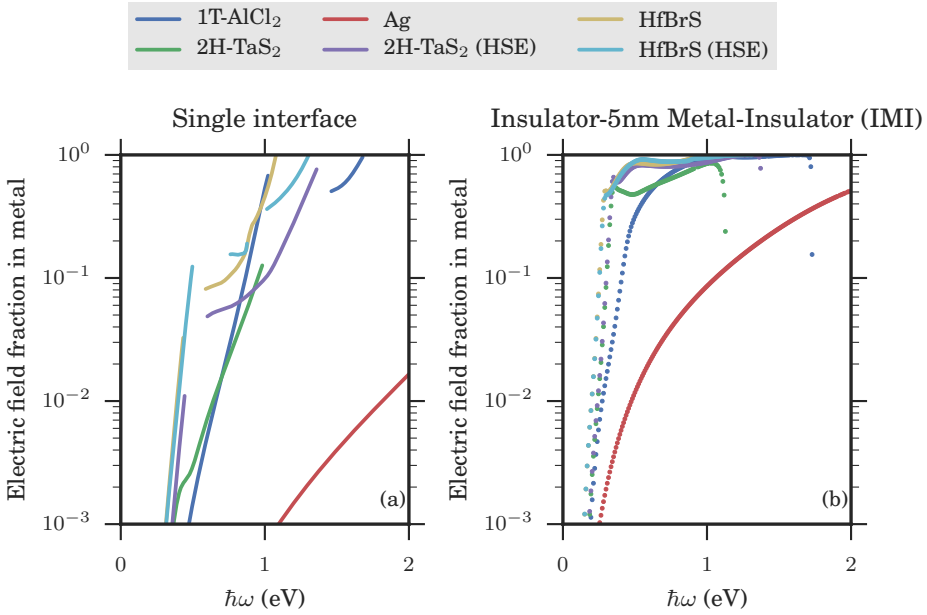


**Figure 6.9:** Field fraction of the electric field within the metallic component of (a) the single interface waveguide and (b) the thin-film waveguide.

on isotropic substrates, SPPs on uniaxial substrates generally carry a volume charge distribution in addition to a surface charge, which is seen from Gauss' law for the electric field

$$\rho = \varepsilon_0 \nabla \cdot \mathbf{E} = ik_{\parallel} \left( 1 - \frac{\varepsilon_{\parallel}}{\varepsilon_{\perp}} \right) \varepsilon_0 E_x. \quad (6.4)$$

Shorter propagation lengths were generally observed for SPPs on the investigated uniaxial substrates compared to the noble metals (Figure 4(b) in paper). The reason is partly a lower group velocity of SPPs in uniaxial substrates but additionally, that a larger fraction of the electric field contained within the uniaxial substrate as shown in Figure 6.9(a). This is caused by a larger metallic screening in the noble metals, compared to the uniaxial metals, which reduces the attenuation length of the electric field into the substrates. It is generally found that increasing the out-of-plane dielectric screening,  $\varepsilon_{\perp}$ , decreases the attenuation length within the uniaxial substrates which provides a route for decreasing plasmonic losses in uniaxial substrates.

The thin-film wave guiding modes are determined by solving Maxwell's equations for a thin film encapsulated in dielectric. Similar to the isotropic metallic thin film (Sec. 2.3.1) uniaxial substrates support symmetric and anti-symmetric modes, however, the changed boundary conditions lead to slightly different dispersion relations.

For a wave-guide centered at  $z = 0$  of width  $d$  the solutions for the tangential electric field within the thin film can be expressed as  $E_x(\mathbf{r}) = E_x^\pm(z)e^{-ik_\parallel x}$ , where  $\pm$  refer to the symmetry of the electric field in the  $z = 0$  plane

$$E_x^\pm(z) = E_0 \left( e^{ik_{\perp,M}z} \pm e^{-ik_{\perp,M}z} \right) \quad (6.5)$$

where  $k_{\perp,M}$  is the out-of-plane component of the wave vector inside the metallic thin film. The resulting out-of-plane component is obtained from Gauss' law  $\nabla \cdot \mathbf{D} = 0$ ,

$$E_\perp^\pm = -\frac{\varepsilon_{\parallel,M}k_\parallel}{\varepsilon_{\perp,M}k_{\perp,M}} E_0 \left( e^{ik_{\perp,M}z} \mp e^{-ik_{\perp,M}z} \right). \quad (6.6)$$

Continuity of the tangential electric field at the thin film interface gives the electric field distribution outside the thin film

$$E_\parallel^\pm = E_0 \left( e^{ik_{\perp,M}d/2} \pm e^{-ik_{\perp,M}d/2} \right) e^{ik_{\perp,D}(z-d/2)}, \quad z > d/2. \quad (6.7)$$

The continuity of the tangential component of the displacement field  $D_\perp^D(d/2) = D_\perp^M(d/2)$  then yield the dispersion relations

$$L^- : \quad \varepsilon_{\parallel,M}k_{\perp,D} + \varepsilon_D k_{\perp,M} \coth \left( \frac{-ik_{\perp,M}d}{2} \right) = 0, \quad \text{symmetric} \quad (6.8)$$

$$L^+ : \quad \varepsilon_{\parallel,M}k_{\perp,D} + \varepsilon_D k_{\perp,M} \tanh \left( \frac{-ik_{\perp,M}d}{2} \right) = 0, \quad \text{anti-symmetric} \quad (6.9)$$

which have been divided into two branches  $L^-$ ,  $L^+$  according to common convention [42]. Compared to the dispersion relations in isotropic thin films (Eqs. (2.20), (2.21)) the expressions above differ in that they involve the in-plane component of the dielectric function. The equations are solved numerically for the real and imaginary parts of the in-plane wave vector component following the procedure of Dionne et al. [42].

Figure 6.10 shows the dispersion relation of SPPs in silver thin-films of thicknesses  $d = 100$  nm and  $d = 10$  nm, where the grey scale colors indicate the absolute values of the left-hand side of the dispersion relations. The thin films are encapsulated in  $\text{SiO}_2$  of dielectric function  $\varepsilon = 2.1$ . The hybridization of the SPPs in the 100 nm thin film is negligible and the symmetric mode shows the same dispersion as the anti-symmetric mode shown in Figure 6.10(a). In the 10 nm thin film the hybridization is significant and the anti-symmetric mode (the LRSPP, see Sec. 2.3.1) couples only weakly with the thin film entailing very broad mode widths (not shown). The symmetric mode (the SRSPP) couples more strongly with the thin film achieving much larger wave vectors and sub-wavelength character in correspondence with literature. These conclusions are consistent with the discussion of Section 2.3.1.

Our study of thin film uniaxial waveguides showed that as the film thicknesses increase, higher order modes emerge; a property not shared by isotropic metallic thin-films. Figure 6.11(a) presents the propagating modes of a 200 nm 2H-TaS<sub>2</sub> thin film where higher order modes are observed between frequencies  $\sim 0.5 - 1.4$  eV. The

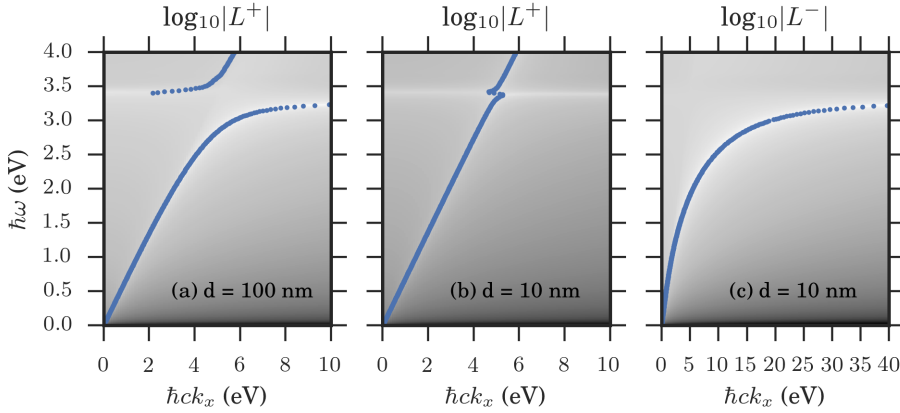


**Figure 6.10:** (a) Anti-symmetric modes in a silver thin film of 100 nm thickness. (b) Anti-symmetric and (c) symmetric modes in a 10 nm silver thin film. The shading is given by  $\log_{10}|L^\pm|$  marked above the plot (for  $\text{Im}k_x = 0.01$ ).

origin of the modes is the hyperbolic nature of 2H-TaS<sub>2</sub> (see Sec. 2.5) leading to the existence of bulk propagating modes within the waveguide, explaining why isotropic metals do not show such modes. The hyperbolic modes are generally more confined than the SPP. The higher confinement means that a larger fraction of the electric field is contained within the thin film, which generally leads to larger losses and shorter propagation lengths and lifetimes for the hyperbolic modes. The extreme subwavelength character of the hyperbolic modes and the low group velocities might make them useful for slow light applications[111, 112], however, for SPP wave guiding it is not expected that they offer a significant advantage over SRSPs in thin films which already offer great confinement. Figure 6.11(b) and (c) shows the anti-symmetric and symmetric modes of a 5 nm 2H-TaS<sub>2</sub> thin film with results resembling the silver thin film. As the thin film thickness is decreased the higher order hyperbolic modes are pushed toward larger wave vectors which explains why they are not observed for the 5 nm thin film. The light-like character of the antisymmetric LRSPP mode leads to very poor confinement and this is the reason that only the symmetric SRSP mode have been considered in the paper.

### 6.2.9 Future directions

A future study could use the insight gained here to search for uniaxial plasmonic materials that: maximise the onset of interband transitions, maximize the in-plane

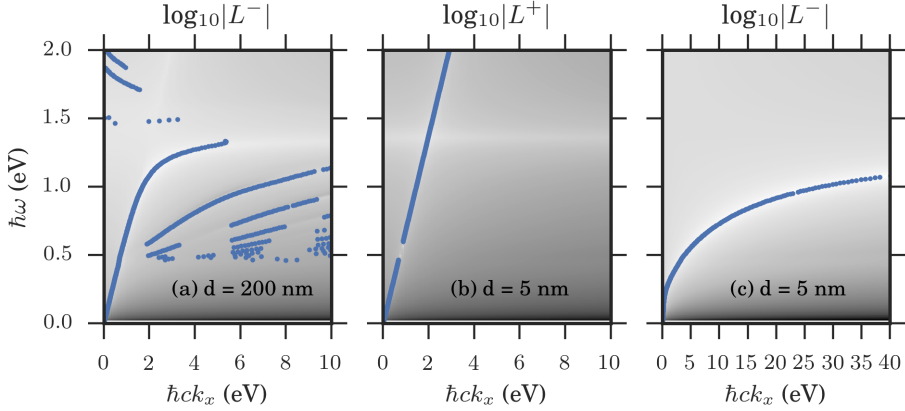


**Figure 6.11:** (a) Symmetric modes in a 2H-TaS<sub>2</sub> thin film of 200 nm thickness. Note the emergence of higher order modes in the hyperbolic regime 0.5 - 1.4 eV. (b) Anti-symmetric and (c) symmetric modes in a 10 nm thin film. The shading is given by  $\log_{10}|L^{\pm}|$  marked above the plot (for  $\text{Im}k_x = 0.01$ ).

plasmafrequency and maximize the out-of-plane dielectric function. This would lead to a smaller electric field fraction within the thin films and longer propagation lengths and lifetimes but worse confinement.

To avoid compromising confinement, it is necessary to lower the intrinsic ohmic losses of the materials. We have hypothesized that the reduced dimensionality of layered materials make it more likely for them to exhibit the special metallic band structure in which metallic bands are separated from other bands by finite energy gaps. By screening the layered halides we have already found the metastable 1T-GaCl<sub>2</sub> whose bandstructure is almost a perfect replica of the elusive loss-less metal (Fig. 6.12), however, it is unlikely that 1T-GaCl<sub>2</sub> is thermodynamically stable when taking into account other competing phases. A future study could screen for experimentally known layered materials to test the hypothesis and explore the existence conditions for these special band structure characters.

It was observed that the energy gap to the valence bands closed in 2H-TaS<sub>2</sub> when constructing the bulk crystal from the monolayer (Fig. 2 in paper). This should entail even lower density of states for scattering for monolayer H-TaS<sub>2</sub> compared to bulk 2H-TaS<sub>2</sub> and a future study could investigate the properties of monolayer H-TaS<sub>2</sub> with special focus on the consequences of the special band structures.

A waveguide medium like 2H-TaS<sub>2</sub> provides a way of guiding both photonic and electric signals in the same medium through its finite conductivity, SPPs and hyperbolic modes. It has been argued that this is necessary to achieve integrated electronic-

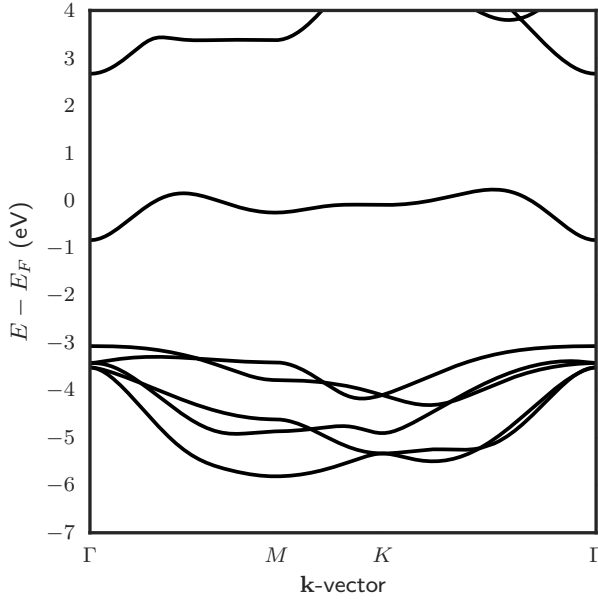


**Figure 6.12:** Band structure of 1T-GaCl<sub>2</sub>. It is stressed that this material is only meta-stable.

photonic circuits[1] and we believe that this kind of hybrid wave guide is a step in the right direction.

### 6.3 Paper III: Layered materials with hyperbolic light dispersion

Due to the lack of artificial structuring in natural hyperbolic materials, the limit on the achievable Purcell factor is set either by the distance of the dipole to the substrate or non-local effects that reduce the metallic screening for very short wavelengths (Sec. 2.5.1). We have investigated the importance of spatial dispersion by implementing the non-local effects in the dielectric function of our layered materials by

$$\varepsilon_{\parallel}(\omega, k_{\parallel}) = 1 - \frac{\omega_p^2}{\omega(\omega + i\eta) - \beta^2 k_{\parallel}^2} \quad (6.10)$$

$$\varepsilon_{\perp}(\omega) = \frac{\omega_p^2}{\omega(\omega + i\eta)}, \quad (6.11)$$

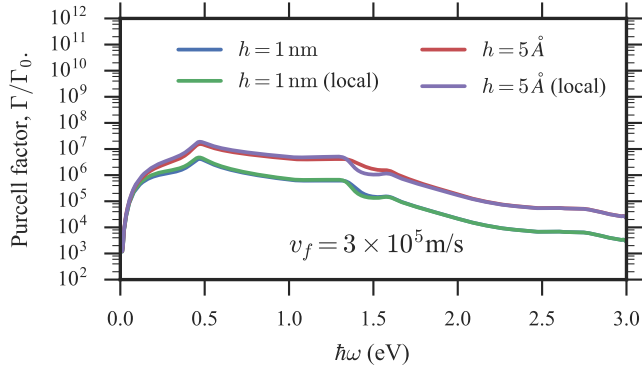


**Figure 6.13:** The Purcell factor calculated with and without spatial dispersion for varying distance between the dipole and the substrate.

where  $\beta = \sqrt{\frac{3}{5}}v_F$  with the fermi-velocity  $v_F$  [77]. Evident from the above expressions is that the wave-vector dependence is only included in the in-plane component of the dielectric function. This is due to the anticipation of a small out-of-plane Fermi velocity originating from the weak interlayer hybridization which is confirmed by inspecting the bandstructures of the layered materials presented in Paper II. Given that a hyperbolic response requires a negative in-plane dielectric function, it is clear from Eq. (6.10) that the main effect of the non-local effects is to limit the hyperbolic response to wave-vectors smaller than the characteristic non-local wave vector  $k_{nl} < \omega/\beta$ .

The importance of spatial dispersion on the Purcell factor is determined by the distance of the dipole to the substrate by the exponential term in the integrand of Eq. (2.61). For the specific case of 2H-TaS<sub>2</sub>, we accounted for the non-local effects by the model presented above using a fermi-velocity of  $3 \times 10^5$  m/s which was determined by inspecting the bandstructure of 2H-TaS<sub>2</sub>. The results are presented in Fig. 6.13. From these results it is concluded, that the effect of spatial dispersion is safely ignored.

EMT was employed to determine the hyperbolic regimes of heterostructures of the investigated layered materials. As argued in Paper I, EMT can break down for large layer thicknesses due to interference effects between multiply reflected beams as well as in the atomically thin layer limit, due to quantum mechanical hybridization effects at the interfaces. In Figure 6.14(a), we investigate the effects of interface hybridization on the dielectric function of doped graphene-boron nitride heterostructures when varying the number of layers of each component. The doping level is set to +0.5 eV in the graphene layers. In correspondence with Paper I, discrepancies are found between the predicted EMT dielectric function and the calculated dielectric functions. However, since the description of the hyperbolic regimes is mainly determined by the in-plane plasma frequency, which is fairly well-described by EMT, we conclude that

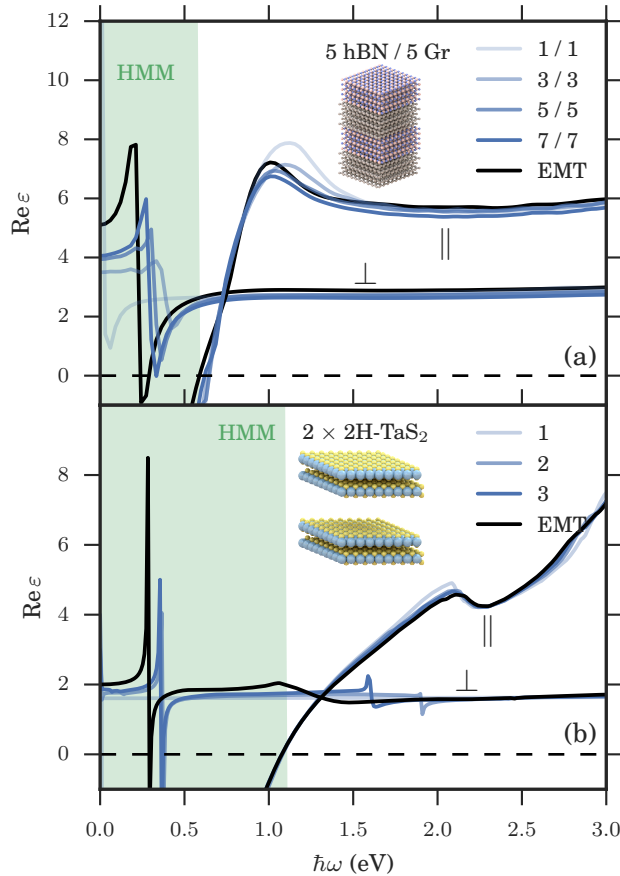


**Figure 6.14:** Effective medium theory for the dielectric function is tested from first principles by (a) assembling heterostructures composed graphene and hexagonal boron-nitride and (b) by analyzing the dielectric properties of multilayered 2H-TaS<sub>2</sub>.

the hyperbolic regimes are reasonably described by EMT.

The difference in electronic structure of graphene compared to the TMDs means that it is not clear whether these conclusions are valid in general. We have therefore tested our conclusions on heterostructures of 2H-TaS<sub>2</sub> and vacuum. The vacuum was needed since no other semi-conducting TMD matches the lattice constant of 2H-TaS<sub>2</sub>. It is however not expected to be important for the investigation of the accuracy of EMT. The results are presented in Figure 6.14(b) which ratifies the conclusions.

Figure 6.15(a) presents Purcell factors for a few of the metallic and one semi-

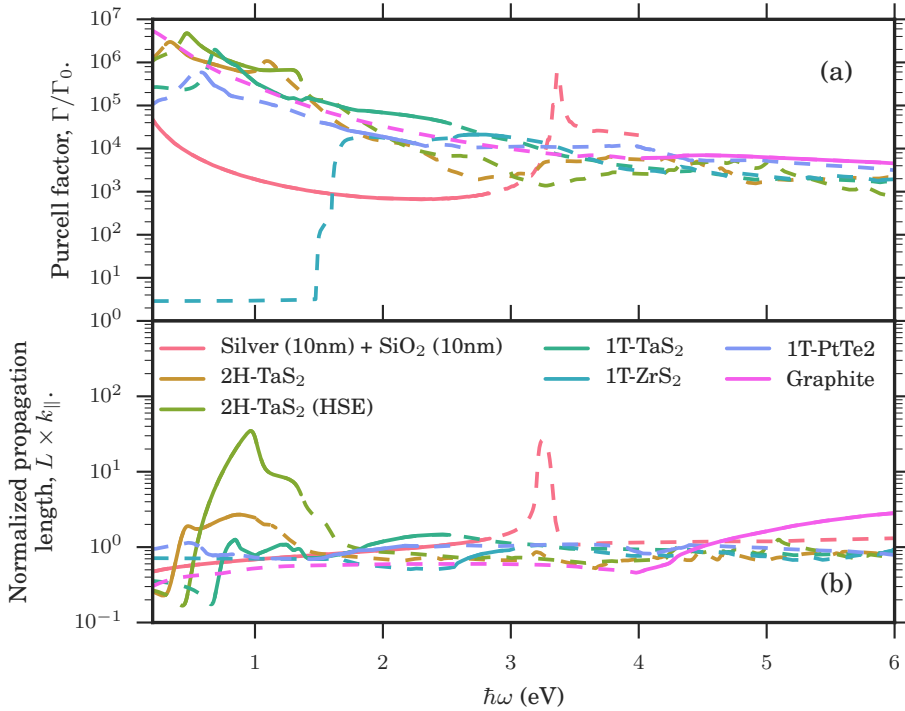


**Figure 6.15:** Purcell factors for some of the naturally hyperbolic materials compared with the silver-SiO<sub>2</sub> metamaterial. The full lines mark the hyperbolic regimes (as predicted by EMT for the metamaterial) and dashed lines are drawn if the materials are not hyperbolic.

conducting TMD compared to graphite and a silver-SiO<sub>2</sub> hyperbolic metamaterial. The hyperbolic regimes are marked by full lines, dashed lines mark metallic or elliptic regimes. The Purcell factor of semiconducting 1T-ZrS<sub>2</sub> is dominated by quenching above the band gap, i.e., non-radiative decay due to excitement of electron hole pairs (Sec. 2.5.1), and it is not possible to see a signature of the enhanced decay rate due to hyperbolic propagating modes in the hyperbolic regime ( $\sim 2.5 - 2.9$  eV). Similar results are obtained for graphite (shown) and the other semi-conducting TMDs (not shown). Below the band gap the Purcell factor only achieves a modest near unity value originating from reflection due to the real part of the dielectric function. The metallic TMDs in general show much larger Purcell factors for lower frequencies. Furthermore, clear signatures of the hyperbolic regimes, manifesting as shoulders or peaks in the Purcell factors, shows that quenching do not dominate the hyperbolic response of the metals for low frequencies in contrast to the semi-conducting hyperbolic materials. For higher frequencies, quenching from interband

transitions again dominate the Purcell factor of the metals.

Figure 6.15(b) shows the normalized propagation length through the hyperbolic material,  $k_{\parallel}/\text{Im } k_{\perp}$ . By comparing the results of 2H-TaS<sub>2</sub> with and without HSE (Sec. 6.2.4), it is clear that the origin of the long propagation lengths is its special bandstructure, since the only difference between these results are the size of the energy gaps surrounding the metallic bands. Furthermore, the effect of the crystal structure is highlighted if the results are compared to 1T-TaS<sub>2</sub> which has much smaller propagation lengths due to the wider conduction bands (Fig. 6.4(c)).

# CHAPTER 7

## Implementation

---

A considerable part of the work associated with this thesis has consisted of developing and optimizing code for the calculation of the optical properties of matter. This chapter goes into details with the important aspects of the code and the contributions that have been made. The most important contributions consist of implementing the optical response for metallic systems, reducing the computational costs by applying crystal symmetries and implementing the linear tetrahedron method for Brillouin zone integrals using Delaunay triangulated grids.

### 7.1 GPAW

The implementation has been performed in the electronic structure code GPAW[113]. GPAW implements the projector augmented wave (PAW) method [114, 115] for expansion of wavefunctions close to the atomic cores. This reduces the size of the basis sets needed to converge electronic structure calculations by replacing the strongly oscillating electronic wavefunctions close to the atomic cores by smoothly varying functions. This substitution is enabled by a well-defined transformation from 'smooth' to 'hard' wave functions which additionally means that the 'hard' wave functions can always be retrieved from their smooth counter parts.

### 7.2 Python

The implementation has primarily been written in Python. Python is a high-level programming language that provide many useful tools for the scientific community. It can, in some cases, have a large computational overhead compared to lower level languages like C and Fortran, however, this can typically be overcome by employing pre-compiled Python packages where time-consuming operations have been implemented in lower level languages interfaced with Python. SciPy is a specific Python package that provides many of the tools needed in the implementation of the response code, such as, Voronoi tessellation, Delaunay Triangulation and an efficient KDTree implementation. To implement those tools would have been time-consuming, and the programming effort was significantly reduced by employing these pre-made solutions.

### 7.3 Calculating the response functions

At a basic level, optical properties of matter are derived from the dielectric function as described in Chapter 2. In the RPA approximation the dielectric function is derived from the non-interacting density response function as shown in Chapter 3.3.

For the present purposes, the non-interacting density response function is presented as (Sec. 3.4)

$$\chi_{\mathbf{G},\mathbf{G}'}^0(\mathbf{q}, \omega) = \frac{1}{(2\pi)^3} \sum_{n,m} \int_{\text{BZ}} d\mathbf{k} \frac{f_{n\mathbf{k}} - f_{m\mathbf{k}+\mathbf{q}}}{\omega + i\eta + \epsilon_{n\mathbf{k}} - \epsilon_{m\mathbf{k}+\mathbf{q}}} \times \\ \langle n\mathbf{k} | e^{-i(\mathbf{q}+\mathbf{G})\cdot\mathbf{r}} | m\mathbf{k} + \mathbf{q} \rangle \langle m\mathbf{k} + \mathbf{q} | e^{i(\mathbf{q}+\mathbf{G}')\cdot\mathbf{r}'} | n\mathbf{k} \rangle. \quad (7.1)$$

This expression reveals the tasks that are involved in its calculation: A sum over bands and an integration over the Brillouin zone.

### 7.4 Linear tetrahedron method

A typical bottleneck in the calculation of the density response function is the Brillouin zone integral. The convergence of the integral depend on the specific material investigated, however, even for the optical properties of the simplest materials (with well-behaving integrands) they are slowly converging. To reconcile this with the well-known fact that GW total energy calculations converge comparably fast with a number of k-points[116, 117], we need to bring attention to the fact that frequency integrals of the screened interaction is taken in these methods, which typically converge faster. The large number of k-points needed for an accurate calculation of optical properties is thus related to the fact that we want the frequency resolved dielectric function rather than some integral of it.

The Brillouin zone integral is often approximated as a simple sum of the discretely sampled Brillouin Zone

$$\frac{1}{(2\pi)^3} \int_{\text{BZ}} d\mathbf{k} \rightarrow \frac{1}{\Omega} \sum_{\mathbf{k} \in \text{BZ}} \quad (7.2)$$

as assumed in Section 3.4. Given the fact that the k-point integration is a typical bottleneck for the calculation of the density response function other approximations for the integral has been explored previously. The linear tetrahedron method[118] is an example of a higher order approximation that interpolates the integrand between nearby k-points. In the linear tetrahedron method the volume of the Brillouin zone is filled with non-overlapping tetrahedrons, within which each eigenvalue is interpolated linearly. The division of the IBZ into tetrahedrons is done by a Delaunay triangulation[119]. SciPy contains the tools to compute such triangulations which is ultimately why this specific triangulation was chosen. By interpolating the eigenvalues between neighboring k-points it is possible to perform the k-point integrals analytically within each tetrahedron.

MacDonald, Vosko, and Coleridge [118] applied this method to response functions of similar form to the density response function, taking advantage of the spectral representation of the density response function given by

$$\chi^0(\omega) = \lim_{\eta \rightarrow 0} \int_{-\infty}^{\infty} d\omega' \frac{A(\omega')}{\omega - \omega' + i\eta} \quad (7.3)$$

where  $A(\omega) = \text{Im}\chi^0(\omega)$  is known as the spectral function and is given by

$$A_{\mathbf{G}, \mathbf{G}'}(\mathbf{q}, \omega) = (-i\pi) \frac{V}{(2\pi)^3} \sum_{n,m} \int_{\text{BZ}} d\mathbf{k} (f_{n\mathbf{k}} - f_{m\mathbf{k}+\mathbf{q}}) \delta(\omega + \omega_{nm}(\mathbf{k})) \times \\ \langle n\mathbf{k} | e^{-i(\mathbf{q}+\mathbf{G}) \cdot \mathbf{r}} | m\mathbf{k} + \mathbf{q} \rangle \langle m\mathbf{k} + \mathbf{q} | e^{i(\mathbf{q}+\mathbf{G}') \cdot \mathbf{r}'} | n\mathbf{k} \rangle, \quad (7.4)$$

where  $\omega_{nm}(\mathbf{k}) = \epsilon_{n\mathbf{k}} - \epsilon_{m\mathbf{k}+\mathbf{q}}$ . The appearance of delta-functions makes the spectral function a nicer quantity to work with, since it turns the Brillouin zone volume integral into surface integrals over constant frequency surfaces. MacDonald, Vosko, and Coleridge [118] showed that the spectral function could be expressed as a sum over all tetrahedrons as

$$A(\omega) = \sum_{i=1}^{N_{\text{tet}}} V^i g^i \sum_{k=1}^4 I_k^i F_k^i \quad (7.5)$$

where we have suppressed all arguments to the spectral function other than the frequency for simplicity. The inner  $k$ -sum runs over all vertices of a single tetrahedron,  $V^i$  is the volume of the  $i$ 'th tetrahedron,  $g^i$  is the contribution to the joint density of states of the  $i$ 'th tetrahedron,  $I_k^i$  a weighted average of the integrand of the spectral function evaluated at the vertices  $F_k^i$

$$F_{\mathbf{k}}^i = (f_{n\mathbf{k}} - f_{m\mathbf{k}+\mathbf{q}}) \langle n\mathbf{k} | e^{-i(\mathbf{q}+\mathbf{G}) \cdot \mathbf{r}} | m\mathbf{k} + \mathbf{q} \rangle \langle m\mathbf{k} + \mathbf{q} | e^{i(\mathbf{q}+\mathbf{G}') \cdot \mathbf{r}'} | n\mathbf{k} \rangle, \quad (7.6)$$

and the outer  $i$ -sum runs over all tetrahedrons. In practice, this is implemented as a point summation over all  $k$ -point with frequency dependent weights to ease parallelization.

The results obtained by MacDonald are reiterated here for reference. Given a tetrahedron with vertices at  $\mathbf{k}_1$ ,  $\mathbf{k}_2$ ,  $\mathbf{k}_3$  and  $\mathbf{k}_4$ , ordered after increasing transition frequencies, where the transition energies at each vertex are given by  $\omega_1$ ,  $\omega_2$ ,  $\omega_3$  and  $\omega_4$ , the contribution to the spectral function can be divided into five cases depending on the frequency  $\omega$ :

**Case (i)**  $\omega < \omega_1$

The tetrahedron does not contribute to the integral.

**Case (ii)**  $\omega_1 < \omega < \omega_2$

In this case we have,

$$f_{n,m} = \frac{\omega - \omega_m}{\omega_n - \omega_m} \quad (7.7)$$

$$g^i = \frac{3n^i}{\omega - \omega_1} \quad (7.8)$$

$$n^i = f_{2,1}f_{3,1}f_{4,1} \quad (7.9)$$

$$I_1^i = \frac{1}{3}(f_{1,2} + f_{1,3} + f_{1,4}) \quad (7.10)$$

$$I_k^i = \frac{f_{k,1}}{3}, \quad k = 2, 3, 4. \quad (7.11)$$

**Case (iii)**  $\omega_2 < \omega < \omega_3$

$$g^i = \frac{3}{\Delta_{4,1}}(f_{2,3}f_{3,1} + f_{3,2}f_{2,4}) \quad (7.12)$$

$$I_1^i = \frac{f_{1,4}}{3} + \frac{f_{1,3}f_{3,1}f_{2,3}}{g^i\Delta_{4,1}} \quad (7.13)$$

$$I_2^i = \frac{f_{2,3}}{3} + \frac{f_{2,4}^2f_{3,2}}{g^i\Delta_{4,1}} \quad (7.14)$$

$$I_3^i = \frac{f_{3,2}}{3} + \frac{f_{3,1}^2f_{2,3}}{g^i\Delta_{4,1}} \quad (7.15)$$

$$I_4^i = \frac{f_{4,1}}{3} + \frac{f_{4,2}f_{2,4}f_{3,2}}{g^i\Delta_{4,1}} \quad (7.16)$$

$$I_k^i = \frac{1}{3}f_{k,1}, \quad k = 2, 3, 4 \quad (7.17)$$

$$\Delta_{n,m} = \omega_n - \omega_m \quad (7.18)$$

**Case (iv)**  $\omega_3 < \omega < \omega_4$

$$g^i = \frac{3(1 - n^i)}{\omega_4 - \omega} \quad (7.19)$$

$$n^i = 1 - f_{2,1}f_{3,1}f_{4,1} \quad (7.20)$$

$$I_k^i = \frac{f_{k,4}}{3}, \quad k = 1, 2, 3 \quad (7.21)$$

$$I_1^i = \frac{1}{3}(f_{4,1} + f_{4,2} + f_{4,3}). \quad (7.22)$$

**(iv)**  $\omega_4 < \omega$

The tetrahedron do not contribute to the integral.

These expressions have been implemented in GPAW for the calculation of the density response function. Examples of the convergence of the method was presented in Section 6.1.

## 7.5 Symmetries of the dielectric function

The computational effort spent on calculating the dielectric function for realistic systems can be substantial, and as argued a large part of the effort is spent in the calculation of the Brillouin zone integral. In addition to the linear tetrahedron interpolation scheme, it is possible to reduce the computational complexity of the integrals by considering the symmetries that the integrand of the spectral function possess.

Symmetries are in practice represented by operators working on real space coordinates. The inversion operator, for example, is defined as the operator that inverts coordinates, i.e.,  $\hat{U}f(\mathbf{r}) = f(\hat{U}\mathbf{r}) = f(-\mathbf{r})$ . If a symmetry operator commutes with the Hamiltonian

$$\hat{U}\hat{H}\Psi = \hat{H}(\hat{U}\Psi) = E(\hat{U}\Psi), \quad (7.23)$$

then given a solution  $\Psi$  with eigenvalue  $E$  of Schrödinger's equation entails that  $\hat{U}\Psi$  will also be a solution with eigenvalue  $E$ . The existence of symmetries makes some  $\mathbf{k}$ -points equivalent. To see this we use Bloch's theorem which states that the translational invariance leads to the following form of eigenstates

$$\psi(\mathbf{r}) = \psi_{n\mathbf{k}}(\mathbf{r}) = e^{-i\mathbf{k}^T\mathbf{r}}u_{n\mathbf{k}}(\mathbf{r}), \quad (7.24)$$

where  $\mathbf{k} \in \text{BZ}$  is the Bloch momentum and  $n$  is a band index. The Bloch states transform under symmetry operations according to

$$\hat{U}\psi_{n\mathbf{k}}(\mathbf{r}) = \psi_{n\mathbf{k}}(\hat{U}\mathbf{r}) = \hat{U}\left(e^{-i\mathbf{k}^T\mathbf{r}}u_{n\mathbf{k}}(\mathbf{r})\right) = e^{-i\mathbf{k}^T\hat{U}\mathbf{r}}u_{n\mathbf{k}}(\hat{U}\mathbf{r}) \quad (7.25)$$

$$= e^{-i(\hat{U}^{-1}\mathbf{k})^T\mathbf{r}}u_{n\mathbf{k}}(\hat{U}\mathbf{r}) = e^{-i(\hat{U}^{-1}\mathbf{k})^T\mathbf{r}}u_{n\mathbf{k}}(\hat{U}\mathbf{r}) \quad (7.26)$$

$$= \psi_{n\hat{U}^{-1}\mathbf{k}}(\mathbf{r}) \quad (7.27)$$

where we have used the unitary property  $U^T = U^{-1}$ . The result shows that wavefunctions at different  $\mathbf{k}$ -points  $\mathbf{k}' = \hat{U}^{-1}\mathbf{k}$  can be related by crystal symmetries. For practical applications it is useful to summarize the above result as

$$\psi_{n\hat{U}\mathbf{k}}(\mathbf{r}) = \psi_{n\mathbf{k}}(\hat{U}^{-1}\mathbf{r}). \quad (7.28)$$

To see how symmetries are employed to reduce the Brillouin zone integration the pair density is written as

$$M_{\mathbf{G}}^{nm}(\mathbf{k}, \mathbf{q}) = \int d\mathbf{r} \psi_{n\mathbf{k}}^*(\mathbf{r})e^{-i(\mathbf{q}+\mathbf{G})\cdot\mathbf{r}}\psi_{m\mathbf{k}+\mathbf{q}}(\mathbf{r}). \quad (7.29)$$

If a symmetry operator satisfying  $\hat{U}\mathbf{k} = \mathbf{k}'$  exists then

$$M_{\mathbf{G}}^{nm}(\mathbf{k}', \mathbf{q}) = M_{\mathbf{G}}^{nm}(\hat{U}\mathbf{k}, \mathbf{q}) \quad (7.30)$$

$$= \int d\mathbf{r} \psi_{n\hat{U}\mathbf{k}}^*(\mathbf{r})e^{-i(\mathbf{q}+\mathbf{G})\cdot\mathbf{r}}\psi_{m\hat{U}\mathbf{k}+\mathbf{q}}(\mathbf{r}) \quad (7.31)$$

To make further progress it is assumed that  $\hat{U}\mathbf{q} = \mathbf{q}$ ,

$$M_{\mathbf{G}}^{nm}(\mathbf{k}', \mathbf{q}) = \int d\mathbf{r} \psi_{n\hat{U}\mathbf{k}}^*(\mathbf{r}) e^{-i(\mathbf{q}+\mathbf{G})\cdot\mathbf{r}} \psi_{m\hat{U}(\mathbf{k}+\mathbf{q})}(\mathbf{r}) \quad (7.32)$$

$$= \int d\mathbf{r} \psi_{n\mathbf{k}}^*(\hat{U}^T \mathbf{r}) e^{-i(\mathbf{q}+\mathbf{G})\cdot\mathbf{r}} \psi_{m\mathbf{k}+\mathbf{q}}(\hat{U}^T \mathbf{r}). \quad (7.33)$$

Letting  $\hat{U}^T \mathbf{r} \rightarrow \mathbf{r}'$  leads to,

$$M_{\mathbf{G}}^{nm}(\mathbf{k}', \mathbf{q}) = \int d\mathbf{r} \psi_{n\mathbf{k}}^*(\mathbf{r}) e^{-i(\mathbf{q}+\mathbf{G})\cdot\hat{U}^{-T}\mathbf{r}} \psi_{m\mathbf{k}+\mathbf{q}}(\mathbf{r}) \quad (7.34)$$

$$= \int d\mathbf{r} \psi_{n\mathbf{k}}^*(\mathbf{r}) e^{-i(\mathbf{q}+\hat{U}^{-1}\mathbf{G})\cdot\mathbf{r}} \psi_{m\mathbf{k}+\mathbf{q}}(\mathbf{r}) \quad (7.35)$$

$$= M_{\hat{U}^{-1}\mathbf{G}}^{nm}(\mathbf{k}, \mathbf{q}) \quad (7.36)$$

This result shows that the pair-densities at  $\mathbf{k}'$  corresponds to a reshuffling of the pair-densities at  $\mathbf{k}$ . The assumption  $\hat{U}\mathbf{q} = \mathbf{q}$  corresponds to restricting applicable crystal symmetries to the so-called 'little group' of  $\mathbf{q}$ .

In the optical limit  $\mathbf{q} \rightarrow 0$  all crystal symmetries can be applied as shown below. In this case the momentum matrix elements are written as

$$N^{nm}(\mathbf{k}) = \int d\mathbf{r} \psi_{n\mathbf{k}}(\mathbf{r}) \nabla \psi_{m\mathbf{k}}(\mathbf{r}) \quad (7.37)$$

and it is assumed that there exist a crystal symmetry such that  $\hat{U}\mathbf{k} = \mathbf{k}'$ . The resulting relationship of the momentum matrix elements is

$$N^{nm}(\mathbf{k}') = N^{nm}(\hat{U}\mathbf{k}) \quad (7.38)$$

$$= \int d\mathbf{r} \psi_{n\hat{U}\mathbf{k}}^*(\mathbf{r}) \nabla \psi_{m\hat{U}\mathbf{k}}(\mathbf{r}) \quad (7.39)$$

$$= \int d\mathbf{r} \psi_{n\mathbf{k}}^*(\hat{U}^{-1}\mathbf{r}) \nabla \psi_{m\mathbf{k}}(\hat{U}^{-1}\mathbf{r}) \quad (7.40)$$

$$= \int d\mathbf{r} \psi_{n\mathbf{k}}^*(\mathbf{r}) \hat{U} \nabla \psi_{m\mathbf{k}}(\mathbf{r}) \quad (7.41)$$

$$= \hat{U} N^{nm}(\mathbf{k}) \quad (7.42)$$

To apply the symmetry operations the density response function is written as

$$\chi_{\mathbf{G}\mathbf{G}'}(\omega, \mathbf{q}) = \frac{2}{\Omega} \sum_{nm\mathbf{k}} \Delta f_{\mathbf{k}}^{nm} \Delta \varepsilon_{\mathbf{k}}^{nk} M_{\mathbf{G}}^{nm}(\mathbf{k}, \mathbf{q}) (M_{\mathbf{G}'}^{nm}(\mathbf{k}, \mathbf{q}))^* \quad (7.43)$$

where  $\Delta f_{\mathbf{k}}^{nm} = f_{n\mathbf{k}} - f_{m\mathbf{k}+\mathbf{q}}$ ,  $\Delta \varepsilon_{\mathbf{k}}^{nk} = \frac{1}{\omega+i\eta+\varepsilon_{n\mathbf{k}}-\varepsilon_{m\mathbf{k}+\mathbf{q}}} - \frac{1}{\omega+i\eta-(\varepsilon_{n\mathbf{k}}-\varepsilon_{m\mathbf{k}+\mathbf{q}})}$  and  $M_{\mathbf{G}}^{nm}(\mathbf{k}, \mathbf{q}) = \langle n\mathbf{k} | e^{-i(\mathbf{q}+\mathbf{G})\cdot\mathbf{r}} | m\mathbf{k} + \mathbf{q} \rangle$ . Regarding the matrix elements as a vector in  $\mathbf{G}$  the action of a symmetry operator can be written as

$$(\underline{\underline{\mathbf{U}}} M^{nm}(\mathbf{k}, \mathbf{q}))_{\mathbf{G}} = M_{\hat{U}^{-1}\mathbf{G}}^{nm}(\mathbf{k}, \mathbf{q}). \quad (7.44)$$

Writing the density response function as a matrix in  $\mathbf{G}, \mathbf{G}'$  then results in

$$\underline{\underline{\chi}}(\omega, \mathbf{q}) = \frac{2}{\Omega} \sum_{nm\mathbf{k}} \Delta f_{\mathbf{k}}^{nm} \Delta \varepsilon_{\mathbf{k}}^{nm} \mathbf{M}^{nm}(\mathbf{k}, \mathbf{q}) \mathbf{M}^{nm}(\mathbf{k}, \mathbf{q})^\dagger.$$

A common notion in group theory is the star of a particular k-point, which denotes the set of symmetry related k-points obtained by employing all symmetries on some k-point. Dividing the above k-point sum into a sum over stars we can write

$$\underline{\underline{\chi}}(\omega, \mathbf{q}) = \frac{2}{\Omega} \sum_{nm\star} \Delta f_{\star}^{nm} \Delta \varepsilon_{\star}^{nm} \sum_{\mathbf{k} \in \star} \mathbf{M}^{nm}(\mathbf{k}, \mathbf{q}) \mathbf{M}^{nm}(\mathbf{k}, \mathbf{q})^\dagger. \quad (7.45)$$

Introducing the symmetry operators by Eq. (7.44), and taking into account the special case that high-symmetry k-points are mapped into themselves by some symmetry operations by introducing the number of k-points in each star as  $N_\star$ , the density response function reduces to

$$\underline{\underline{\chi}}(\omega, \mathbf{q}) = \frac{2}{\Omega N_U} \sum_U \underline{\underline{\mathbf{U}}} \left( \sum_{nm\star} \Delta f_{\star}^{nm} N_\star \Delta \varepsilon_{\star}^{nm} \mathbf{M}^{nm}(\star, \mathbf{q}) \mathbf{M}^{nm}(\star, \mathbf{q})^\dagger \right) \underline{\underline{\mathbf{U}}}^\dagger. \quad (7.46)$$

where  $N_U$  is the number of symmetry operators in the little group of  $\mathbf{q}$  (i.e. the character of the group). From this expression we are inspired to define the irreducible  $\underline{\underline{\chi}}$

$$\underline{\underline{\chi}}^{\text{irred.}}(\omega, \mathbf{q}) = \frac{2}{\Omega N_U} \sum_{nm\star} \Delta f_{\star}^{nm} N_\star \Delta \varepsilon_{\star}^{nm} \mathbf{M}^{nm}(\star, \mathbf{q}) \mathbf{M}^{nm}(\star, \mathbf{q})^\dagger. \quad (7.47)$$

The density response function can then be obtained as

$$\underline{\underline{\chi}} = \sum_U \underline{\underline{\mathbf{U}}} \underline{\underline{\chi}}^{\text{irred.}} \underline{\underline{\mathbf{U}}}^\dagger. \quad (7.48)$$

In the case of the tetrahedron method, where no tetrahedrons are mapped into themselves, the irreducible density response function is simply

$$\underline{\underline{\chi}}^{\text{irred.}}(\omega, \mathbf{q}) = \frac{2}{\Omega} \sum_{T \in \text{IBZ}_{\mathbf{q}}} \underline{\underline{\chi}}_T(\omega, \mathbf{q}) \quad (7.49)$$

where  $\underline{\underline{\chi}}_T$  is the contribution to the density response function from a single tetrahedron. Eq. (7.48) is of practical importance because it shows that the crystal symmetries can be implemented as a simple post-processing of the irreducible density response function. This significantly simplifies the implementation of the symmetry operations and essentially boils down to determining the mapping of reciprocal lattice vectors under symmetry operators.

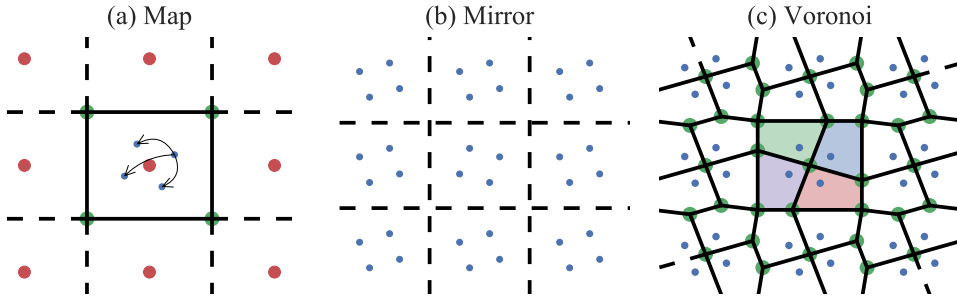


**Figure 7.1:** Example of the algorithm used for determining the IBZ for the case of a material with 4-fold symmetry. (a) A random point is mapped out by the symmetry operations. (b) The point are mirrored in the BZ edges. (c) The Voronoi diagram is calculated. The colored areas are all valid choices for the irreducible zone.

## 7.6 The irreducible Brillouin zone

When employing symmetries, the k-point integral of the density response function is taken over the irreducible Brillouin zone (IBZ) of the little group of  $\mathbf{q}$ . This section details the general algorithm implemented for determining the IBZ given any set of symmetry operators in any crystal. Furthermore, an algorithm for folding out the lattice IBZ to the crystal IBZ is explained which is used to avoid skewed IBZs when no mirror planes are present in the symmetry group.

The most common sampling of the BZ used in electronic structure calculations is the Monkhorst-Pack construction [120]:

$$\text{BZ} = \{\mathbf{k} \mid k_1 \mathbf{b}_1 + k_2 \mathbf{b}_2 + k_3 \mathbf{b}_3, k_1, k_2, k_3 \in [-1/2, 1/2[ \} \quad (7.50)$$

where  $\mathbf{b}_{1,2,3}$  are reciprocal lattice vectors. This construction is normally sufficient, but suffers from the fact that it need not be invariant under crystal symmetry transformations, which can cause difficulties if the k-point integral is reduced using crystal symmetries.

To avoid this problem we employ the Wigner-Seitz construction of the Brillouin zone, which is invariant under crystal symmetries[121]. In this construction, the Brillouin zone is defined as the volume of points closer to the origin than any other reciprocal lattice vector, which is actually a special case of the so-called Voronoi diagram in mathematics. This fact makes it exceedingly easy to determine the BZ, since packages for calculating the Voronoi diagram for a collection of points already exist.

The tools provided by Python and its associated packages also makes it easier to determine the IBZ, however, it is not quite as straight-forward as calculating the BZ. For the point summation integration method it is not necessary to care about how the

irreducible k-points are located throughout the BZ, since they are not related to their neighbouring points, so the irreducible k-points are simply determined by picking one random k-point of out each k-point star (see the previous section for definition of a star). This is clearly not true in the tetrahedron method where it is important that the irreducible k-points are not chosen randomly but rather chosen to be in the vicinity of each other. This is further complicated by the fact that there can exist many choices for the IBZ.

The implemented algorithm for determining the IBZ is explained pictorially in Figure 7.1 for the case of a two-dimensional BZ with a 4-fold rotational symmetry and the following paragraph explains the logic of the algorithm.

By picking a random point and mapping it around the first BZ using the symmetry operators (Fig. 7.1(a)) it is possible to determine the positions in reciprocal space that is described by the initial random point. The irreducible zone can then be thought of as the neighbourhood of this initial point, which in practice is obtained from the Voronoi diagram of the mapped set of points constrained to the first BZ. The constraint can be implemented by mirroring the mapped points in the boundaries of the BZ (Fig. 7.1(b)) and taking the Voronoi diagram as shown in Figure 7.1(c) where the possible irreducible zones are shaded by different colors.

For materials with no mirror planes in their symmetry group, the algorithm above can result in irregularly shaped IBZs, as evident from 7.1(c) where the IBZ zone edges are dependent on the random point chosen initially. This is not a fundamental problem but it can lead to irregularly shaped tetrahedrons which should be avoided if possible, as it is detrimental to the performance of the linear tetrahedron method. The user is therefore offered to build the irreducible in units of the IBZ of the lattice group, which usually is of a more regular shape. The construction of the IBZ of the lattice group is performed using the algorithm above, and then folded out to the irreducible zone of the crystal group.

Again there is a degree of arbitrariness as to how this unfolding can be performed. If the lattice symmetry group is  $G_L$  and the crystal symmetry group is  $G_C$  then this folding is in practice performed by partitioning  $G_L$  in cosets of  $G_C$ , e.g., if the character of  $G_L$  is 8 and the character of  $G_C$  is 4 due to a broken mirror symmetry  $\Gamma_M$ , then the lattice group can be regarded as two cosets of the crystal group  $\{G_C, G_C\Gamma_M\}$ . The mapping of the IBZ of  $G_L$  to the IBZ of  $G_C$  is then obtained by choosing one operator from each of the cosets. To ensure that the mapped IBZ is not disjoint, all possible mappings are tested and only mappings that minimize the IBZ volume are accepted. Two operators  $G_1, G_2$  of  $G_L$  belong to the same right coset of  $G_C$  if and only if  $G_1^{-1}G_2 \in G_C$  which provides an easy way of determining the right cosets mentioned above. Fig. 7.2 show an example of this algorithm in practice for the same case of a material with a 4-fold symmetry from, where the result is seen to conform more nicely with the lattice IBZ as opposed to Fig. 7.1(c).

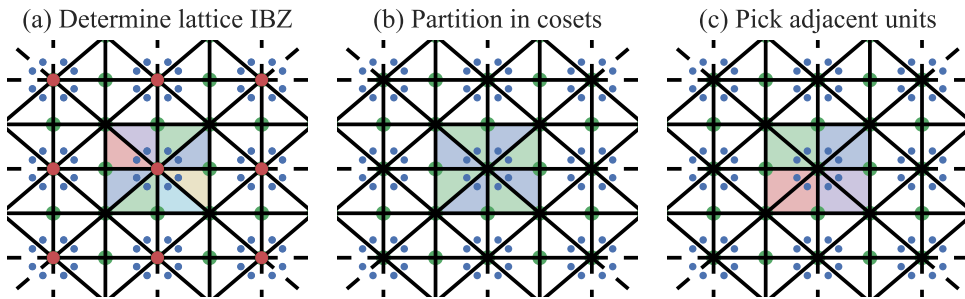


**Figure 7.2:** Example of the algorithm used for folding the lattice IBZ out to the crystal IBZ. Starting from (a) the lattice IBZ, (b) the lattice group is partitioned into cosets (shaded by green and blue) of the crystal group from which (c) the crystal IBZ can be obtained by picking adjacent units in each coset. In (c) each shaded region indicates a valid IBZ.

# Conclusion

---

In this thesis we have considered the properties of layered materials for optical applications. Compared to two-dimensional and three-dimensional materials layered materials can be thought of as an intermediate of the two; the materials are not strictly two-dimensional but do inherit some properties of their two-dimensional equivalents. The focus of the thesis have been on the nano-optical properties of the layered materials, in particular their properties in plasmonic and metamaterial applications.

By investigating the dielectric properties of graphene-hexagonal boron nitride heterostructures we have shown that the effective medium theory approach is limited in its validity for atomically thin components. To remedy this deficiency we propose an extension of effective medium theory which takes into account the changed electronic properties at the interfaces of the heterostructure and show that this extension entails an improved description of the heterostructure properties.

We have shown how the special bandstructure of some layered materials like 2H-TaS<sub>2</sub> might lead to a suppression of the optical losses due to a reduction in the density of states for scattering. The special bandstructures are characterized by an intermediate metallic band surrounded finite energy gaps which resemble the 'elusive loss-less metal' model bandstructure[63]. We show that the constant relaxation rate approximation for the optical losses is not a good approximation for these materials and propose a simple model based on the joint density of states to account for a reduction in the density of states for scattering. Our results gives hope to the future of plasmonics by showing that metals with such exotic bandstructures do not solely belong to the realm of theoretical physics. These discoveries could motivate future investigations of the existence conditions for these special bandstructures and in particular test the hypothesis given in one of the papers that the band structure character is related to the low-dimensional character of the materials.

Based upon the principle of minimizing the density of states for scattering we propose a new class of layered materials consisting of mixtures of transition metal, chalcogen and halogen atoms which significantly reduce the optical losses. We show that these metals might find application as thin-film wave guides where they are expected to show superior lifetimes and comparable propagation lengths compared to silver. Additionally, layered materials might in fact be more suited for thin film fabrication since their internal layering makes it easier to minimize surface roughness and we expect out discoveries will motivate further research.

We have shown that layered materials generally are natural hyperbolic materials,

due to their intrinsic crystal anisotropy, that is likely to lead to a scenario where the signs of the in-plane and out-of-plane dielectric response differ sign. Furthermore, we show that a consequence of the diverse electronic properties of the TMDs the hyperbolic spectral ranges span frequencies from the infrared to the UV. Possibly, the most intriguing property of layered and 2D materials is their ability to form heterostructures with virtually any 2D material, and we show how heterostructuring can help to fine-tune the hyperbolic responses to practically any frequency regime. Finally, we have shown that the lack of internal structuring in natural hyperbolic materials lead to Purcell factors that are orders of magnitudes greater than layered hyperbolic metamaterials.

# CHAPTER 9

## Hull energies and HOF for MXY compounds

---

Here we present the calculated HOF and energy the convex hull of competing phases for all the MXY compounds.

Formula	Hull (eV)	HOF (eV)	Formula	Hull (eV)	HOF (eV)
HfClO	-27.84	-28.58	ZrBrO	-26.50	-27.45
HfClS	-19.78	-19.66	TiBrS	-14.77	-15.69
HfClSe	-18.14	-17.62	TiBrSe	-13.44	-13.78
TiClO	-24.50	-28.05	ZrBrSe	-17.16	-16.55
TiClSe	-16.09	-16.58	ZrBrS	-18.66	-18.55
ZrClO	-28.13	-30.32	HfIO	-22.30	-22.35
TiClS	-17.43	-18.51	HfISe	-12.60	-12.01
ZrClSe	-18.79	-19.31	TiIO	-19.63	-21.40
ZrClS	-20.29	-21.29	HfIS	-14.24	-14.05
HfBrO	-23.43	-25.64	ZrIO	-23.08	-24.29
HfBrSe	-13.72	-14.78	TiIS	-12.57	-12.90
HfBrS	-15.36	-16.94	ZrIS	-15.24	-15.87
TiBrO	-21.84	-24.93	TiISe	-11.23	-10.99
			ZrISe	-13.74	-13.89

**Table 9.1:** Calculated heat of formation and hull energies for chalcogen-halogen mixtures..



# Bibliography

---

- [1] Ekmel Ozbay. “Plasmonics: Merging Photonics and Electronics at Nanoscale Dimensions”. In: *Science* 311.5758 (2006), pages 189–193. DOI: 10.1126/science.1114849.
- [2] Harry a. Atwater. “The Promise of Plasmonics”. In: *Scientific American* 296.4 (2007), pages 56–62. DOI: 10.1038/scientificamerican0407-56.
- [3] Jacob B. Khurgin. “How to deal with the loss in plasmonics and metamaterials”. In: *Nature Nanotechnology* 10.1 (2015), pages 2–6. DOI: 10.1038/nnano.2014.310. arXiv: 1411.6577.
- [4] Alexander Poddubny et al. “Hyperbolic metamaterials”. In: *Nature Photonics* 7.12 (2013), pages 948–957. DOI: 10.1038/nphoton.2013.243.
- [5] A K Geim and K.S. Novoselov. “The rise of graphene”. In: *Nature Mater.* 6.3 (2007), pages 183–191.
- [6] Mingsheng Xu et al. “Graphene-Like Two-Dimensional Materials”. In: *Chemical Reviews* 113.5 (May 2013), pages 3766–3798. DOI: 10.1021/cr300263a.
- [7] Surbhi Lal, Stephan Link, and Naomi J. Halas. “Nano-optics from sensing to waveguiding”. In: *Nature Photonics* 1.11 (November 2007), pages 641–648. DOI: 10.1038/nphoton.2007.223.
- [8] Lukas Novotny and Bert Hecht. *Principles of Nano-Optics*. Second edi. 2012.
- [9] Heinz Raether. *Surface Plasmons on Smooth and Rough Surfaces and on Gratings*. Springer-Verlag, 1986.
- [10] Stefan A. Maier. *Plasmonics: Fundamentals and applications*. 2007, pages 1–223. DOI: 10.1007/0-387-37825-1. arXiv: 0405528 [cond-mat].
- [11] G. V. Eleftheriades and K. G. Balmain. *Negative-Refractive Metamaterials*. IEEE, 2005.
- [12] Nader Engheta and Richard W. Ziolkowski. *Metamaterials Physics and Engineering Explorations*. 2006.
- [13] Vladimir M. Shalaev. “Optical negative-index metamaterials”. In: *Nature Photonics* 1.1 (January 2007), pages 41–48. DOI: 10.1038/nphoton.2006.49.
- [14] W Cai and V Shalaev. *Optical metamaterials: fundamentals and applications Vol. 10*. Berlin, Germany: Springer, 2010. DOI: 10.1007/978-1-4419-1151-3.

- [15] William L Barnes, Alain Dereux, and Thomas W Ebbesen. “Surface plasmon subwavelength optics”. In: *Nature* 424.6950 (August 2003), pages 824–830.
- [16] Stefan A. Maier and Harry A. Atwater. *Plasmonics: Localization and guiding of electromagnetic energy in metal/dielectric structures*. 2005. DOI: 10.1063/1.1951057.
- [17] Viktor G Veselago. “The electrodynamics of substances with simultaneously negative values of  $\epsilon$  and  $\mu$ ”. In: *Soviet Physics Uspekhi* 10.4 (April 1968), pages 509–514. DOI: 10.1070/PU1968v010n04ABEH003699.
- [18] Søren Raza et al. “Nonlocal optical response in metallic nanostructures”. In: *Journal of Physics: Condensed Matter* 27.18 (2015), page 183204.
- [19] Lorenzo Ferrari et al. “Hyperbolic metamaterials and their applications”. In: *Progress in Quantum Electronics* 40 (2015), pages 1–40. DOI: 10.1016/j.pquantelec.2014.10.001.
- [20] K S Novoselov et al. “Two-dimensional atomic crystals”. In: *Proceedings of the National Academy of Sciences of the United States of America* 102.30 (2005), pages 10451–10453. DOI: 10.1073/pnas.0502848102. arXiv: 0503533 [cond-mat].
- [21] Jonathan N Coleman et al. “Two-Dimensional Nanosheets Produced by Liquid Exfoliation of Layered Materials”. In: *Science* 331.6017 (2011), pages 568–571. DOI: 10.1126/science.1194975.
- [22] K S Novoselov et al. “Electric Field Effect in Atomically Thin Carbon Films”. In: *Science* 306.5696 (2004), pages 666–669. DOI: 10.1126/science.1102896.
- [23] K S Novoselov et al. “Two-dimensional gas of massless Dirac fermions in graphene”. In: *Nature* 438.7065 (November 2005), pages 197–200.
- [24] A. H. Castro Neto et al. “The electronic properties of graphene”. In: *Reviews of Modern Physics* 81.1 (2009). DOI: 10.1103/RevModPhys.81.109. arXiv: 0709.1163v2.
- [25] A H Castro Neto and K Novoselov. “Two-Dimensional Crystals: Beyond Graphene”. In: *Materials Express* 1.1 (2011).
- [26] Fengnian Xia et al. “Two-dimensional material nanophotonics”. In: *Nature Photonics* 8.12 (November 2014), pages 899–907. DOI: 10.1038/nphoton.2014.271.
- [27] J A Wilson and A D Yoffe. “The transition metal dichalcogenides discussion and interpretation of the observed optical, electrical and structural properties”. In: *Advances in Physics* 18.73 (May 1969), pages 193–335. DOI: 10.1080/00018736900101307.
- [28] Manish Chhowalla et al. “The chemistry of two-dimensional layered transition metal dichalcogenide nanosheets.” In: *Nature chemistry* 5.4 (2013), pages 263–75. DOI: 10.1038/nchem.1589. arXiv: 1205.1822.

- [29] Qing Hua Wang et al. “Electronics and optoelectronics of two-dimensional transition metal dichalcogenides.” In: *Nature nanotechnology* 7.11 (2012), pages 699–712. DOI: 10.1038/nnano.2012.193.
- [30] A K Geim and I V Grigorieva. “Van der Waals heterostructures”. In: *Nature* 499.7459 (July 2013), pages 419–425.
- [31] Jiajie Pei et al. “Producing air-stable monolayers of phosphorene and their defect engineering”. In: *Nature Communications* 7 (January 2016), page 10450.
- [32] Achim Woessner et al. “Highly confined low-loss plasmons in graphene–boron nitride heterostructures”. In: *Nature Materials* 14.4 (April 2015), pages 421–425.
- [33] Stefan A. Maier. “Plasmonics: The Promise of Highly Integrated Optical Devices”. In: *IEEE Journal of Selected Topics in Quantum Electronics* 12.6 (2006), pages 1671–1677. DOI: 10.1109/JSTQE.2006.884086.
- [34] S A Maier et al. “Plasmonics—A Route to Nanoscale Optical Devices”. In: *Advanced Materials* 13.19 (2001), pages 1501–1505. DOI: 10.1002/1521-4095(200110)13:19<1501::AID-ADMA1501>3.0.CO;2-Z.
- [35] J B Pendry. “Negative refraction makes a perfect lens”. In: *Physical Review Letters* 85.18 (2000), pages 3966–3969. DOI: 10.1103/PhysRevLett.85.3966.
- [36] Nicholas Fang et al. “Sub- $\lambda/2$  Diffraction-Limited Optical Imaging with a Silver Superlens”. In: *Science* 308.5721 (2005), pages 534–537. DOI: 10.1126/science.1108759.
- [37] Vladimir M Shalaev. “Transforming Light”. In: *Science* 322.5900 (2008), pages 384–386. DOI: 10.1126/science.1166079.
- [38] Suljo Linic, Phillip Christopher, and David B. Ingram. “Plasmonic-metal nanostructures for efficient conversion of solar to chemical energy”. In: *Nature Materials* 10.12 (December 2011), pages 911–921. DOI: 10.1038/nmat3151.
- [39] J M Pitarke et al. “Theory of surface plasmons and surface-plasmon polaritons”. In: *Reports on Progress in Physics* 1.1 (2006), page 54. DOI: 10.1088/0034-4885/70/1/R01. arXiv: 0611257 [cond-mat].
- [40] M. S. Tame et al. “Quantum plasmonics”. In: *Nature Physics* 9.6 (2013), pages 329–340. DOI: 10.1038/nphys2615. arXiv: 1312.6806.
- [41] Dmitri K Gramotnev and Sergey I Bozhevolnyi. “Plasmonics beyond the diffraction limit”. In: *Nat Photon* 4.2 (February 2010), pages 83–91.
- [42] J A Dionne et al. “Planar metal plasmon waveguides: frequency-dependent dispersion, propagation, localization, and loss beyond the free electron model”. In: *Phys. Rev. B* 72.7 (August 2005), page 75405. DOI: 10.1103/PhysRevB.72.075405.
- [43] Pierre Berini. “Long-range surface plasmon polaritons”. In: *Adv. Opt. Photon.* 1.3 (November 2009), pages 484–588. DOI: 10.1364/AOP.1.000484.

- [44] Pierre Berini. “Figures of merit for surface plasmon waveguides”. In: *Optics Express* 14.26 (2006), page 13030. DOI: 10.1364/OE.14.013030.
- [45] Matthew D. Arnold and Martin G. Blaber. “Optical performance and metallic absorption in nanoplasmonic systems.” In: *Optics express* 17.5 (2009), pages 3835–47. DOI: 10.1364/oe.17.003835.
- [46] Omar Kidwai, Sergei V Zhukovsky, and J E Sipe. “Effective-medium approach to planar multilayer hyperbolic metamaterials: Strengths and limitations”. In: *Phys. Rev. A* 85.5 (May 2012), page 53842. DOI: 10.1103/PhysRevA.85.053842.
- [47] R A Flynn et al. “A room-temperature semiconductor spaser operating near 1.5  $\mu\text{m}$ ”. In: *Opt. Express* 19.9 (April 2011), pages 8954–8961. DOI: 10.1364/OE.19.008954.
- [48] Jacob B. Khurgin and Greg Sun. “Practicality of compensating the loss in the plasmonic waveguides using semiconductor gain medium”. In: *Applied Physics Letters* 100.1 (2012). DOI: 10.1063/1.3673849.
- [49] Jacob B. Khurgin and Greg Sun. “Scaling of losses with size and wavelength in nanoplasmonics and metamaterials”. In: *Applied Physics Letters* 99.21 (2011). DOI: 10.1063/1.3664105.
- [50] Paul R. West et al. “Searching for better plasmonic materials”. In: *Laser and Photonics Reviews* 4.6 (2010), pages 795–808. DOI: 10.1002/lpor.200900055. arXiv: 0911.2737.
- [51] M G Blaber, M D Arnold, and M J Ford. “Optical properties of intermetallic compounds from first principles calculations: a search for the ideal plasmonic material.” In: *Journal of Physics: Condensed Matter* 21.14 (2009), page 144211. DOI: 10.1088/0953-8984/21/14/144211.
- [52] Alexandra Boltasseva and Harry A Atwater. “Low-Loss Plasmonic Metamaterials.” en. In: *Science* 331.6015 (January 2011), pages 290–291. DOI: 10.1126/science.1198258.
- [53] Gururaj V. Naik, Jongbum Kim, and Alexandra Boltasseva. “Oxides and nitrides as alternative plasmonic materials in the optical range”. In: *Opt. Mater.* 1.6 (2011), pages 1090–1099. DOI: 10.1103/PhysRevLett.107.133901. arXiv: 1103.6013.
- [54] Gururaj V. Naik, Vladimir M. Shalaev, and Alexandra Boltasseva. “Alternative plasmonic materials: Beyond gold and silver”. In: *Advanced Materials* 25.24 (2013), pages 3264–3294. DOI: 10.1002/adma.201205076.
- [55] Philippe Tassin et al. “A comparison of graphene, superconductors and metals as conductors for metamaterials and plasmonics”. In: *Nature Photonics* 6.4 (2012), pages 259–264. DOI: 10.1038/nphoton.2012.27. arXiv: 1210.0640.
- [56] Giuseppe Grosso and Giuseppe Pastori Parravicini. *Solid State Physics*. Academic Press, 2000.

- [57] Yanwen Wu et al. “Intrinsic optical properties and enhanced plasmonic response of epitaxial silver”. In: *Advanced Materials* 26.35 (2014), pages 6106–6110. DOI: 10.1002/adma.201401474. arXiv: 1306.5360.
- [58] Jacob B. Khurgin and Alexandra Boltasseva. “Reflecting upon the losses in plasmonics and metamaterials”. In: *MRS Bulletin* 37.08 (2012), pages 768–779. DOI: 10.1557/mrs.2012.173.
- [59] Dmitri N Basov and Michael M Fogler. “Quantum materials: The quest for ultrafast plasmonics”. In: *Nat Nano* advance on (December 2016).
- [60] K. S. Novoselov A. N. Grigorenko, M. Polini. “Graphene plasmonics”. In: *Nat. Photonics* 6.October (2012), pages 749–758. DOI: 10.1038/NPHOTON.2012.262. arXiv: 1301.4241.
- [61] F Bonaccorso et al. “Graphene Photonics and Optoelectronics”. In: *Nature Photonics* 4.9 (2010), pages 611–622. DOI: 10.1038/nphoton.2010.186. arXiv: 1006.4854.
- [62] M. G. Blaber, M. D. Arnold, and M. J. Ford. “Designing materials for plasmonic systems: the alkali–noble intermetallics”. In: *Journal of Physics: Condensed Matter* 22.9 (2010), page 95501. DOI: 10.1088/0953-8984/22/9/095501. arXiv: 0908.3707.
- [63] J. B. Khurgin and G. Sun. “In search of the elusive lossless metal”. In: *Applied Physics Letters* 96.2010 (2010), pages 2012–2015. DOI: 10.1063/1.3425890.
- [64] M D Eisaman et al. “Invited Review Article: Single-photon sources and detectors”. In: *Review of Scientific Instruments* 82.7 (2011), page 071101. DOI: <http://dx.doi.org/10.1063/1.3610677>.
- [65] Matthew Pelton. “Modified spontaneous emission in nanophotonic structures”. In: *Nat Photon* 9.7 (July 2015), pages 427–435.
- [66] Leslie E. Ballentine. *Quantum Mechanics - A Modern Development*. 2nd. World Scientific.
- [67] Ari Sihvola. “Metamaterials in electromagnetics”. In: *Metamaterials* 1.1 (March 2007), pages 2–11. DOI: <http://dx.doi.org/10.1016/j.metmat.2007.02.003>.
- [68] Zubin Jacob, Igor I. Smolyaninov, and Evgenii E. Narimanov. “Broadband Purcell effect: Radiative decay engineering with metamaterials”. In: *Applied Physics Letters* 100.18 (2012), page 181105. DOI: 10.1063/1.4710548. arXiv: 0910.3981.
- [69] Dylan Lu et al. “Enhancing spontaneous emission rates of molecules using nanopatterned multilayer hyperbolic metamaterials”. In: *Nat Nano* 9.1 (January 2014), pages 48–53.
- [70] Harish N S Krishnamoorthy et al. “Topological Transitions in Metamaterials”. In: *Science* 336.6078 (April 2012), pages 205–209. DOI: 10.1126/science.1219171. arXiv: 1109.5637.

- [71] Z Jacob, L V Alekseyev, and E Narimanov. “Optical hyperlens: far-field imaging beyond the diffraction limit”. In: *Opt. Express* 14 (2006). DOI: 10.1364/OE.14.008247.
- [72] Z Liu et al. “Far-field optical hyperlens magnifying sub-diffraction-limited objects”. In: *Science* 315 (2007). DOI: 10.1126/science.1137368.
- [73] Sergei V. Zhukovsky et al. “Existence conditions for bulk large-wavevector waves in metal-dielectric and graphene-dielectric multilayer hyperbolic metamaterials”. In: *Proceedings of SPIE* 9125 (May 2014). Edited by Allan D. Boardman et al., page 91251M. DOI: 10.1117/12.2052627.
- [74] Mikhail Y. Shalaginov et al. “Enhancement of single-photon emission from nitrogen-vacancy centers with TiN/(Al,Sc)N hyperbolic metamaterial”. In: *Laser and Photonics Reviews* 9.1 (January 2015), pages 120–127. DOI: 10.1002/lpor.201400185.
- [75] Gururaj V Naik et al. “Epitaxial superlattices with titanium nitride as a plasmonic component for optical hyperbolic metamaterials.” In: *Proceedings of the National Academy of Sciences of the United States of America* 111.21 (2014), pages 7546–51. DOI: 10.1073/pnas.1319446111. arXiv: arXiv:1408.1149.
- [76] Prashant Shekhar, Jonathan Atkinson, and Zubin Jacob. “Hyperbolic metamaterials: fundamentals and applications”. In: *Nano Convergence* 1.1 (December 2014), page 14. DOI: 10.1186/s40580-014-0014-6.
- [77] Wei Yan, Martijn Wubs, and N. Asger Mortensen. “Hyperbolic metamaterials: Nonlocal response regularizes broadband supersingularity”. In: *Physical Review B* 86.20 (November 2012), page 205429. DOI: 10.1103/PhysRevB.86.205429.
- [78] F Bloch. “Bremsvermögen von Atomen mit mehreren Elektronen”. In: *Zeitschrift für Physik* 81.5 (1933), pages 363–376. DOI: 10.1007/BF01344553.
- [79] Alexander L Fetter. “Electrodynamics of a layered electron gas. I. Single layer”. In: *Annals of Physics* 81.2 (1973), pages 367–393. DOI: [http://dx.doi.org/10.1016/0003-4916\(73\)90161-9](http://dx.doi.org/10.1016/0003-4916(73)90161-9).
- [80] B N J Persson and M Persson. “Damping of vibrations in molecules adsorbed on a metal surface”. In: *Surface Science* 97.2 (1980), pages 609–624. DOI: [http://dx.doi.org/10.1016/0039-6028\(80\)90691-3](http://dx.doi.org/10.1016/0039-6028(80)90691-3).
- [81] B N J Persson and N D Lang. “Electron-hole-pair quenching of excited states near a metal”. In: *Phys. Rev. B* 26.10 (November 1982), pages 5409–5415. DOI: 10.1103/PhysRevB.26.5409.
- [82] B N J Persson and S Andersson. “Dynamical processes at surfaces: Excitation of electron-hole pairs”. In: *Phys. Rev. B* 29.8 (April 1984), pages 4382–4394. DOI: 10.1103/PhysRevB.29.4382.
- [83] W L Barnes. “Fluorescence near interfaces: The role of photonic mode density”. In: *Journal of Modern Optics* 45.4 (April 1998), pages 661–699. DOI: 10.1080/09500349808230614.

- [84] Andreas Hirsch. “The era of carbon allotropes”. In: *Nat Mater* 9.11 (November 2010), pages 868–871.
- [85] P. A. M. Diriac. “Series A, Containing Papers of a Mathematical and Physical Character”. In: *Proceedings of the Royal Society of London* 123.792 (1929).
- [86] M Born and R Oppenheimer. “Zur Quantentheorie der Molekeln”. In: *Annalen der Physik* 389 (1927), pages 457–484. DOI: 10.1002/andp.19273892002.
- [87] Jorge Kohanoff. *Electronic Structure Calculations for Solids and Molecules*. Cambridge, 2006.
- [88] W Kohn. “Nobel Lecture: Electronic structure of matter - wave functions and density functionals”. In: *Rev. Mod. Phys.* 71.5 (1999), pages 1253–1266. DOI: 10.1103/RevModPhys.71.1253.
- [89] P Hohenberg and W Kohn. “Inhomogeneous Electron Gas”. In: *Phys. Rev.* 136.3B (November 1964), B864–B871. DOI: 10.1103/PhysRev.136.B864.
- [90] W. Kohn and L. J. Sham. “Self-Consistent Equations Including Exchange and Correlation Effects”. In: *Physical Review* 140.4A (1965), A1133–A1138. DOI: 10.1103/PhysRev.140.A1133.
- [91] Mark S Hybertsen and Steven G Louie. “First-Principles Theory of Quasiparticles: Calculation of Band Gaps in Semiconductors and Insulators”. In: *Phys. Rev. Lett.* 55.13 (September 1985), pages 1418–1421. DOI: 10.1103/PhysRevLett.55.1418.
- [92] M Gajdoš et al. “Linear optical properties in the projector-augmented wave methodology”. In: *Phys. Rev. B* 73.4 (January 2006), page 45112. DOI: 10.1103/PhysRevB.73.045112.
- [93] S Zh. Karazhanov et al. “Electronic structure and optical properties of ZnX ( $X = \text{O}, \text{S}, \text{Se}, \text{Te}$ ): A density functional study”. In: *Phys. Rev. B* 75.15 (April 2007), page 155104. DOI: 10.1103/PhysRevB.75.155104.
- [94] Jess Wellendorff et al. “Density functionals for surface science: Exchange-correlation model development with Bayesian error estimation”. In: *Phys. Rev. B* 85.23 (June 2012), page 235149. DOI: 10.1103/PhysRevB.85.235149.
- [95] Jiří Klimeš, David R Bowler, and Angelos Michaelides. “Chemical accuracy for the van der Waals density functional”. In: *Journal of Physics: Condensed Matter* 22.2 (2010), page 22201.
- [96] Henrik Bruus and Karsten Flensberg. *Many-Body Quantum Theory in Condensed Matter Physics*. Oxford University Press, 2004.
- [97] Stephen L. Adler. “Quantum Theory of the Dielectric Constant in Real Solids”. In: *Physical Review* 126.2 (April 1962), pages 413–420. DOI: 10.1103/PhysRev.126.413.
- [98] Nathan Wiser. “Dielectric constant with local field effects included”. In: *Physical Review* 129.1 (1963), pages 62–69. DOI: 10.1103/PhysRev.129.62.

- [99] Jun Yan et al. “Linear density response function in the projector augmented wave method: Applications to solids, surfaces, and interfaces”. In: *Physical Review B* 83.24 (June 2011), page 245122. DOI: 10.1103/PhysRevB.83.245122. arXiv: arXiv:1104.1273v1.
- [100] Moritz Esslinger et al. “Tetradymites as Natural Hyperbolic Materials for the Near-Infrared to Visible”. In: *ACS Photonics* 1.12 (2014), pages 1285–1289. DOI: 10.1021/ph500296e.
- [101] Ivan V. Iorsh et al. “Hyperbolic metamaterials based on multilayer graphene structures”. In: *Physical Review B* 87.7 (February 2013), page 075416. DOI: 10.1103/PhysRevB.87.075416.
- [102] S. Lebègue et al. “Two-dimensional materials from data filtering and Ab Initio calculations”. In: *Physical Review X* 3.3 (2013), pages 1–7. DOI: 10.1103/PhysRevX.3.031002.
- [103] Filip A. Rasmussen and Kristian S. Thygesen. “Computational 2D Materials Database: Electronic Structure of Transition-Metal Dichalcogenides and Oxides”. In: *Journal of Physical Chemistry C* 119.23 (2015), pages 13169–13183. DOI: 10.1021/acs.jpcc.5b02950. arXiv: 1506.02841.
- [104] Xin Zhang et al. “Phonon and Raman scattering of two-dimensional transition metal dichalcogenides from monolayer, multilayer to bulk material”. In: *Chem. Soc. Rev.* 44.9 (2015), pages 2757–2785. DOI: 10.1039/C4CS00282B.
- [105] Kristen Kaasbjerg, Kristian S Thygesen, and Karsten W Jacobsen. “Phonon-limited mobility in *n*-type single-layer MoS<sub>2</sub> from first principles”. In: *Phys. Rev. B* 85.11 (March 2012), page 115317. DOI: 10.1103/PhysRevB.85.115317.
- [106] N Wakabayashi et al. “Phonons and charge density waves in 1T-TiSe<sub>2</sub>”. In: *Solid State Communications* 28.11 (1978), pages 923–926. DOI: [http://dx.doi.org/10.1016/0038-1098\(78\)90112-6](http://dx.doi.org/10.1016/0038-1098(78)90112-6).
- [107] Junpeng Lu et al. “Atomic Healing of Defects in Transition Metal Dichalcogenides”. In: *Nano Letters* 15.5 (May 2015), pages 3524–3532. DOI: 10.1021/acs.nanolett.5b00952.
- [108] Petr Lazar, Jana Martinová, and Michal Otyepka. “Structure, dynamical stability, and electronic properties of phases in TaS<sub>2</sub> from a high-level quantum mechanical calculation”. In: *Physical Review B* 92.22 (December 2015), page 224104. DOI: 10.1103/PhysRevB.92.224104.
- [109] A H Castro Neto. “Charge Density Wave, Superconductivity, and Anomalous Metallic Behavior in 2D Transition Metal Dichalcogenides”. In: *Phys. Rev. Lett.* 86.19 (2001), pages 4382–4385. DOI: 10.1103/PhysRevLett.86.4382.
- [110] Robert Warmbier, George S Manyali, and Alexander Quandt. “Surface plasmon polaritons in lossy uniaxial anisotropic materials”. In: *Phys. Rev. B* 85.8 (February 2012), page 85442. DOI: 10.1103/PhysRevB.85.085442.

- [111] Edward Yoxall et al. “Direct observation of ultraslow hyperbolic polariton propagation with negative phase velocity”. In: *Nature Photonics* 9.September (2015), pages 674–679. DOI: 10.1038/nphoton.2015.166.
- [112] Tony Low et al. “Polaritons in layered two-dimensional materials”. In: *Nat Mater* advance on (November 2016).
- [113] J. Enkovaara et al. “Electronic structure calculations with GPAW: a real-space implementation of the projector augmented-wave method.” In: *Journal of physics: Condensed matter* 22.25 (2010), page 253202. DOI: 10.1088/0953-8984/22/25/253202.
- [114] P E Blöchl. “Projector augmented-wave method”. In: *Phys. Rev. B* 50.24 (December 1994), pages 17953–17979. DOI: 10.1103/PhysRevB.50.17953.
- [115] C Rostgaard. “The Projector Augmented-wave Method”. In: *ArXiv e-prints* (2009). arXiv: 0910.1921 [cond-mat.mtrl-sci].
- [116] M Shishkin and G Kresse. “Implementation and performance of the frequency-dependent *GW* method within the PAW framework”. In: *Phys. Rev. B* 74.3 (July 2006), page 35101. DOI: 10.1103/PhysRevB.74.035101.
- [117] M Shishkin and G Kresse. “Self-consistent *GW* calculations for semiconductors and insulators”. In: *Phys. Rev. B* 75.23 (June 2007), page 235102. DOI: 10.1103/PhysRevB.75.235102.
- [118] A H MacDonald, S H Vosko, and P T Coleridge. “Extensions of the tetrahedron method for evaluating spectral properties of solids”. en. In: *Journal of Physics C: Solid State Physics* 12.15 (August 1979), pages 2991–3002. DOI: 10.1088/0022-3719/12/15/008.
- [119] C Bradford Barber, David P Dobkin, and Hannu Huhdanpaa. “The Quickhull Algorithm for Convex Hulls”. In: *ACM Trans. Math. Softw.* 22.4 (December 1996), pages 469–483. DOI: 10.1145/235815.235821.
- [120] Hendrik J Monkhorst and James D Pack. “Special points for Brillouin-zone integrations”. In: *Phys. Rev. B* 13.12 (June 1976), pages 5188–5192. DOI: 10.1103/PhysRevB.13.5188.
- [121] E P Wigner and F Seitz. “On the Constitution of Metallic Sodium BT - Part I: Physical Chemistry. Part II: Solid State Physics”. In: edited by Arthur S Wightman. Berlin, Heidelberg: Springer Berlin Heidelberg, 1997, pages 365–371. DOI: 10.1007/978-3-642-59033-7\_34.

